A Fabry-Pérot Microcavity for Quantum Optics with Atomic Defects in Diamond

Erika Janitz
Department of Physics
Faculty of Science
McGill University

August 2019

A thesis submitted to McGill University in partial fulfillment
of the requirements for the degree of Doctor of Philosophy

To my lovely friends

Abstract

The peculiar laws of quantum physics offer a mechanism for exploring fundamentally new types of information processing that promise unprecedented speed and security. Realizing this technology requires a quantum system that can be controlled with exquisite precision, and which can be duplicated and combined into a scalable quantum network. Quantized magnetic moments in diamond, controlled using light via an atom-like defect called the germanium vacancy center, are an example of such a system. The central goal of the work pursued in this thesis is to develop an efficient optical interface for such defects through coupling to an optical cavity, thereby increasing the strength of their interaction with light.

To that end, we present progress toward developing a tunable cavity platform using a microscopic mirror fabricated on the tip of an optical fiber. The first manuscript provides a detailed characterization and model of the optical modes of this system. The model takes into account different sources of loss, such as scattering, absorption, and clipping losses at the fiber mirror resulting from coupling to higher order modes. The second manuscript provides a demonstration of room-temperature cavity coupling to a single emitter. We observe emission into the cavity mode beyond what is possible by filtering effects, resulting in an increased spectral density of cavity fluorescence. In the final manuscript, we actively stabilize the cavity length to the frequency of a laser, achieving a feedback bandwidth of 44 kHz. The laser frequency could in turn be stabilized to the fixed frequency of an emitter optical transition, thereby reducing the cavity detuning.

Moving forward, this system can be cooled to cryogenic temperature where it should be possible to achieve a strong enhancement of coherent emission into the cavity mode. Such a device would directly impact progress towards building a scalable quantum information processing network and will open new avenues for exploring fundamental physics.

Résumé

Les étonnantes lois de la physique quantique offrent un mécanisme permettant d'explorer des types de traitement de l'information fondamentalement nouveaux, promettant des vitesses et un niveau de sécurité sans précédent. La mise en œuvre de cette technologie requière un système quantique apte à être contrôlé avec une extrême précision et pouvant être dupliqué et combiné afin de former un réseau quantique extensible. Un exemple de système répondant à ces caractéristiques est le moment magnétique quantique associé à certains défauts cristallographiques dans le diamant, tel que le défaut dit « centre Germanium-lacune ». Les transitions optiques de ce type de défauts, similaires à celles d'un atome, permettent la manipulation de son moment magnétique de spin par le biais d'ondes lumineuses. Le but principal du travail effectué lors de cette thèse est le développement d'une interface efficiente entre ces défauts et la lumière. Cette interface se matérialise sous la forme d'une cavité optique accroissant l'interaction entre onde et matière.

Dans cet objectif, nous présentons les progrès visant à développer une plateforme ajustable, basée sur un miroir microscopique fabriqué à l'apex d'une fibre optique. Le premier manuscrit fournit une caractérisation détaillée de cette plateforme et décrit un modèle prenant en compte les pertes optiques du système. Le modèle singularise les différentes sources des pertes comme la diffusion, l'absorption et les pertes l'écrêtage dues au couplage avec des modes d'ordres supérieurs. Le second manuscrit démontre le couplage à température ambiante entre un émetteur isolé et la cavité optique. Nous observons une émission préférentielle dans le mode optique définit par la cavité, au-delà d'un simple effet de filtrage, résultant en une augmentation de la densité spectrale. Dans le dernier manuscrit, nous stabilisons la longueur de la cavité vis-à-vis de la longueur d'onde d'un laser de référence et obtenons une bande passante de rétroaction de 44 kHz. La fréquence du laser de référence pourrait être à son tour asservie à une fréquence fixe

correspondant à la transition optique d'un émetteur, réduisant ainsi le désaccordage de la cavité.

Dans le future, ce système pourrait être refroidi à basses températures, pour lesquelles il devrait être possible de d'obtenir une forte amélioration de l'émission dans le mode de la cavité. Un dispositif de ce type participerait directement au progrès visant à construire un réseau quantique extensible et ouvrirait de nouvelles portes dans l'exploration de la physique fondamentale.

Contributions

The body of this dissertation contains three chapters, each representing an original contribution to the chosen field of research. I am the lead or co-lead author on all of these works, and the sole author of this thesis. The specific contributions of each author are listed below by manuscript.

Fabry-Perot Microcavity for Diamond-Based Photonics

E. Janitz: Fabricated the diamond membrane and cavity mirrors, designed and built the experiment, performed the measurements (excluding the white light spectrum), and analyzed the corresponding data. In addition, E. Janitz performed the three-dimensional numerical simulations and wrote the manuscript in collaboration with L. Childress.

M. Ruf: Acquired and analyzed the white light data. M. Ruf also contributed to calculating the power coupling between the cavity and fiber modes.

M. Dimock: Wrote the acquisition code for the white light data, and assisted with other instrumentation.

A. Bourassa: Contributed to the design and construction of the laser ablation setup.

J. Sankey: Provided key insights and assistance with manuscript revision.

L. Childress: Supervised the project and contributed significantly to the experimental design, interpretation of the results, and manuscript writing. In addition, L. Childress developed the one-dimensional cavity model and performed simulations.

Cavity-Enhanced Photon Emission from a Single Germanium Vacancy Center in a Diamond Membrane

R. Høy Jensen: Constructed the experimental setup and wrote the acquisition software. R. Høy Jensen contributed equally with E. Janitz to experimental design, measurements, interpretation, analysis, and manuscript writing.

E. Janitz: Fabricated the diamond membrane, machined the cavity mirrors with Y. He, developed the cavity-coupling theory, and performed the numerical simulations. E. Janitz contributed equally with R. Høy Jensen to experimental design, measurements, interpretation, analysis, and manuscript writing.

Y. Fontana: Designed the initial experiment, created the cavity mount, and performed simulations to calculate the confocal fiber-coupling efficiency. Y. Fontana provided experimental insights, and assisted with manuscript revision.

Y. He: Worked with E. Janitz to fabricate the fiber mirror used in this experiment.

O. Gobron: Provided extensive experimental assistance.

I. Radko: Assisted with the dipole emission calculations.

C. D. Rodríguez Rosenblueth: Assisted with numerical fitting of the white light transmission data.

L. Childress, A. Huck, and U. Lund Andersen: Assisted with interpretation of experimental results and manuscript revision.

A High Mechanical Bandwidth Fiber-Coupled Fabry-Perot Cavity

E. Janitz: Contributed equally with M. Ruf to experimental design and construction. E. Janitz acquired the published data, performed the analysis, and wrote the manuscript.

M. Ruf: Contributed equally with E. Janitz to experimental design and construction.

Y. Fontana: Performed the mechanical simulations and assisted with interpretation of the results.

J. Sankey and L. Childress: Contributed to experimental design, interpretation of results, and manuscript revision.

Acknowledgements

Within five minutes of meeting Lily, I knew that I had found the right PhD supervisor. I was well aware of her seminal contributions to our field, but was nonetheless dazzled by her eloquence, scientific intuition, breadth of knowledge, and sense of humor. Perhaps more important than our long discussions regarding the minutiae of diamond defects and cavities, she taught me how to think critically and approach challenges. Having such an excellent role model and mentor was perhaps the most valuable part of my graduate studies and I am very grateful for the experience.

I would like to thank the Childress lab, specifically the fiber cavity team comprising Yannik, Mark, Rigel, César, and Sparrow. I am also lucky to have worked alongside Adrian, Zack, Luke and Märta. In addition, I would like to thank Jack for his supervision and advice, as well as the members of the Sankey lab including Max, Vincent, Simon, Christoph and Tina. I am also indebted to Yoichi and Robert for their help with many experimental challenges. Finally, I was lucky enough to partake in a fruitful collaboration with Ulrik Andersen's group at DTU during my last year of studies, and would particularly like to thank Rasmus, Alex, Olivier, Ilya, Yuriy, Mads, and Maxime.

In addition, I would like to acknowledge my friends and family. Rosa and John, you were the best room-mates and I miss our little family. Fiona and Dylan, there are too many hilarious moments to count and I love you both. I am grateful for my highschool girlfriends Mel, Ketrina, and Malaika for prioritizing our friendship regardless of time and distance. Thank you to all of my friends in Montreal, Waterloo, San Francisco, Copenhagen, and Boston for fuelling my joie de vivre!

Lastly, I would like to thank my family, specifically my mother, sister, adopted father Emmanuel, Aunt Teresa, and Uncle Rob. Thank you for loving and supporting me implicitly. Kevin, Janet, Michael, and Claire - I am so lucky to have you in my life.

Finally, thank you Eric for everything. You are my best friend and biggest supporter. None of this would have been possible without you.

Contents

List of Figures

List of Tables

1

Introduction

The field of quantum information exploits the properties of quantum mechanics to improve on classical computing technologies, providing exponential speedup for certain algorithms [1, 2] and simulations [3, 4], as well as unprecedented cryptographic security [5–7]. The physical requirements for such a technology are succinctly described by the DiVincenzo criteria [8], which state that any feasible platform must contain isolated quantum bits (or qubits) that can store information for long timescales, have well-defined initialization and readout mechanisms, provide a set of universal quantum computational gates, and support a way to couple individual qubits into a scalable system. Recently, there has been impressive experimental progress in fulfilling these criteria, with Google releasing an on-chip quantum processor of 72 qubits in 2018 [9]. While short-range interactions are sufficient for coupling qubits on chip-scale devices, longer-range interactions are necessary for delocalized applications such as quantum communication [10] and distributed quantum computing [11]. Such technologies require the realization of a quantum network, where information is processed and stored locally in quantum nodes that are connected via long-range quantum channels [12, 13]. Hybrid light-matter systems represent the leading candidates for realization of such networks, where photons (referred to as flying qubits) interface coherently and reversibly with quantum states of matter. There are currently several promising candidates for use as stationary nodes in such systems including trapped atoms and ions, quantum dots, rare-earth-ion-doped crystals, and atomic defect centers in diamond. We will now consider the strengths and weaknesses of each of these technologies in turn.

Neutral atoms and ions exhibit internal-state dependent optical transitions, providing a natural interface between quantum states of matter and light [14]. Furthermore, it is possible to obtain strong, coherent interaction between these states and a well-defined photonic mode through coupling to an optical cavity [15]. While extensive work has been done in storing quantum states in large atomic ensembles [16, 17], single- to few-particle systems are particularly promising as they can naturally constitute a few-qubit processor. For example, recent demonstrations have utilized different ionic species in

the same trap as optical interfaces and long-lived quantum memories [18]. Advantages of such platforms include long spin coherence times (over 10 minutes has been demonstrated) [19], and fixed optical transition frequencies for a given atomic species owing to their identical nature. Limiting their use is the challenge of cooling and trapping small particle numbers inside cavities with small mode volumes [20]. This is further exacerbated in ionic systems where trapping potentials are perturbed by dielectric interfaces (such as mirrors), limiting their proximity [21]. Despite these challenges, prototypical quantum networks have been demonstrated using single atoms in optical cavities [22].

Semiconductor quantum dots represent another promising platform for creating a coherent light-matter interface. These nanofabricated devices behave as artificial atoms, exhibiting discrete energy levels due to geometric confinement and electrostatic interactions [23]. Quantum dots have intrinsically large optical dipole moments since they contain on the order of $10^4 - 10^5$ atoms [23], leading to stronger optical interactions compared to atomic systems. Furthermore, these devices are fixed within a semiconductor matrix, allowing optical or electrical components to be structured using mature semiconductor fabrication techniques. On the other hand, the solid-state nature of these devices also poses some experimental challenges as the nuclear spin bath of the substrate causes rapid dephasing [24], while variation in quantum dot size leads to large inhomogenous broadening [23]. Nevertheless, optically-mediated entanglement has been demonstrated between quantum dots separated by 5 m [25].

Crystals doped with rare-earth ions constitute a third candidate technology, and have been used to couple quantum states of light to collective atomic excitations [26]. These demonstrations are largely analogous to work done with atomic vapors, without the added effort of cooling and trapping. Such systems can exhibit long coherence times [27], and offer the additional benefit of multimode operation due to the large inhomogenous absorption spectrum caused by crystal defects and strain [28]. However, it has been challenging to realize a local few-qubit quantum processor due to the inherently delocalized nature of the ensemble [29], with some progress in realizing two-qubit quantum gates between subensembles in the same crystal [30]. So far, there has been an impressive demonstration of optically-mediated entanglement between collective excitations in two different crystals [31], and promising recent work on isolating single rare-earth ion defects for use as individual quantum systems [32–34].

A final architecture for realizing a coherent spin-photon interface utilizes individual spins in diamond as matter qubits, which are photonically-coupled via optically-active crystallographic defects. Like quantum dots, these systems are localized in the diamond substrate, behaving like isolated atoms in a solid-state system. Similar to atomic or rare-earth-ion systems, they can exhibit long coherence times due to the largely spin-free environment of diamond [35, 36]. Defects offer a further advantage by providing access to several proximal nuclear spins, allowing the realization of a few-qubit quantum processor [37]. These comparatively attractive properties make defects in diamond a promising candidate for use as a node in quantum networks, and are the platform explored in this thesis.

Crystallographic defects of interest include the well-studied nitrogen vacancy (NV) center, the relatively novel negatively charged silicon vacancy (SiV) and germanium vacancy (GeV) centers, the neutral SiV center [38], and other newly discovered defects containing group IV elements [39–41]. Thus far, nitrogen vacancy centers have been used to demonstrate many critical elements of a quantum network, owing to their long-lived electronic spin states [42] that can be tuned and controlled through the application of magnetic and microwave fields [43]. The electronic spin can be coupled to even longer-lived nuclear spins in diamond via the hyperfine interaction [44, 45], which can serve as quantum memories. Furthermore, one- and two-qubit quantum gates between spin states have been demonstrated with 99.995% and 99.2% fidelities respectively [46]. At cryogenic temperatures, the zero phonon line (ZPL) emission can exhibit coherent, spin-dependent optical transitions [47–49], which have been used to entangle the electronic spin with the state of an emitted photon [50]. Indistinguishable fluorescence from separate defects has been verified by two-photon quantum interference [51, 52], a tool which was later used in creating projective entanglement between the electronic spins of NV centers separated by up to 1.3 km [53, 54]. Similar entanglement protocols have been used to demonstrate teleportation of a quantum state [55], as well as entanglement distillation [56]. So far, entanglement rates with NV centers have been limited to tens of hertz [57] due to spectral diffusion from the permanent dipole moment [58], the low branching ratio into the ZPL (3%) [43], the long excited state lifetime (12 ns) [59], and the difficulty of collecting emitted photons into a well-defined optical mode.

One approach to improving entanglement rates is to work with a different emitter with superior optical properties. Defects containing group IV elements such as SiV and

GeV centers exhibit higher symmetry than the NV center, leading to a vanishing permanent electric dipole moment [39]. This has been shown to strongly suppresses spectral diffusion for both as-grown [60–62] and implanted emitters [63]. In addition, these defects exhibit a higher fraction of emission (larger branching ratio) into the ZPL as they have similar charge densities in the ground and excited states [64]. For example, the negatively charged GeV center has a ZPL branching ratio of 60% [62, 65], the negatively charged SiV center has a branching ratio of 70% [66], and the neutral SiV has a branching ratio of 90% [38].

Another method for increasing interaction rates is to couple defects to optical cavities, which can enhance emission into their spectral and spatial modes via the Purcell effect [67], thereby increasing both emission at the ZPL frequency and collection efficiency, as compared to the 4π solid angle of free-space emission. Figures of merit for such a defect-cavity system include a high optical quality factor, small mode volume, and excellent emitter optical properties. One approach is to fabricate the resonator from the diamond itself, where demonstrated structures include whispering gallery mode [68] and racetrack resonators [69], as well as one- [70, 71] and two-dimensional [72] photonic crystal cavities. These devices are attractive for their small mode volumes (which can be less than one cubic wavelength in diamond) and high quality factors ($Q > 10^5$ has been shown for photonic crystal beams [73]). Unfortunately, defects in these devices are necessarily close to nanofabricated interfaces, which results in spectral diffusion of many GHz for NV centers [72, 74]. In contrast, SiV and GeV centers in similar structures have exhibited comparatively minimal spectral diffusion due to their insensitivity to interfaces [75–77], providing an alternative path forward. Some remaining challenges in coupling defects to nanophotonic devices include spatial alignment of the emitter to the cavity mode, where progress has been made in implanting impurities with high spatial accuracy using focused ion beam milling [78]. Furthermore, finite fabrication tolerances can result in spectral detuning of the cavity resonance from the emitter optical transition, which can be mitigated by further etching of the device or by gas condensation at cryogenic temperatures [70, 79].

A complementary approach is to instead couple defects to microscopic Fabry-Perot cavities, which can have much higher quality factors (limited only by the mirror finesse which can approach one million [80]), at the expense of larger mode volumes (minimum of a few cubic wavelengths [81]). Such a cavity platform is extremely flexible compared

to nanofabricated structures, since the spherical mirror can be moved laterally to position the cavity waist on the emitter of interest, while the cavity frequency can be tuned via the mirror spacing. Consequently, these types of resonators have already been coupled to a myriad of different systems, including quantum dots [82], atoms [83], ions [84, 85], molecules [86], mechanical elements [87], and nanostructures [88]. Room temperature cavity coupling has also been demonstrated for NV [89] and SiV centers [90] in nanodiamonds; however, these crystals exhibit inhomogeneous broadening of hundreds of GHz [91], rendering them unsuitable for use in quantum networks. Recently, open cavities were coupled to implanted NV centers in micron-thick diamond membranes that exhibited spectral diffusion of $\approx$1 GHz at cryogenic temperatures (a factor of 60 larger than the lifetime-limited linewidth) [92]. Moving forward, it should be possible to achieve optical linewidths approaching the radiative limit by choosing a defect without a permanent dipole moment or by using native nitrogen to form NV centers [93, 94]. In addition, the comparatively narrow resonances of open cavity systems ($\sim$ 100 MHz - 1 GHz) can enhance individual spin-selective transitions within the ZPL, which has direct applications in some quantum network proposals [95, 96]. Finally, it is relatively easy to achieve high collection efficiency in cavity transmission; for example, spherical mirrors fabricated on the tip of an optical fiber have achieved over 85% power coupling into the guided mode [81].

In this thesis, we propose to combine the excellent optical properties of a single GeV center in a diamond membrane with the flexibility of a microscopic Fabry-Pérot fiber cavity geometry. This platform will serve as a step toward an efficient and coherent spin-photon interface using defects in diamond. The remainder of this chapter will present the basic theory uderlying the GeV center and Purcell enhancement, as well as the fabrication procedures for creating the cavity mirrors and diamond membranes.

1.1 The Germanium Vacancy Center in Diamond

The germanium vacancy center is an optically-active defect in diamond occurring along the $\langle 111 \rangle$ family of crystalline axes. These emitters comprise two missing carbon atoms (vacancies) and an interstitial germanium atom [97, 98] (see Fig. 1a), resulting in a defect with D_{3d} symmetry (similar to the SiV center) with a vanishing permanent electric

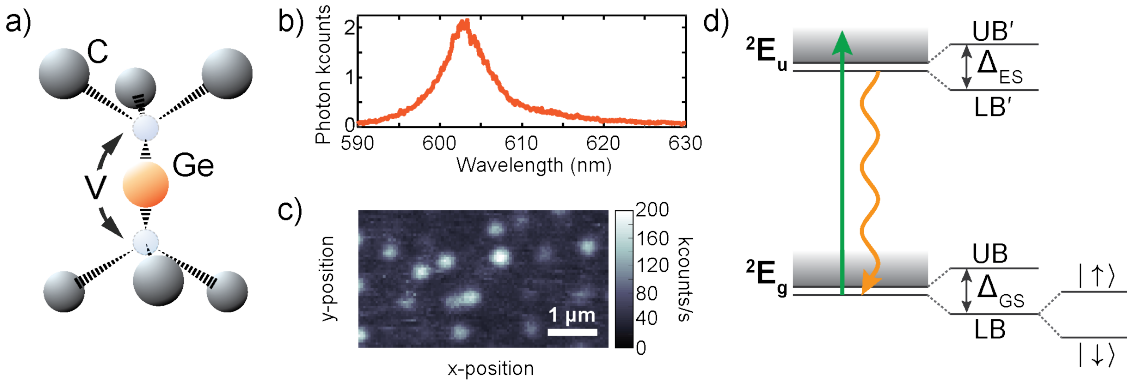

Figure 1: a) The crystallographic structure of the GeV center, where C refers to carbon atoms, V to vacancies, and Ge to the germanium atom. b) A room temperature spectrum of the GeV center emission. c) A confocal image of an implanted sample where bright spots correspond to single GeV centers. d) The electronic structure of the GeV center. The defect can be excited off-resonantly into the phonon sideband (green arrow) and will emit with a ZPL wavelength of 602 nm (orange arrow). The ground and excited states are doubly degenerate in both spin and orbital states with the upper and lower orbital branches labelled. The spin degeneracy in an orbital branch can be lifted through application of a magnetic field (shown for the ground state LB).

dipole. The optical transitions of GeV centers are within the bandgap of diamond [39, 99], causing them to behave as isolated atoms in a solid state system. Emitters can be created through the introduction of impurities during diamond growth [62, 65, 99, 100], or through subsequent ion implantation and annealing [77, 99], with densities such that single defects are optically addressable via confocal microscopy (see Fig. 1b). GeV centers can be excited resonantly at the ZPL wavelength (602 nm) [62, 77], or into the phonon sideband (PSB) with higher energy photons [101]. The ZPL emission is broad at room temperature (linewidth $\sim$ 5 nm), with a reported branching ratio of 60% (Huang-Rhys factor of 0.5 [65], see Fig. 1c). The remaining 40% of emission is accompanied by a high frequency phonon and occurs at longer wavelengths. There is some discrepancy in the literature regarding the location of the PSB features, with reports of peaks at 615 nm [102], 616 nm [65], 640 nm [103], and 641 nm [65], in addition to claims that the PSB extends over 200 nm [101]. It is challenging to identify these features in part because the second order Raman emission in diamond from a 532 nm laser appears between

600 − 620 nm [99, 104]. There may also be differences in the PSB structure between nanocrystal and bulk samples.

The orientation of the optical dipole(s) has not been carefully studied for this defect, but they are expected to be along the ⟨111⟩-axis or in the perpendicular plane based on crystallographic symmetry. The SiV center was found to have its strongest optical dipole along the defect axis [61], with evidence of weaker transitions in the perpendicular plane, but this may not be the case for the GeV center. In addition, differing values for the quantum efficiency have been reported in literature. The efficiency was inferred to be high through measurements of the excited state lifetime, which showed little change as a function of temperature (or the phononic density of states) [77]. Further comparison of experimental parameters in the cited work led to a lower bound of 40%. Other groups have cited comparatively low efficiencies (in the realm of 3%) based on absorption measurements with nano and microcrystals [103].

The GeV center electronic structure (Fig. 1d) is very similar to that of the SiV center [105], where optical transitions occur between ^2E_u and ^2E_g energy levels. In low strain samples, the GeV center ground and excited states are both orbital and spin degenerate ($S = 1/2$), where the orbital degeneracies are partially lifted by a combination of dynamic Jahn-Teller effect and spin-orbit interaction [39] with energy splittings Δ_{GS} and Δ_{ES}. At cryogenic temperatures, the individual ZPL transition linewidths can approach the lifetime-limit of 26 MHz for the reported 6 ns excited state lifetime [62]. This allows for spectroscopic observation of the four-line fine structure corresponding to transitions between the different ground and excited orbital states [62]. An effective two-level system can be defined within the lower orbital branch (LB) of the ground state by further applying a magnetic field to split the spin sublevels via the Zeeman interaction [106]. So far, optical preparation of different ground state spin superpositions has been demonstrated, as well as spin manipulation through the application of resonant microwave fields [62]. These experiments yielded relaxation times of up to $T_1 = 25 \pm 5$ μs and $T_2 = 19 \pm 1$ ns, limited by transitions between orbital branches caused by absorption or emission of single phonon at the orbital splitting frequency [77, 107]. The coherence can therefore be improved by either reducing the phononic density of states or occupation at energy Δ_{GS}. A simple method for reducing the thermal phonon occupation is to cool the sample to a temperature well below the ground state splitting ($\approx$ 150 GHz [77], corresponding to 7.2 K). This approach was recently employed for SiV cen-

ters ($\Delta_{GS} \approx 50$ GHz, corresponding to 2.4 K) in a dilution refrigerator, where $T_2 = 13$ ms was achieved for a sample at 100 mK, with a polarization in LB of over 99% [106].

Despite relatively poor coherence times at liquid helium temperatures, there has been an impressive experiment showing optical nonlinearity caused by a single GeV center coupled to a nanofabricated waveguide. In this work, resonant coupling between a ZPL transition and the waveguide mode reduced the transmission by $18 \pm 1\%$ in a single optical pass [77]. In contrast to previous work with NV centers, implanted defects in these devices exhibited nearly lifetime-limited optical transitions (within a factor of ≈ 3). This demonstration is very encouraging for future cavity measurements, which could easily achieve higher quality factors and smaller mode volumes.

1.2 Purcell Enhancement

The Purcell effect describes the change in spontaneous emission rate for an atomic system coupled to an optical structure, thereby modifying the photonic density of states [67]. Optical cavities are examples of such structures, where the enhanced emission rate into the cavity mode is quantified by the so-called Purcell factor:

$$F_p = \frac{\gamma_{cav}}{\gamma_{free}}, \tag{1.1}$$

where γ_{cav} and γ_{free} are the cavity-coupled and freespace emission rates. Here, we follow Ref. [108] to derive F_p for a two-level emitter initially prepared in the excited state with zero photons in the system ($|e,0\rangle$). This is an eigenstate of the atomic Hamiltonian:

$$\hat{H}_{atom} = \hbar\omega |e,0\rangle\langle e,0|, \tag{1.2}$$

where ω is the frequency of the atomic transition. Based on this Hamiltonian, the emitter should never decay to the atomic ground state through emission of a photon ($|g,1\rangle$). Interestingly, spontaneous emission is made possible through the presence of zero-field fluctuations in the photonic ground state which couple to the system via the interaction Hamiltonian:

$$\hat{\mathbf{H}}_{\mathbf{int}} = -\hat{\mathbf{E}}(\mathbf{r}) \cdot \hat{\mathbf{d}}. \tag{1.3}$$

Here, $\hat{\mathbf{E}}(\mathbf{r})$ represents the quantized electric field operator and $\hat{\mathbf{d}}$ is the electronic dipole operator. The electric field operator is given by:

$$\hat{\mathbf{E}}(\mathbf{r}) = \left(\mathbf{E}(\mathbf{r})\,\hat{a} + \mathbf{E}^*(\mathbf{r})\,\hat{a}^\dagger\right), \tag{1.4}$$

where $\mathbf{E}(\mathbf{r}) = i\,E_0\,\mathbf{f}(\mathbf{r})$ is the electric field at position $\mathbf{r}$ with $E_0 = \sqrt{\frac{\hbar\omega}{2\epsilon_0 V}}$ and normalized vector $\mathbf{f}(\mathbf{r})$. The photonic creation and annihilation operators are denoted $\hat{a}^\dagger$ and $\hat{a}$ respectively and V is the electromagnetic quantization volume. The electric dipole operator can be written as:

$$\hat{\mathbf{d}} = \boldsymbol{\mu}\,\hat{\sigma}^+ + \boldsymbol{\mu}^*\,\hat{\sigma}^-, \tag{1.5}$$

where $\boldsymbol{\mu}$ is the dipole moment and $\hat{\sigma}^+$ and $\hat{\sigma}^-$ are the atomic raising and lowering operators respectively. The resulting spontaneous emission rates can be calculated using Fermi's golden rule (for a full derivation see Ref. [109]):

$$\gamma_{e,g} = \frac{2\pi}{\hbar^2} D(\omega)\left|M_{e,g}\right|^2, \tag{1.6}$$

where $D(\omega)$ is the photonic density of states and $M_{e,g} = \langle g, 1|H_{int}|e, 0\rangle$ is the transition matrix element. With these definitions we can rewrite Eq. 1.6:

$$\gamma_{e,g} = \frac{\pi\omega}{\hbar\,\epsilon_0 V} D(\omega)\left|\mathbf{f}(\mathbf{r_0})\cdot\boldsymbol{\mu}\right|^2, \tag{1.7}$$

where $\mathbf{r_0}$ is the position of the two-level system. This result is a general form for the spontaneous emission rate, which is a function of the photonic density of states as well as the overlap between the emitter dipole and vacuum electric field.

We can now calculate the spontaneous emission rates γ_{cav} and γ_{free} used in Eq. 1.1. For an emitter in a bulk medium of refractive index n, the freespace density of states is:

$$D(\omega) = \frac{n^3\omega^2 V}{\pi^2 c^3}. \tag{1.8}$$

Averaging over all possible orientations of the electric field gives $\left|\mathbf{f}(\mathbf{r_0}) \cdot \boldsymbol{\mu}\right|^2 = \frac{|\boldsymbol{\mu}|^2}{3}$, resulting in a freespace emission rate of:

$$\gamma_{free} = \frac{|\boldsymbol{\mu}|^2}{3\pi\hbar\epsilon_0}\left(\frac{\omega n}{c}\right)^3. \tag{1.9}$$

In contrast, the density of states for an optical cavity is parameterized by a Lorentzian:

$$D(\omega) = \frac{2}{\pi}\frac{\kappa^2}{\kappa^2 + 4\Delta^2}, \tag{1.10}$$

where κ is the cavity decay rate and $\Delta = \omega - \omega_c$ is the emitter-cavity detuning. For resonant coupling ($\Delta = 0$), this reduces to $D(\omega_c) = \frac{2}{\pi\kappa}$, resulting in a spontaneous emission rate of:

$$\gamma_{cav} = \frac{2\omega}{\hbar\,\epsilon_0\,\kappa\,V}\left|\mathbf{f}(\mathbf{r_0}) \cdot \boldsymbol{\mu}\right|^2. \tag{1.11}$$

Unlike the freespace electric field, the cavity field has a well-defined polarization, resulting in alignment-dependent values of $\left|\mathbf{f}(\mathbf{r_0}) \cdot \boldsymbol{\mu}\right|^2$. The cavity mode volume is given by [23]:

$$V = \frac{\iiint n^2(\mathbf{r})|\mathbf{E}(\mathbf{r})|^2 d^3\mathbf{r}}{n^2(\mathbf{r_0})|\mathbf{E}(\mathbf{r_0})|^2}. \tag{1.12}$$

Substituting these results into Eq. 1.1 yields the enhancement in spontaneous emission rate for an atomic system resonantly coupled to a cavity:

$$F_p = \frac{\gamma_{cav}}{\gamma_{free}} = \frac{3}{4\pi^2}\left(\frac{\lambda}{n}\right)^3\left(\frac{Q}{V}\right)\frac{\left|\mathbf{f}(\mathbf{r_0}) \cdot \boldsymbol{\mu}\right|^2}{|\boldsymbol{\mu}|^2}. \tag{1.13}$$

where $Q = \frac{\omega_c}{\kappa}$ is the cavity quality factor, and V is the mode volume of the cavity. For open cavity geometries that do not modify the rate of emission into freespace modes, the overall increase in the spontaneous emission rate can be calculated as:

$$\frac{\gamma_{free} + \gamma_{cav}}{\gamma_{free}} = 1 + F_p. \tag{1.14}$$

This can be generalized for a cavity resonantly coupled to a transition with branching ratio ζ and quantum effciency η_{QE}:

$$\frac{\gamma_{free} + \gamma'_{cav}}{\gamma_{free}} = (1 + \zeta\, \eta_{QE}\, F_p), \tag{1.15}$$

where $\gamma'_{cav} = \zeta\, \eta_{QE}\, \gamma_{cav}$ is the modified emission into the cavity mode. The Purcell factor and increase in spontaneous emission rate will serve as figures of merit for the work discussed in this thesis.

1.3 Cavity Mirror Fabrication

Open microcavities formed by spherical mirrors on the tips of optical fibers offer a flexible platform for enhancing light-matter interactions with atomic defects in diamond. Thus far, such cavities have been coupled to defects in nanodiamonds at room temperature [89, 90, 110], while another type of open microcavity (where the spherical mirror is instead fabricated on a silica substrate) has been coupled to NV centers in both nanodiamonds [111] and diamond membranes at cryogenic temperatures [92]. In this work, we aim to combine the advantageous elements of these experiments, coupling a high-finesse fiber cavity to a single GeV center in a diamond membrane at cryogenic temperatures.

We employ a half-symmetric cavity setup, where the diamond membrane sample is bonded to a macroscopic flat mirror (see Fig. 2). The cavity is then formed by the fiber mirror, which can be shifted laterally to position the cavity mode on an emitter and longitudinally to tune the cavity frequency. Our goal is to maximize the Purcell enhancement of the GeV center ZPL emission, which is proportional to cavity quality factor divided by the mode volume (see Eq. 1.13). The quality factor is limited by the surface roughness of the micromirror substrate and losses in the applied mirror coatings (consisting of scattering, absorption, and transmission), whereas the cavity mode volume is determined by the diameter of the cavity waist (ω_0) and the energy distribution along the cavity axis (according to Eq. 1.12). The mode volume is therefore optimized by reducing the cavity waist diameter and effective cavity length, which can be achieved experimentally by minimizing the fiber mirror radius of curvature (R), ablation depth, diamond thickness

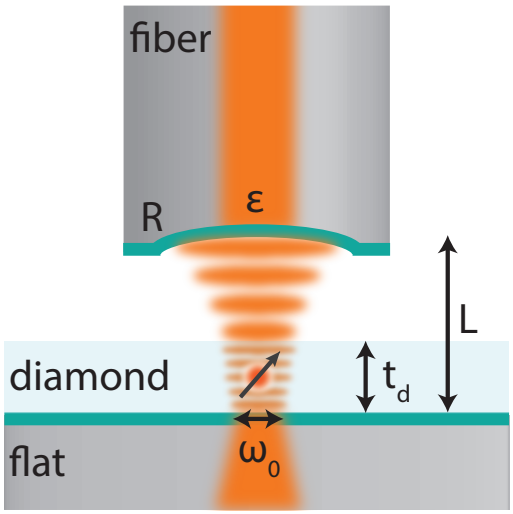

Figure 2: A schematic of a fiber cavity coupled to a single GeV center in a diamond membrane. The geometric cavity length (L), diamond thickness (t_d), waist diameter (ω_0), mirror radius of curvature (R), and coupling efficiency (ϵ) between the fiber and cavity modes are indicated. The dielectric mirror coatings are illustrated in green.

(t_d), and the geometric spacing between mirrors (L). In addition, electric field penetration into the mirror coatings also contributes to this effective length, but is fixed as a function of wavelength. A final tangential goal is to maintain a high electric field overlap (ϵ) between the cavity mode and the propagating mode of the fiber. This is achieved through precise centering of the mirror relative to the fiber core and matching the wavefronts of the cavity mode to those of the single mode fiber (optimized for cavity lengths that are much shorter than the Rayleigh range).

There has been extensive experimental progress in realizing optimized microcavity parameters in recent years. The key component of this platform is the microscopic spherical mirror, which is typically created through infrared laser ablation [81] or focused ion beam (FIB) milling [112]. Laser machining is accomplished using a CO_2 infrared laser, leading to both evaporation and reflowing of the glass at the fiber tip. This process results in an ultrasmooth Gaussian dimple with a reported surface roughness of only 0.2 nm-rms [113], corresponding to scattering losses of $\left(\frac{4\pi\sigma}{\lambda}\right)^2 \approx 17$ ppm at $\lambda = 602$ nm (the GeV center ZPL wavelength) [114]. Recent advances in fabrication have achieved radii of curvature below 5 μm with ablation depths of only ≈ 1 μm [115], corresponding to potential mode volumes of only a few cubic wavelengths. FIB milling offers a com-

plementary approach for fabricating the micromirror geometry, which can in principle achieve smaller radii of curvature as it is not limited by the diffraction limit of infrared light. Thus far, radii down to 5 μm [112] with depths of ≈ 1 μm [110] have been reported, at the expense of higher surface roughness (0.3 − 0.7 nm-rms [110, 112]). Once the spherical dimple is machined, both mirror substrates are coated with high-finesse dielectric mirrors, which can achieve losses on the part-per-million level, resulting in finesse approaching one million [80].

The mode volume can be further reduced by thinning the diamond membrane, though a certain minimum distance must be maintained between defects and interfaces in order to avoid spectral diffusion [72]. However, promising recent results have shown that it is possible to have coherent optical transitions for NV centers created via electon irradiation in few-micron-thick membranes [94]. Finally, excellent power coupling between the cavity and fiber modes of over 85% has been demonstrated through accurate centering of the ablation on the fiber core and using a relatively large radius of curvature (450 μm) for wavefront matching [81].

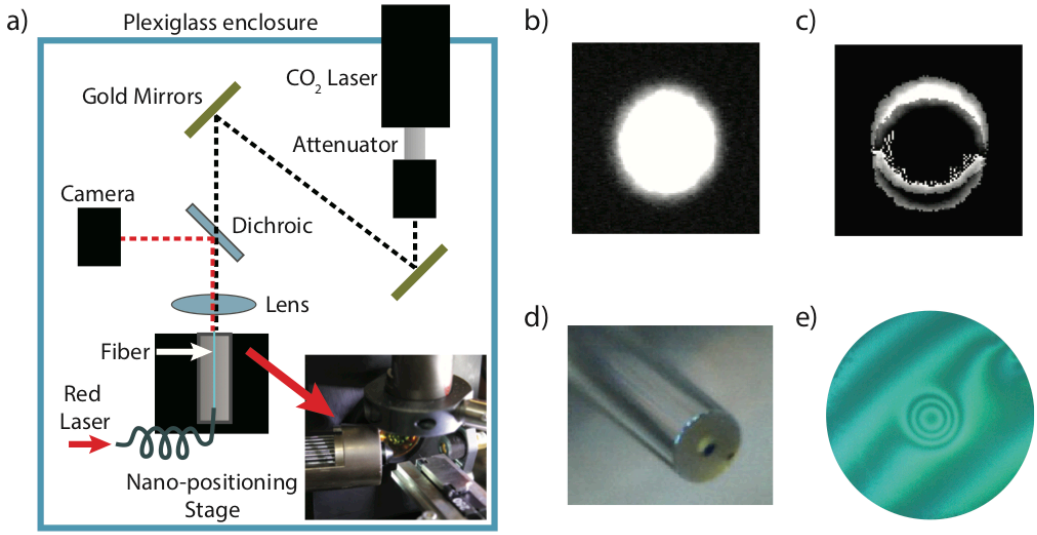

Figure 3: a) A schematic of the laser ablation setup. b) An image of the alignment laser exiting the fiber core. c) An example of the image subtraction used for aligning subsequent fibers. d) An ablated fiber tip showing the Gaussian indentation. e) An interferometric image of an ablated fiber tip.

For our experiment, we developed a laser ablation procedure capable of making mirrors with radii of curvature down to 15 μm and a dimple surface roughness below 0.2 nm-rms (this measurement was limited by the resolution of our atomic force microscope). In addition, we achieve excellent fiber coupling by aligning the ablation to the center of the fiber with sub-micron repeatability through a novel alignment procedure. We machine our fibers using millisecond pulses of light from a 40 W CO_2 laser emitting at 10.6 μm (setup in Fig. 3a), guided using two gold mirrors through a dichroic beamsplitter and focused down by a lens onto the tip of a fiber. Rough alignment is performed using two microscope cameras (inset Fig. 3a), and fine alignment is achieved by shooting a visible laser through the back of the fiber, where it is reflected by the dichroic mirror and imaged onto a camera (Fig. 3b). Once centering has been achieved for one fiber and an image is captured, subsequent fibers can be aligned using image subtraction software with 0.5 μm-rms repeatability (Fig. 3c). The ablation leaves a Gaussian imprint on the fiber tip (Fig. 3d) which can be approximated as parabola near the center. The geometric parameters of the ablation are assessed by fitting images of the fiber tip obtained using a custom-built interferometer (Fig. 3e). Tests of our coated mirrors have resulted in scattering and absorption losses below 10 ppm, and power coupling between the cavity and fiber modes of $\approx 50\%$ for a fiber with $R \approx 60$ μm [116].

1.4 Diamond Membrane Fabrication

We incorporate defects into the cavity via high-quality diamond membranes, which must be thin enough to achieve short cavity lengths (∼1-10 μm), have surface roughness on the 0.1 nm-rms level to preserve the optical quality factor, and contain individually addressable GeV centers (density of ≈ 1 GeV center per mode volume).

Our diamond membranes are fabricated from $\langle 100 \rangle$-cut electronic grade bulk diamond plates (Element 6) that are 0.5 mm thick. Due to the slow etch rate of diamond, preliminary membranes are made by commercial laser slicing of these plates into 2-3 membranes that are 20 ± 10 μm thick (Delaware Diamond Knives). The resulting membranes are specified (on a best effort basis) to have an arithmetic average roughness of Ra$<$ 5 nm, and a parallelism of 3 μm across the sample (corresponding to a membrane wedge of $<$ 1 μm/mm). We then process the samples in a 2:1 piranha solution

and transfer them to a clean sapphire carrier wafer either with tweezers or suspended on a water droplet if the sample is $\leq$ 5 μm thick. At this point, the membrane can be dried using a nitrogen gun, which will dry the top surface and cause water to wick out from under the sample. Sufficiently thin ($\lesssim$ 30 μm) samples will bond to the carrier via Van der Waals forces, while thicker samples are instead rested (unbonded) on the carrier wafer during etching. Thinning and smoothing of the membrane is accomplished

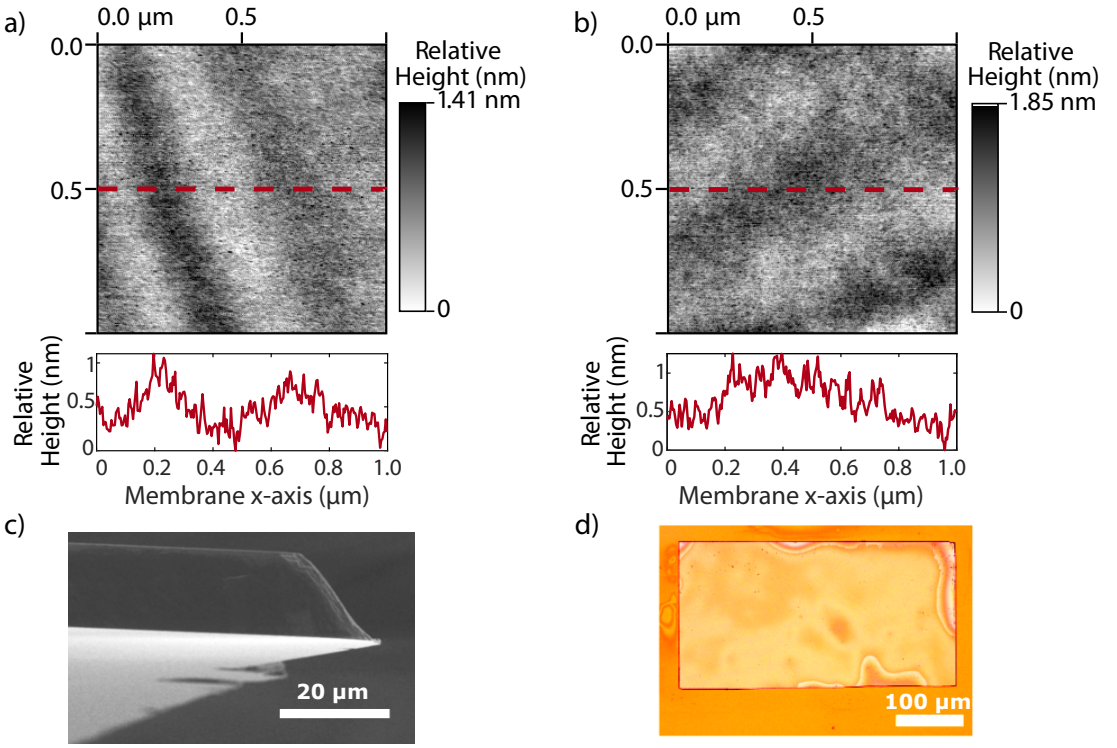

Figure 4: a) AFM image of an optical grade membrane etched with $ArCl_2$, below is a line cut along the y=0.5 μm to show the height variation. b) The same characterization after the sample was etched with O_2/Ar. c) An SEM image of a diamond membrane used to measure the membrane thickness. d) A microscope camera image showing a membrane bonded to a mirror substrate. The fringes in the center of the membrane are caused by interference of light inside the sample. The fringes around the edge of the sample are due to interference of light between the bottom surface of the membrane and the mirror, caused by imperfect bonding.

through an inductively-coupled plasma reaction ion etching (ICP RIE) process, which cycles between 1 hour of $ArCl_2$ and 15 minutes of Ar/O_2 (parameters in Tab. 1) [117, 118]. The $ArCl_2$ etching process is slow and comparatively isotropic, making it ideal for

Etch Parameter	$ArCl_2$	O_2/Ar
Formula	40 sccm Cl_2+10 sccm Ar	30 sccm O_2+5 sccm Ar
Platen Power (W)	250	300
Coil Power (W)	600	600
Chamber Pressure (mTorr)	10	10

Table 1: Parameters for the cycled etching process.

smoothing the membrane surface and removing polishing damage from the slicing process. The subsequent Ar/O_2 etch is faster, but more sensitive to surface contamination and subsequent masking, and will consequently only transfer a low surface roughness for a short period of time. There is some evidence that Cl_2 ions can tunnel into diamond during an $ArCl_2$ ion etching process [119], which has been rumoured to cause the destabilization of near-surface defect centers. We therefore opt to end our process with an Ar/O_2 etch plasma.

Our etch recipes were tested on an optical grade membrane, which has higher impurity concentrations than electronic grade samples but should exhibit the same etching behavior. After each step, the rms surface roughness was assessed over a $\sim 600 \times 600$ nm region, resulting in $\sigma = 0.25$ nm-rms for 1 hour of $ArCl_2$ etching (Fig. 4a), and $\sigma = 0.3$ nm-rms for a subsequent 15 minutes of O_2/Ar etching (Fig. 4b). Linecuts are shown at y=0.5 μm to illustrate that O_2/Ar etching does not noticeably roughen the surface. The $ArCl_2$ etch rate was determined by measuring the membrane thickness before and after etching using a scanning electron microscope (SEM) (example image in Fig. 4c), resulting in 2.2 ± 0.7 μm/hr. The O_2/Ar etch rate was instead determined by measuring the height of pillars formed due to contaminant masking, yielding 4.2 ± 0.2 μm/hr. At each step of the fabrication process, the membrane is observed under an optical microscope to check for signs of visible contamination or to assess bonding quality; an example image of a membrane bonded to a dielectric mirror is shown in Fig. 4d. Fringes in the center of the membrane are caused by interference of light inside the sample due to sample wedge, while fringes around the edge of the sample are due to interference of light between the bottom surface of the membrane and the mirror from imperfect bonding. One can thus conclude that nearly all of the membrane surface is well-bonded to the mirror. In general, we find that the fraction of bonded surface area increases for

thinner samples, where the high fraction seen in Fig. 4d is characteristic of most final devices.

Ion implantation takes place after an initial etch, with the goal of creating a layer of GeV centers with a well-defined density and depth. This is important for open cavity systems as it allows for deterministic placement of defects at a fixed distance from the mirror interface (corresponding to an electric field antinode), which ensures maximum coupling to the cavity mode. The density can be controlled by tuning the implantation fluence with respect to the conversion efficiency, while the depth and straggle are determined by the acceleration energy used (parameters can be calculated with SRIM software [120]). The target depth will depend on whether the mirror has cavity electric field node at the diamond-mirror interface (high-index terminated Bragg stack, where the first cavity electric field antinode occurs at a depth of $\lambda/(4n_d)$ into the diamond), or whether the mirror has an antinode at this interface (low-index terminated Bragg stack, will have the first antinode at a depth of $\lambda/(2n_d)$).

After implantation, membranes are boiled in a triacid solution (1:1:1 sulfuric, nitric, and perchloric acids) for one hour to clean the surface before annealing. The samples used in this thesis were annealed following a three step recipe developed for NV centers [121], after which they were cleaned again in a triacid solution to remove graphitic carbon. Once annealed, the membranes are flipped and etched to the desired thickness on sapphire carrier wafers. The samples are subsequently boiled in a piranha mixture to release the diamond from the carrier substrate and transferred in a water droplet onto a flat mirror (implanted side down). At this point, the cavity materials are ready for assembly.

This chapter motivated the use of germanium vacancy centers coupled to Fabry-Pérot microcavities as a platform for creating a coherent spin-photon interface. The basic theory pertaining to the defect and cavity systems was outlined, and details were provided on device fabrication. Chapter 2 (based on reference [116]) comprises a detailed numeric and analytic study of the cavity mode structure, including different loss mechanisms. Chapter 3 (manuscript in preparation) describes the coupling of a single GeV center to a cavity at room temperature, resulting in an increased spectral density in emission. Finally, Chapter 4 (based on reference [122]) discusses active stabilization of the cavity length to within a cavity resonance. These works are followed by a general discussion of the results, and future directions for the project.

References

1. Simon, D. R. On the power of quantum computation. *SIAM Journal on Computing* **26,** 1474 (1997).
2. Shor, P. W. *Algorithms for quantum computation: Discrete logarithms and factoring* in *Proceedings 35th Annual Symposium on Foundations of Computer Science* (1994), 124.
3. Childs, A. M., Maslov, D., Nam, Y., Ross, N. J. & Su, Y. Toward the first quantum simulation with quantum speedup. *Proceedings of the National Academy of Sciences* **115,** 9456 (2018).
4. Feynman, R. P. Simulating physics with computers. *International Journal of Theoretical Physics* **21,** 467 (1982).
5. Gisin, N., Ribordy, G., Tittel, W. & Zbinden, H. Quantum cryptography. *Reviews of Modern Physics* **74,** 145 (2002).
6. Ekert, A. K. Quantum cryptography based on Bell's theorem. *Physical Review Letters* **67,** 661 (1991).
7. Scarani, V., Bechmann-Pasquinucci, H., Cerf, N. J., Dušek, M., Lütkenhaus, N. & Peev, M. The security of practical quantum key distribution. *Reviews of Modern Physics* **81,** 1301 (2009).
8. DiVincenzo, D. P. The physical implementation of quantum computation. *Fortschritte der Physik: Progress of Physics* **48,** 771 (2000).
9. Kelly, J. *Engineering superconducting qubit arrays for Quantum Supremacy* in *APS Meeting Abstracts* (2018).
10. Gisin, N. & Thew, R. Quantum communication. *Nature Photonics* **1,** 165 (2007).
11. Spiller, T. P., Nemoto, K., Braunstein, S. L., Munro, W. J., van Loock, P. & Milburn, G. J. Quantum computation by communication. *New Journal of Physics* **8,** 30 (2006).
12. Kimble, H. J. The quantum internet. *Nature* **453,** 1023 (2008).
13. Wehner, S., Elkouss, D. & Hanson, R. Quantum internet: A vision for the road ahead. *Science* **362,** eaam9288 (2018).

14. Monroe, C. Quantum information processing with atoms and photons. *Nature* **416,** 238 (2002).

15. Berman, P. R. *Cavity quantum electrodynamics* (Academic Press, 1994).

16. Hammerer, K., Sørensen, A. S. & Polzik, E. S. Quantum interface between light and atomic ensembles. *Reviews of Modern Physics* **82,** 1041 (2010).

17. Sangouard, N., Simon, C., De Riedmatten, H. & Gisin, N. Quantum repeaters based on atomic ensembles and linear optics. *Reviews of Modern Physics* **83,** 33 (2011).

18. Inlek, I., Crocker, C., Lichtman, M., Sosnova, K. & Monroe, C. Multispecies trapped-ion node for quantum networking. *Physical Review Letters* **118,** 250502 (2017).

19. Wang, Y., Um, M., Zhang, J., An, S., Lyu, M., Zhang, J.-N., Duan, L.-M., Yum, D. & Kim, K. Single-qubit quantum memory exceeding ten-minute coherence time. *Nature Photonics* **11,** 646 (2017).

20. Ye, J., Vernooy, D. & Kimble, H. Trapping of single atoms in cavity QED. *Physical Review Letters* **83,** 4987 (1999).

21. Harlander, M., Brownnutt, M., Hänsel, W. & Blatt, R. Trapped-ion probing of light-induced charging effects on dielectrics. *New Journal of Physics* **12,** 093035 (2010).

22. Ritter, S., Nölleke, C., Hahn, C., Reiserer, A., Neuzner, A., Uphoff, M., Mücke, M., Figueroa, E., Bochmann, J. & Rempe, G. An elementary quantum network of single atoms in optical cavities. *Nature* **484,** 195 (2012).

23. Santori, C., Fattal, D. & Yamamoto, Y. *Single-photon devices and applications* (John Wiley & Sons, 2010).

24. Brunner, D., Gerardot, B. D., Dalgarno, P. A., Wüst, G., Karrai, K., Stoltz, N. G., Petroff, P. M. & Warburton, R. J. A coherent single-hole spin in a semiconductor. *Science* **325,** 70 (2009).

25. Delteil, A., Sun, Z., Gao, W.-b., Togan, E., Faelt, S. & Imamoğlu, A. Generation of heralded entanglement between distant hole spins. *Nature Physics* **12,** 218 (2016).

26. Afzelius, M., Cone, R., Chanelière, T., Kröll, S., Moiseev, S., Sellars, M., *et al.* Photon-echo quantum memory. *arXiv preprint arXiv:0810.0172* (2008).

27. Sinclair, N., Oblak, D., Thiel, C. W., Cone, R. L. & Tittel, W. Properties of a rare-earth-ion-doped waveguide at sub-kelvin temperatures for quantum signal processing. *Physical Review Letters* **118,** 100504 (2017).

28. Lvovsky, A. I., Sanders, B. C. & Tittel, W. Optical quantum memory. *Nature Photonics* **3,** 706 (2009).

29. Wesenberg, J. H., Mølmer, K., Rippe, L. & Kröll, S. Scalable designs for quantum computing with rare-earth-ion-doped crystals. *Physical Review A* **75,** 012304 (2007).

30. Longdell, J., Sellars, M. & Manson, N. Demonstration of conditional quantum phase shift between ions in a solid. *Physical Review Letters* **93,** 130503 (2004).

31. Usmani, I., Clausen, C., Bussières, F., Sangouard, N., Afzelius, M. & Gisin, N. Heralded quantum entanglement between two crystals. *Nature Photonics* **6,** 234 (2012).

32. Kolesov, R., Xia, K., Reuter, R., Stöhr, R., Zappe, A., Meijer, J., Hemmer, P. & Wrachtrup, J. Optical detection of a single rare-earth ion in a crystal. *Nature Communications* **3,** 1029 (2012).

33. Siyushev, P., Xia, K., Reuter, R., Jamali, M., Zhao, N., Yang, N., Duan, C., Kukharchyk, N., Wieck, A., Kolesov, R., *et al.* Coherent properties of single rare-earth spin qubits. *Nature communications* **5,** 3895 (2014).

34. Yin, C., Rancic, M., de Boo, G. G., Stavrias, N., McCallum, J. C., Sellars, M. J. & Rogge, S. Optical addressing of an individual erbium ion in silicon. *Nature* **497,** 91 (2013).

35. Balasubramanian, G., Neumann, P., Twitchen, D., Markham, M., Kolesov, R., Mizuochi, N., Isoya, J., Achard, J., Beck, J., Tissler, J., *et al.* Ultralong spin coherence time in isotopically engineered diamond. *Nature Materials* **8,** 383 (2009).

36. Maurer, P. C. *et al.* Room-temperature quantum bit memory exceeding one second. *Science* **336,** 1283 (2012).

37. Dutt, M. G., Childress, L., Jiang, L., Togan, E., Maze, J., Jelezko, F., Zibrov, A., Hemmer, P. & Lukin, M. Quantum register based on individual electronic and nuclear spin qubits in diamond. *Science* **316,** 1312 (2007).

38. Rose, B. C., Huang, D., Zhang, Z.-H., Stevenson, P., Tyryshkin, A. M., Sangtawesin, S., Srinivasan, S., Loudin, L., Markham, M. L., Edmonds, A. M., *et al.* Observation of an environmentally insensitive solid-state spin defect in diamond. *Science* **361,** 60 (2018).

39. Thiering, G. & Gali, A. Ab initio magneto-optical spectrum of group-IV vacancy color centers in diamond. *Physical Review X* **8,** 021063 (2 2018).

40. Iwasaki, T., Miyamoto, Y., Taniguchi, T., Siyushev, P., Metsch, M. H., Jelezko, F. & Hatano, M. Tin-vacancy quantum emitters in diamond. *Physical Review Letters* **119,** 253601 (2017).

41. Trusheim, M. E., Wan, N. H., Chen, K. C., Ciccarino, C. J., Flick, J., Sundararaman, R., Malladi, G., Bersin, E., Walsh, M., Lienhard, B., *et al.* Lead-related quantum emitters in diamond. *Physical Review B* **99,** 075430 (2019).

42. Bar-Gill, N., Pham, L. M., Jarmola, A., Budker, D. & Walsworth, R. L. Solid-state electronic spin coherence time approaching one second. *Nature Communications* **4,** 1743 (2013).

43. Doherty, M. W., Manson, N. B., Delaney, P., Jelezko, F., Wrachtrup, J. & Hollenberg, L. C. The nitrogen-vacancy colour centre in diamond. *Physics Reports* **528,** 1 (2013).

44. Jelezko, F., Gaebel, T., Popa, I., Gruber, A. & Wrachtrup, J. Observation of coherent oscillations in a single electron spin. *Physical Review Letters* **92,** 076401 (2004).

45. Childress, L., Dutt, M. G., Taylor, J., Zibrov, A., Jelezko, F., Wrachtrup, J., Hemmer, P. & Lukin, M. Coherent dynamics of coupled electron and nuclear spin qubits in diamond. *Science* **314,** 281 (2006).

46. Rong, X., Geng, J., Shi, F., Liu, Y., Xu, K., Ma, W., Kong, F., Jiang, Z., Wu, Y. & Du, J. Experimental fault-tolerant universal quantum gates with solid-state spins under ambient conditions. *Nature Communications* **6,** 8748 (2015).

47. Maze, J. R., Gali, A., Togan, E., Chu, Y., Trifonov, A., Kaxiras, E. & Lukin, M. D. Properties of nitrogen-vacancy centers in diamond: the group theoretic approach. *New Journal of Physics* **13,** 025025 (2011).

48. Doherty, M. W., Manson, N. B., Delaney, P. & Hollenberg, L. C. The negatively charged nitrogen-vacancy centre in diamond: the electronic solution. *New Journal of Physics* **13,** 025019 (2011).

49. Robledo, L., Childress, L., Bernien, H., Hensen, B., Alkemade, P. F. A. & Hanson, R. High-fidelity projective read-out of a solid-state spin quantum register. *Nature* **477,** 574 (2011).

50. Togan, E. *et al.* Quantum entanglement between an optical photon and a solid-state spin qubit. *Nature* **466,** 730 (2010).

51. Bernien, H., Childress, L., Robledo, L., Markham, M., Twitchen, D. & Hanson, R. Two-photon quantum interference from separate nitrogen vacancy centers in diamond. *Physical Review Letters* **108,** 043604 (2012).

52. Sipahigil, A., Goldman, M. L., Togan, E., Chu, Y., Markham, M., Twitchen, D. J., Zibrov, A. S., Kubanek, A. & Lukin, M. D. Quantum interference of single photons from remote nitrogen-vacancy centers in diamond. *Physical Review Letters* **108,** 143601 (2012).

53. Hensen, B. *et al.* Loophole-free Bell inequality violation using electron spins separated by 1.3 kilometres. *Nature* **526,** 682 (2015).

54. Bernien, H., Hensen, B., Pfaff, W., Koolstra, G., Blok, M., Robledo, L., Taminiau, T., Markham, M., Twitchen, D., Childress, L., *et al.* Heralded entanglement between solid-state qubits separated by three metres. *Nature* **497,** 86 (2013).

55. Pfaff, W., Hensen, B., Bernien, H., van Dam, S. B., Blok, M. S., Taminiau, T. H., Tiggelman, M. J., Schouten, R. N., Markham, M., Twitchen, D. J., *et al.* Unconditional quantum teleportation between distant solid-state quantum bits. *Science* **345,** 532 (2014).

56. Kalb, N., Reiserer, A. A., Humphreys, P. C., Bakermans, J. J. W., Kamerling, S. J., Nickerson, N. H., Benjamin, S. C., Twitchen, D. J., Markham, M. & Hanson, R. Entanglement distillation between solid-state quantum network nodes. *Science* **356,** 928 (2017).

57. Humphreys, P. C., Kalb, N., Morits, J. P. J., Schouten, R. N., Vermeulen, R. F. L., Twitchen, D. J., Markham, M. & Hanson, R. Deterministic delivery of remote entanglement on a quantum network. *Nature* **558,** 268 (2018).

58. Wolters, J., Sadzak, N., Schell, A. W., Schröder, T. & Benson, O. Measurement of the ultrafast spectral diffusion of the optical transition of nitrogen vacancy centers in nano-size diamond using correlation interferometry. *Physical Review Letters* **110,** 027401 (2013).

59. Tamarat, P., Gaebel, T., Rabeau, J., Khan, M., Greentree, A., Wilson, H., Hollenberg, L., Prawer, S., Hemmer, P., Jelezko, F., *et al.* Stark shift control of single optical centers in diamond. *Physical Review Letters* **97,** 083002 (2006).

60. Sipahigil, A. & Lukin, M. D. Quantum optics with diamond color centers coupled to nanophotonic devices. *arXiv preprint arXiv:1712.06693* (2017).

61. Rogers, L. J., Jahnke, K. D., Teraji, T., Marseglia, L., Müller, C., Naydenov, B., Schauffert, H., Kranz, C., Isoya, J., McGuinness, L. P., *et al.* Multiple intrinsically identical single-photon emitters in the solid state. *Nature Communications* **5,** 4739 (2014).

62. Siyushev, P. *et al.* Optical and microwave control of germanium-vacancy center spins in diamond. *Physical Review B* **96,** 081201 (2017).

63. Evans, R. E., Sipahigil, A., Sukachev, D. D., Zibrov, A. S. & Lukin, M. D. Narrow-linewidth homogeneous optical emitters in diamond nanostructures via silicon ion implantation. *Physical Review Applied* **5,** 044010 (2016).

64. Gali, A. & Maze, J. R. Ab initio study of the split silicon-vacancy defect in diamond: Electronic structure and related properties. *Physical Review B* **88,** 235205 (2013).

65. Palyanov, Y. N., Kupriyanov, I. N., Borzdov, Y. M. & Surovtsev, N. V. Germanium: a new catalyst for diamond synthesis and a new optically active impurity in diamond. *Scientific Reports* **5,** 14789 (2015).

66. Neu, E., Steinmetz, D., Riedrich-Möller, J., Gsell, S., Fischer, M., Schreck, M. & Becher, C. Single photon emission from silicon-vacancy colour centres in chemical vapour deposition nano-diamonds on iridium. *New Journal of Physics* **13,** 025012 (2011).

67. E. M. Purcell. Spontaneous Emission Probabilities at Radio Frequencies. *Physical Review* **69,** 681 (1946).

68. Barclay, P. E., Fu, K.-M. C., Santori, C., Faraon, A. & Beausoleil, R. G. Hybrid nanocavity resonant enhancement of color center emission in diamond. *Physical Review X* **1,** 011007 (2011).

69. Burek, M. J., Meuwly, C., Evans, R. E., Bhaskar, M. K., Sipahigil, A., Meesala, S., Machielse, B., Sukachev, D. D., Nguyen, C. T., Pacheco, J. L., *et al.* Fiber-coupled diamond quantum nanophotonic interface. *Physical Review Applied* **8,** 024026 (2017).

70. Hausmann, B. J. M., Shields, B. J., Quan, Q., Chu, Y., de Leon, N. P., Evans, R., Burek, M. J., Zibrov, A. S., Markham, M., Twitchen, D., *et al.* Coupling of NV centers to photonic crystal nanobeams in diamond. *Nano Letters* **13,** 5791 (2013).

71. Li, L., Schröder, T., Chen, E. H., Walsh, M., Bayn, I., Goldstein, J., Gaathon, O., Trusheim, M. E., Lu, M., Mower, J., *et al.* Coherent spin control of a nanocavity-enhanced qubit in diamond. *Nature Communications* **6,** 6173 (2015).

72. Faraon, A., Santori, C., Huang, Z., Acosta, V. M. & Beausoleil, R. G. Coupling of nitrogen-vacancy centers to photonic crystal cavities in monocrystalline diamond. *Physical Review Letters* **109,** 033604 (2012).

73. Burek, M. J., Chu, Y., Liddy, M. S., Patel, P., Rochman, J., Meesala, S., Hong, W., Quan, Q., Lukin, M. D. & Lončar, M. High quality-factor optical nanocavities in bulk single-crystal diamond. *Nature Communications* **5,** 5718 (2014).

74. Santori, C., Barclay, P. E., Fu, K.-M. C. & Beausoleil, R. G. Vertical distribution of nitrogen-vacancy centers in diamond formed by ion implantation and annealing. *Physical Review B* **79,** 125313 (2009).

75. Sipahigil, A., Evans, R. E., Sukachev, D. D., Burek, M. J., Borregaard, J., Bhaskar, M. K., Nguyen, C. T., Pacheco, J. L., Atikian, H. A., Meuwly, C., *et al.* An integrated diamond nanophotonics platform for quantum-optical networks. *Science* **354,** 847 (2016).

76. Evans, R. E., Bhaskar, M. K., Sukachev, D. D., Nguyen, C. T., Sipahigil, A., Burek, M. J., Machielse, B., Zhang, G. H., Zibrov, A. S., Bielejec, E., *et al.* Photon-mediated interactions between quantum emitters in a diamond nanocavity. *Science* **362,** 662 (2018).

77. Bhaskar, M. K., Sukachev, D. D., Sipahigil, A., Evans, R. E., Burek, M. J., Nguyen, C. T., Rogers, L. J., Siyushev, P., Metsch, M. H., Park, H., *et al.* Quantum nonlinear optics with a germanium-vacancy color center in a nanoscale diamond waveguide. *Physical Review Letters* **118,** 223603 (2017).

78. Schröder, T., Trusheim, M. E., Walsh, M., Li, L., Zheng, J., Schukraft, M., Sipahigil, A., Evans, R. E., Sukachev, D. D., Nguyen, C. T., *et al.* Scalable focused ion beam creation of nearly lifetime-limited single quantum emitters in diamond nanostructures. *Nature Communications* **8,** 15376 (2017).

79. Mosor, S., Hendrickson, J., Richards, B., Sweet, J., Khitrova, G., Gibbs, H., Yoshie, T., Scherer, A., Shchekin, O. & Deppe, D. Scanning a photonic crystal slab nanocavity by condensation of xenon. *Applied Physics Letters* **87,** 141105 (2005).

80. Hood, C. J., Kimble, H. & Ye, J. Characterization of high-finesse mirrors: Loss, phase shifts, and mode structure in an optical cavity. *Physical Review A* **64,** 033804 (2001).

81. Hunger, D., Steinmetz, T., Colombe, Y., Deutsch, C., Hänsch, T. W. & Reichel, J. A fiber Fabry–Perot cavity with high finesse. *New Journal of Physics* **12,** 065038 (2010).

82. Miguel-Sánchez, J., Reinhard, A., Togan, E., Volz, T., Imamoglu, A., Besga, B., Reichel, J. & Estève, J. Cavity quantum electrodynamics with charge-controlled quantum dots coupled to a fiber Fabry–Perot cavity. *New Journal of Physics* **15,** 045002 (2013).

83. Haas, F., Volz, J., Gehr, R., Reichel, J. & Estève, J. Entangled states of more than 40 atoms in an optical fiber cavity. *Science* **344,** 180 (2014).

84. Steiner, M., Meyer, H. M., Deutsch, C., Reichel, J. & Köhl, M. Single ion coupled to an optical fiber cavity. *Physical Review Letters* **110,** 043003 (4 2013).

85. Ballance, T. G., Meyer, H. M., Kobel, P., Ott, K., Reichel, J. & Köhl, M. Cavity-induced backaction in Purcell-enhanced photon emission of a single ion in an ultraviolet fiber cavity. *Physical Review A* **95,** 033812 (3 2017).

86. Mader, M., Reichel, J., Hänsch, T. W. & Hunger, D. A scanning cavity microscope. *Nature Communications* **6,** 7249 (2015).

87. Zhong, H., Fläschner, G., Schwarz, A., Wiesendanger, R., Christoph, P., Wagner, T., Bick, A., Staarmann, C., Abeln, B., Sengstock, K., *et al.* A millikelvin all-fiber cavity optomechanical apparatus for merging with ultra-cold atoms in a hybrid quantum system. *Review of Scientific Instruments* **88,** 023115 (2017).

88. Hümmer, T., Noe, J., Hofmann, M. S., Hänsch, T. W., Högele, A. & Hunger, D. Cavity-enhanced Raman microscopy of individual carbon nanotubes. *Nature Communications* **7,** 12155 (2016).

89. Albrecht, R., Bommer, A., Deutsch, C., Reichel, J. & Becher, C. Coupling of a single nitrogen-vacancy center in diamond to a fiber-based microcavity. *Physical Review Letters* **110,** 243602 (24 2013).

90. Benedikter, J., Kaupp, H., Hümmer, T., Liang, Y., Bommer, A., Becher, C., Krueger, A., Smith, J. M., Hänsch, T. W. & Hunger, D. Cavity-enhanced single-photon source based on the silicon-vacancy center in diamond. *Physical Review Applied* **7,** 024031 (2 2017).

91. Jantzen, U., Kurz, A. B., Rudnicki, D. S., Schäfermeier, C., Jahnke, K. D., Andersen, U. L., Davydov, V. A., Agafonov, V. N., Kubanek, A., Rogers, L. J., *et al.* Nanodiamonds carrying silicon-vacancy quantum emitters with almost lifetime-limited linewidths. *New Journal of Physics* **18,** 073036 (2016).

92. Riedel, D., Söllner, I., Shields, B. J., Starosielec, S., Appel, P., Neu, E., Maletinsky, P. & Warburton, R. J. Deterministic enhancement of coherent photon generation from a nitrogen-vacancy center in ultrapure diamond. *Physical Review X* **7,** 031040 (2017).

93. Van Dam, S. B., Walsh, M., Degen, M. J., Bersin, E., Mouradian, S. L., Galiullin, A., Ruf, M., IJspeert, M., Taminiau, T. H., Hanson, R., *et al.* Optical coherence of diamond nitrogen-vacancy centers formed by ion implantation and annealing. *arXiv preprint arXiv:1812.11523* (2018).

94. Ruf, M., IJspeert, M., van Dam, S., de Jong, N., van den Berg, H., Evers, G. & Hanson, R. Optically coherent nitrogen-vacancy centers in μm-thin etched diamond membranes. *Nano Letters* **19,** 3987 (2019).

95. Nemoto, K., Trupke, M., Devitt, S. J., Stephens, A. M., Scharfenberger, B., Buczak, K., Nöbauer, T., Everitt, M. S., Schmiedmayer, J. & Munro, W. J. Photonic architecture for scalable quantum information processing in diamond. *Physical Review X* **4,** 031022 (3 2014).

96. Nemoto, K., Trupke, M., Devitt, S. J., Scharfenberger, B., Buczak, K., Schmiedmayer, J. & Munro, W. J. Photonic quantum networks formed from NV- centers. *Scientific Reports* **6,** 26284 (2016).

97. Goss, J. P., Briddon, P. R., Rayson, M. J., Sque, S. J. & Jones, R. Vacancy-impurity complexes and limitations for implantation doping of diamond. *Physical Review B* **72,** 035214 (3 2005).

98. Goss, J. P., Briddon, P. R. & Shaw, M. J. Density functional simulations of silicon-containing point defects in diamond. *Physical Review B* **76,** 075204 (7 2007).

99. Iwasaki, T. *et al.* Germanium-vacancy single color centers in diamond. *Scientific Reports* **5,** 12882 (2015).

100. Palyanov, Y. N., Kupriyanov, I. N., Borzdov, Y. M., Khokhryakov, A. F. & Surovtsev, N. V. High-pressure synthesis and characterization of Ge-doped single crystal diamond. *Crystal Growth & Design* **16,** 3510 (2016).

101. Haussler, S. *et al.* Photoluminescence excitation spectroscopy of SiV- and GeV-color center in diamond. *New Journal of Physics* **19,** 063036 (2017).

102. Ekimov, E. A., Lyapin, S., Boldyrev, K. N., Kondrin, M. V., Khmelnitskiy, R., Gavva, V. A., Kotereva, T. V. & Popova, M. N. Germanium–vacancy color center in isotopically enriched diamonds synthesized at high pressures. *Journal of Experimental and Theoretical Physics* **102,** 701 (2015).

103. Boldyrev, K., Mavrin, B., Sherin, P. S. & Popova, M. Bright luminescence of diamonds with Ge-V centers. *Journal of Luminescence* **193,** 119 (2018).

104. Solin, S. A. & Ramdas, A. K. Raman spectrum of diamond. *Physical Review B* **1,** 1687 (4 1970).

105. Hepp, C. *et al.* Electronic structure of the silicon vacancy color center in diamond. *Physical Review Letters* **112,** 036405 (3 2014).

106. Sukachev, D. D., Sipahigil, A., Nguyen, C. T., Bhaskar, M. K., Evans, R. E., Jelezko, F. & Lukin, M. D. Silicon-vacancy spin qubit in diamond: a quantum memory exceeding 10 ms with single-shot state readout. *Physical Review Letters* **119,** 223602 (2017).

107. Jahnke, K. D., Sipahigil, A., Binder, J. M., Doherty, M. W., Metsch, M., Rogers, L. J., Manson, N. B., Lukin, M. D. & Jelezko, F. Electron–phonon processes of the silicon-vacancy centre in diamond. *New Journal of Physics* **17,** 043011 (2015).

108. Fox, M. *Quantum optics: an introduction* (OUP Oxford, 2006).

109. Griffiths, D. J. & Schroeter, D. F. *Introduction to quantum mechanics* (Cambridge University Press, 2018).

110. Albrecht, R., Bommer, A., Pauly, C., Mücklich, F., Schell, A. W., Engel, P., Schröder, T., Benson, O., Reichel, J. & Becher, C. Narrow-band single photon emission at room temperature based on a single nitrogen-vacancy center coupled to an all-fiber-cavity. *Applied Physics Letters* **105,** 073113 (2014).

111. Johnson, S., Dolan, P., Grange, T., Trichet, A., Hornecker, G., Chen, Y.-C., Weng, L., Hughes, G., Watt, A., Auffèves, A., *et al.* Tunable cavity coupling of the zero phonon line of a nitrogen-vacancy defect in diamond. *New Journal of Physics* **17,** 122003 (2015).

112. Dolan, P. R., Hughes, G. M., Grazioso, F., Patton, B. R. & Smith, J. M. Femtoliter tunable optical cavity arrays. *Optics Letters* **35,** 3556 (2010).

113. Hunger, D., Deutsch, C., Barbour, R. J., Warburton, R. J. & Reichel, J. Laser microfabrication of concave, low-roughness features in silica. *AIP Advances* **2,** 012119 (2012).

114. Bennett, J. M. Recent developments in surface roughness characterization. *Measurement Science and Technology* **3,** 1119 (1992).

115. Najer, D., Renggli, M., Riedel, D., Starosielec, S. & Warburton, R. J. Fabrication of mirror templates in silica with micron-sized radii of curvature. *Applied Physics Letters* **110,** 011101 (2017).

116. Janitz, E., Ruf, M., Dimock, M., Bourassa, A., Sankey, J. & Childress, L. Fabry-Perot microcavity for diamond-based photonics. *Physical Review A* **92,** 043844 (2015).

117. Maletinsky, P., Hong, S., Grinolds, M. S., Hausmann, B., Lukin, M. D., Walsworth, R. L., Loncar, M. & Yacoby, A. A robust scanning diamond sensor for nanoscale imaging with single nitrogen-vacancy centres. *Nature Nanotechnology* **7,** 320 (2012).

118. Latawiec, P., Venkataraman, V., Burek, M. J., Hausmann, B. J., Bulu, I. & Lončar, M. On-chip diamond Raman laser. *Optica* **2,** 924 (2015).

119. Cui, S. *Near-surface Nitrogen Vacancy Centers in Diamond* PhD thesis (2014).

120. Ziegler, J. F., Ziegler, M. D. & Biersack, J. P. SRIM–The stopping and range of ions in matter. *Nuclear Instruments and Methods in Physics Research Section B: Beam Interactions with Materials and Atoms* **268,** 1818 (2010).

121. Chu, Y. *et al.* Coherent optical transitions in implanted nitrogen vacancy centers. *Nano Letters* **14,** 1982 (2014).

122. Janitz, E., Ruf, M., Fontana, Y., Sankey, J. & Childress, L. High mechanical bandwidth fiber-coupled Fabry-Perot cavity. *Optics Express* **25,** 20932 (2017).

Preface to Chapter 2

In this manuscript, we outline the fabrication and characterization of a high-quality-factor Fabry-Pérot microcavity containing a diamond membrane. We study the modified spectrum of the membrane-in-cavity device, developing numeric and analytic models to describe the mode structure. Moreover, we look at the impact of different losses in the system and estimate the Purcell enhancement that could be achieved. Elucidation of the electric field distribution is critical for calculating emitter-cavity coupling rates for such systems, making this work an important milestone toward an efficient optical interface for defects in diamond.

2

Fabry-Perot Microcavity for Diamond-Based Photonics

Erika Janitz, Maximilian Ruf, Mark Dimock, Alexandre Bourassa, Jack Sankey, and Lilian Childress

Department of Physics, McGill University, Montreal CA

This chapter has been published in Physical Review A.
Journal reference: Physical Review A **92**, 043844 (2015).

Abstract

Open Fabry-Perot microcavities represent a promising route for achieving a quantum electrodynamics (cavity-QED) platform with diamond-based emitters. In particular, they offer the opportunity to introduce high purity, minimally fabricated material into a tunable, high quality factor optical resonator. Here, we demonstrate a fiber-based microcavity incorporating a thick (> 10 μm) diamond membrane with a finesse of $17,000$, corresponding to a quality factor $Q \sim 10^6$. Such minimally fabricated, thick samples can contain optically stable emitters similar to those found in bulk diamond. We observe modified microcavity spectra in the presence of the membrane, and develop analytic and numerical models to describe the effect of the membrane on cavity modes, including loss and coupling to higher-order transverse modes. We estimate that a Purcell enhancement of approximately 20 should be possible for emitters within the diamond in this device, and provide evidence that better diamond surface treatments and mirror coatings could increase this value to 200 in a realistic system.

2.1 Introduction

The field of diamond photonics has seen tremendous growth over the last decade [1, 2], spurred by new applications of optically active defect centers in metrology [3, 4] and quantum information science [5, 6]. In particular, the nitrogen-vacancy (NV) defect [7] exhibits long spin coherence times and narrow optical transitions favorable for realizing a solid-state cavity-QED system. In pursuit of this goal, much progress has been made in fabricating low-mode-volume cavities in diamond itself [2, 8–10], and Purcell enhancement of the NV zero phonon line as large as 70 has been observed in a diamond photonic crystal cavity [11]. A complementary strategy is to confine the defect in an open Fabry-Perot microcavity [12, 13], which provides in-situ tunability and the possibility for very narrow cavity linewidths. Recently, three groups have observed coupling between an open cavity and an NV center in a nanocrystal [14–17].

A central challenge for diamond photonics is destabilization of defect optical transitions in close proximity to surfaces, especially for defects in nanocrystals or in nanofabricated devices [18]. For example, the aforementioned diamond photonic crystal cavity achieved its high Purcell factor at the expense of spectral diffusion of many GHz [11], far in excess of the near lifetime-limited linewidths of 13 MHz that can be observed in some type IIa samples [19]. While recent advances in surface treatments [20] and fabrication [21] hold promise for realizing optimal NV properties in nanophotonic structures, narrow linewidths are most reliably obtained microns into bulk diamond. The open cavities discussed here can accommodate the larger mode volumes required for such microns-thick samples: both their mode volume V and quality factor Q increase approximately linearly with length, so that the Purcell enhancement F_p depends only on the mirror finesse $\mathcal{F}$ and the ratio of the cavity waist w_0 to the resonant wavelength λ: $F_p \propto \mathcal{F}\lambda^2/w_0^2$ [12]. In addition, their linewidths are comparatively narrow and can be tuned over a wide range in-situ via the cavity length, potentially allowing exploration of spin-dependent coupling between an NV center and the cavity. Finally, by adjusting the positions of the mirrors, one can optimize the cavity mode spatial overlap with the emitter.

In principle, it is straightforward to incorporate a microns-thick membrane into an open cavity. However, for high finesse $\mathcal{F} > 10^4$ cavities, losses at the 100 ppm level are important. Absorption and scattering must be minimized, and changes in the cav-

ity mode induced by the dielectric interface must be considered. Here, we demonstrate that a fiber-based microcavity can maintain high finesse $\mathcal{F} \sim 17,000$ (quality factor $Q \sim 10^6$) while incorporating a > 10 μm thick diamond membrane compatible with high stability defect centers. We further develop a theoretical description for the longitudinal modes (including diffraction effects), and perturbatively estimate the mixing between transverse modes induced by the membrane. Based on our measurements, we predict our device should be capable of enhancing the NV zero phonon line by a factor of approximately 20.

2.2 The Fiber Cavity Device

We work with a fiber-based Fabry-Perot microcavity [12, 13] in a geometry similar to those used to study quantum dots [22] and molecules [23]. The microcavity system (Fig. 5a) consists of a concave mirror on the tip of a single mode optical fiber, and a macroscopic flat mirror to which we bond the diamond membrane. Compared with traditional optics, these fiber-based cavities offer advantages in stable alignment and efficient coupling to the single mode propagating in the fiber [12].

The fiber mirror substrate is fabricated using a CO_2 laser ablation process [12]. The ablation laser induces evaporation and melting of the glass on the fiber tip [24], resulting in an approximately Gaussian-shaped dimple (Fig. 5b) with an extremely low surface roughness of < 0.2 nm-rms, as measured with an atomic force microscope. By imaging the fiber core during ablation alignment, we achieve a placement repeatability of 0.5 μm for the ablation spot. The fiber used in our experiments is measured to have a power coupling efficiency to the cavity mode of $\epsilon^2 = 48 \pm 4\%$ (limited by mirror absorption as well as cavity and ablation misalignment, see Appendix 2.A), and an effective radius of curvature $R = 61.0 \pm 1.4$ μm (see Appendix 2.B).

The second mirror substrate is a superpolished macroscopic mirror flat with surface roughness below 0.1 nm-rms. The flat and fiber mirrors are coated with a dielectric mirror stack (LASEROPTIK) specified to have a transmission of 70 ± 10 ppm and < 24 ppm losses at $\lambda = 637$ nm; the theoretical finesse of the stack design is $53,100$. The fiber (stripped of all polymer jacketing) and flat mirrors were both annealed at 300°C for five hours under atmospheric conditions to reduce losses in the coatings [25].

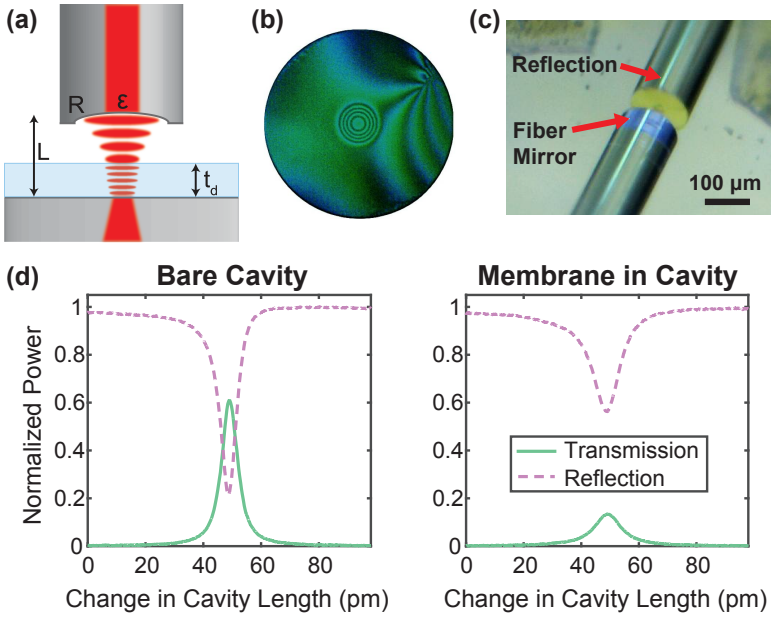

Figure 5: (Color online) (a) A schematic of the microcavity system illustrating the cavity length (L), mirror radius of curvature (R), diamond membrane thickness (t_d), and coupling efficiency (ϵ) between the fiber and cavity modes. (b) An interferometric image of an ablated fiber, where each subsequent dark fringe corresponds to a change in depth of ≈ 253 nm. (c) A microscope camera image of the fiber cavity mirror and reflection seen against the diamond membrane. Dark regions in the upper corners are due to partial etching of the mirror beneath the membrane, and some contamination of the diamond surface is also visible. (d) Measured transmission (solid line) and reflection (dashed line) curves for the bare cavity, and membrane-in-cavity configurations, normalized to the peak reflected power. These particular measurements correspond to finesses of $\mathcal{F}_L \approx 37,000 \pm 1000$ and $\mathcal{F}_L \approx 15,900 \pm 900$ for the bare cavity and membrane-in-cavity respectively.

The diamond membrane is fabricated from a $\langle 100 \rangle$-cut electronic grade single crystal diamond plate. The bulk diamond was laser cut laterally, producing 20 ± 10 μm thick diamond membranes polished to a surface roughness of approximately 5 nm-rms. One of the resulting membranes was cleaned in a piranha solution and bonded with Van der Waals forces to a silicon carrier wafer, and approximately 2 μm was etched from the membrane surface using an $ArCl_2$ inductively coupled plasma reactive ion etching (ICP RIE) recipe [26–28]. The etching process reduced the surface roughness to < 0.2 nm-rms (measured over one optical wavelength squared). The membrane was then removed from the carrier, similarly cleaned in piranha, etched on the other side (again removing

2 μm with $ArCl_2$), and finally bonded to the macroscopic mirror flat. Finally, a third $ArCl_2$ etch was performed to thin the membrane to approximately 10 μm.

To assemble the cavity, the mirror flat is fixed to a tip-tilt mount, while the fiber is clamped to a 3-axis manual and piezo stage. The tip-tilt mount enables angular alignment of the cavity mode, while the 3-axis stage allows for study of different regions of the membrane as well as precision control of the cavity length. Figure 5c shows an image of the assembled device.

2.3 Effect of the Membrane on Cavity Modes

2.3.1 *Cavity finesse*

Introducing the membrane into the cavity affects the linewidth of its resonances. To determine the cavity finesse, we scan the position of the fiber mirror while monitoring the cavity's transmission and reflection at a fixed wavelength near 637 nm (provided by a tunable diode laser). In this case, we define the finesse as the ratio of the free spectral range (FSR $\approx \lambda/2$) to the resonance full width half maximum (FWHM) measured as a function of the length of the cavity, and denote it by $\mathcal{F}_L$:

$$\mathcal{F}_L = \frac{\text{FSR in length}}{\text{FWHM in length}} \tag{2.1}$$

Note that for the membrane-in-cavity system, this is not necessarily the same as finesse obtained by measuring the resonance spacing and linewidth as a function of laser frequency.

We measure the finesse by first performing a long scan of the cavity length to observe the resonance spacing as a function of the voltage applied to the piezo stage. By scanning the length over about 20 μm (roughly 60 FSR), we can fit the observed resonances to extract the free spectral range and calibrate the piezo stage nonlinearity. Subsequent voltage scans over shorter length ranges (0.6 μm) provide high resolution data for extracting the cavity linewidth. At each position of interest, we measure 64 transmission and reflection peak data sets to gather statistics on the cavity linewidth. This procedure is followed for all measurements of $\mathcal{F}_L$ presented.

We characterize the transmission and reflection curves for the TEM_{00} fundamental mode using the same fiber mirror for an empty or "bare" cavity, and for a membrane-in-cavity, as illustrated by sample data sets in Fig. 5d. These measurements are corrected for calibrated losses in the measurement apparatus (outside of the cavity), and are normalized to the peak reflected power. To determine cavity linewidth, we fit the transmission and reflection data sets to Lorentzian and Fano lineshapes respectively; in practice, the reflection signal gives better signal to noise and was used to calculate cavity finesse. The asymmetric resonances seen in reflection can arise from a slight displacement of the ablation dimple from the fiber core (see Appendix 2.A).

As discussed below, the observed finesse varies with the length of the cavity, the transverse location on the membrane, and the frequency of the laser. At best, we observe a peak finesse of $\mathcal{F}_L \approx 37,000$ for the bare cavity and $\mathcal{F}_L \approx 17,000$ for the membrane-in-cavity setup. When we observe different locations on the flat mirror's surface, we find the finesse for the empty cavity typically fluctuates by a few thousand, most likely due to surface contamination or spatially-varying surface roughness. With the diamond present, however, the finesse fluctuates by a much larger factor, with no observable cavity resonances in many locations. At first glance one might presume these fluctuations arise from similar physics, i.e. roughness, contamination, or even crystal defects in the diamond itself. However, as discussed below, such large finesse fluctuations are primarily caused by spatial variations in the diamond layer thickness, which affects the cavity mode structure in an important and predictable way.

2.3.2 *Mode structure*

We characterize the cavity mode structure by illuminating the flat mirror with a broadband LED source, and measuring the spectrum of the light transmitted into the fiber with a grating spectrometer. By gathering data as a function of cavity length, we observe the evolution of multiple longitudinal and transverse modes (see Fig. 6a).

The measured white light spectrum exhibits a canted periodic structure that is markedly different from the behavior of a bare cavity. These features can be quantitatively reproduced by a simple one-dimensional (1D) model. We consider lossless mirrors at each end of the cavity, with a 180 degree phase shift on reflection (facing the cavity) to ap-

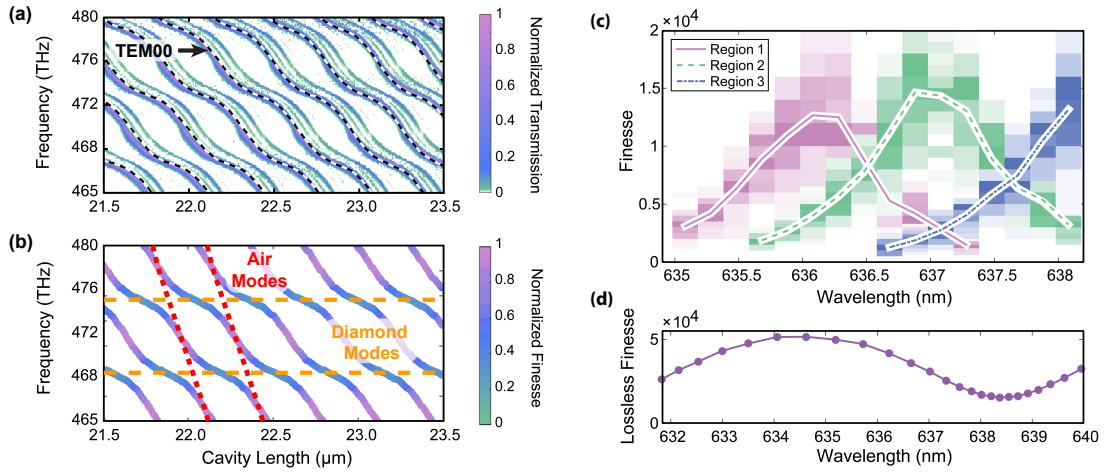

Figure 6: (Color online) (a) Cavity spectrum obtained by coupling a broadband LED through the flat mirror, and scanning the length of the cavity. An approximate analytic fit (Eq. 2.3) to the resonances is overlaid. The error in the x-axis calibration is ± 0.2 μm. (b) A numerical simulation of the normalized finesse $\mathcal{F}_L$ of the cavity resonances including the Guoy phase and mirror stack. Lines indicating the cavity resonances associated with air and diamond regions are overlaid to illustrate the avoided crossings. (c) Finesse vs. laser wavelength measured for three different regions of the diamond membrane, corresponding to different membrane thicknesses. The raw finesse data was binned using the Freedman-Diaconis rule to show the underlying distribution, and the binned data is shown through opacity. The mean finesse values are plotted as lines. (d) Simulated finesse vs. laser wavelength for a lossless cavity. The absence of scattering losses leads to high finesse over a much larger wavelength range.

proximate the dielectric mirror stack terminated at the high index material ($Ta_2 0_5$ in this case). Between the mirrors are a slab of diamond of thickness t_d and index n_d, and a layer of air with thickness $L - t_d$ and index $n_{air} = 1$ (see Fig. 5a). In the limit of perfect mirrors, the resonant frequencies ν are given by solutions to the transcendental equation

$$(1 + n_d) \sin\left(\frac{2\pi\nu}{c}\left(L + t_d(n_d - 1)\right)\right) = (1 - n_d) \sin\left(\frac{2\pi\nu}{c}\left(L - t_d(n_d + 1)\right)\right). \tag{2.2}$$

Note that while the resonances occur regularly every $c/2\nu$ as the length of the cavity shifts, the variation with frequency is less straightforward. For long cavities, encompass-

ing many nodes, Eq. 2.2 can be approximated by writing ν in terms of its deviation from an integer multiple m of the average free spectral range, $\nu = \delta\nu + mc/(2(L + (n_d - 1)t_d))$, and neglecting $\delta\nu$ in the right hand side (RHS) of Eq. 2.2 [29], yielding:

$$\nu \approx \frac{c}{2\pi\,(L + (n_d - 1)t_d)} \left\{ \pi m - (-1)^m \arcsin\left(\frac{n_d - 1}{n_d + 1} \sin\left(\frac{m\pi(L - (n_d + 1)t_d)}{L + (n_d - 1)t_d}\right)\right)\right\}. \tag{2.3}$$

Fitting Eq. 2.3 to the fundamental mode frequencies in the cavity spectrum results in an estimated membrane thickness of $t_d = 10.5 \pm 0.2$ μm and the cavity lengths given in the x-axis of Fig. 6a, where the fit results are shown by the dashed lines. Note that we fit resonances over the full 20 μm range of the stage (not shown) to produce these estimates, and included a cubic nonlinearity in the piezo stage response; the region displayed in the figure is representative of the goodness of fit. The fit deviations arise because the model neglects the transverse Gaussian field profile and Guoy phase of the cavity mode, which can lead to errors in the estimated length of up to half a FSR ($\lambda/4$) [1]. The fit also allows us to determine the cavity length during transmission and reflection measurements, albeit with an increased uncertainty (roughly ± 0.3 μm) [2].

The model also provides some intuition about the system. If the membrane-air interface were perfectly reflective (i.e. $n_d \to \infty$), it would divide the cavity into two, and the normal modes would separate into "diamond" modes and "air" modes, wherein the field is entirely localized in either the diamond or air, respectively. Since the diamond thickness is fixed, the diamond mode frequencies (horizontal lines in Fig. 6b) would not depend on the longitudinal position of the fiber mirror, while the air modes would decrease in frequency as the air gap increases in length (slanted lines in Fig. 6b). Indeed the frequency spacings for these modes would reveal the diamond thickness and cavity length: $\Delta\nu_{di} = \frac{c}{2\,n_d\,t_d}$, and $\Delta\nu_{air} = \frac{c}{2\,(L - t_d)}$ for the diamond and air modes re-

1 A significantly more complicated analytic expression including the Guoy phase and transverse mode profile was also derived, but due to the equation complexity and other systematic measurement errors (including stage drift and nonlinearity), the latter model did not improve precision of the membrane thickness and cavity length estimates.

2 The increased uncertainty arises because the LED used to obtain the white-light spectrum heats the cavity, and we must allow it to attain thermal equilibrium before acquiring data. We track length changes as the structure warms, but can only calibrate them within $\sim \pm\lambda/4$.

spectively. With finite n_d, these modes are coupled to one another, leading to the large avoided crossings observed in the spectrum; "diamond-like" modes have a shallow slope, while the "air-like" modes have a steeper slope. This behavior is very similar to that of a membrane-in-the-middle system [29], where the air-diamond dielectric interface plays the role of a weakly reflective, vanishingly thin membrane.

Our analysis above focused on the fundamental mode, and indeed, for an ideal spherical ablation dimple, light from the fiber core should couple primarily to the Gaussian TEM_{00} mode. Nevertheless, some higher order modes are also visible in the spectrum. Similar features observed in the white-light spectrum for the bare cavity are used to extract the effective radius of curvature of the fiber mirror ($R = 61.0 \pm 1.4$ μm), as noted in section 2.2 and detailed in Appendix 2.B.

In addition to the analytic 1D model used to find the cavity resonance frequencies, we developed a numerical three-dimensional model for the cavity modes that incorporates wavefront curvature within the cavity and the full dielectric mirror stack. This model includes an approximation that the air-diamond interface follows the curvature of the Gaussian wavefronts, in order to prevent coupling between transverse modes via refraction. Figure 6b shows simulated cavity resonances in the absence of any loss, calculated over the same length and frequency range as the white light transmission data. The cavity parameters used are those extracted from the fit in Fig. 6a, and full calculation details are provided in Appendix 2.C. The color of each data point shows the calculated value of $\mathcal{F}_L$ normalized to the naive finesse estimate of $\frac{\pi}{T}$, where T is transmission per pass of one mirror, and all other loss processes are neglected. The highest finesse values are obtained when the laser frequency is tuned to an air-like mode, approaching the naive estimate. Conversely, if the laser frequency is tuned to a diamond-like mode, the measured finesse will be consistently lower than expected.

We emphasize that our models thus far assume no losses, meaning the aforementioned finesse fluctuations arise entirely from interference effects. The finesse limitations can be understood by considering the effect of attaching a diamond membrane to the flat mirror. The dielectric coatings used for our mirrors are terminated with a high index material, and are optimized for use in air. Diamond has a high index of refraction ($n_d = 2.417$), which effectively lowers the reflectivity of the flat mirror, corresponding to a decrease in finesse for modes in which the electric field is more confined to the membrane. Quantitatively, the lossless 1D analytic model predicts that the finesse of

the diamond-like modes is reduced by a factor of $2/(n_d^2+1) \approx 0.3$. Conversely, if low-index-terminated mirrors were used, the diamond-like modes would exhibit the naive finesse while the air-like modes would have finesse reduced by $2/(1/n_d^2+1) \approx 0.6$.

A central prediction of this calculation is that the mode structure can cause dramatic finesse variations with laser wavelength. Moreover, because the mode structure shifts with t_d, peak finesse values should occur at different frequencies for different membrane thicknesses. Figure 6c shows the measured finesse $\mathcal{F}_L$ as a function of laser wavelength for three regions on the diamond membrane with marginally different thicknesses [3]. The square data points correspond to raw finesse data (binned using the Freedman-Diaconis rule to show the underlying distribution) where opacity illustrates measurement frequency. The mean finesse is plotted with a line. For each region, the peak finesse occurs at some wavelength corresponding to an air-like mode. The finesse decreases as the laser is tuned away from this wavelength, and the electric field becomes more localized in the diamond membrane.

While the qualitative features of our data in Fig. 6c are similar to the lossless model predictions, the drop in finesse is notably larger and steeper. For comparison, Fig. 6d shows the numerically simulated finesse for the ideal lossless system, which exhibits much more gradual variations. As discussed quantitatively below, the discrepancy can only be explained by including loss primarily at the air-diamond interface, such as scattering from roughness or contamination. The sharp wavelength dependence again arises from interferometric effects: when there is an electric field node at the air-diamond interface, field driven surface losses are strongly suppressed. In this geometry, a node appears at the air-diamond surface only for the air-like mode, providing a mechanism for the sharp finesse peaks in Fig. 6c.

To quantitatively understand the effects of loss, we add different absorption and scattering mechanisms to the numerical transfer matrix model described in Appendix 2.C. We consider loss in the mirrors, loss caused by scattering at the diamond interfaces, and absorption in the diamond. Loss inside the mirrors and diamond is modeled by adding complex components to the refractive indices of the layers. Scattering by sur-

3 White light spectra were taken at each membrane region, but the variation in thickness was below our measurement precision of $\sim$ 200 nanometers, illustrating that even slight changes in diamond thickness can drastically change the finesse measured for a given laser frequency.

face roughness of the diamond membrane is added by adjusting the interface reflection and transmission coefficients according to [30, 31]

$$r_{ij} = r_{ij}^{(0)} e^{-2(2\pi\sigma n_i/\lambda)^2} \tag{2.4}$$

$$t_{ij} = t_{ij}^{(0)} e^{-(1/2)\left(2\pi\sigma(n_i-n_j)/\lambda\right)^2}, \tag{2.5}$$

where r_{ij} (t_{ij}) is the amplitude reflection (transmission) coefficient going from material of index n_i into material of index n_j, σ is the rms surface roughness, λ is the wavelength in vacuum, and $r_{ij}^{(0)}$ and $t_{ij}^{(0)}$ are the lossless Fresnel coefficients. These reflection and transmission coefficients are used in the transfer matrix describing each diamond surface. To quantitatively compare the effects of each individual source of loss, we increase its strength sufficiently to bring the peak finesse $\mathcal{F}_L$ down to our observed value of $17,000$ (while holding other sources of loss at zero). We then calculate the cavity modes and linewidths for the cavity parameters extracted from the fit in Fig. 6a over the cavity lengths illustrated in Fig. 7a.

Figure 7b shows $\mathcal{F}_L$ as a function of wavelength, as predicted by several loss models. As noted earlier, scattering at the air-diamond interface behaves qualitatively differently from the other loss models, and most closely approaches the features we observe in Fig. 6c. Because there is always a node at the high-index-terminated mirror surface, scattering from the diamond-mirror interface does not produce such sharp features.

Figures 7b also includes simulations using our best estimate for the specific losses in our system. Enough mirror loss was added to bring the finesse down to $37,000$ (peak finesse measured for the bare cavity), and we set the diamond-mirror interface roughness to 0.19 nm-rms (as measured for similar samples). To match the features in Fig. 6c, we added sufficient scattering at the air-diamond interface to produce a peak in $\mathcal{F}_\mathcal{L}$ (see Fig. 7b) with a FWHM of 1.14 nm (the linewidth of the central peak in Fig. 6c). Finally, absorptive loss was added to bring the peak $\mathcal{F}_L$ value down to $17,000$. Notably, a very large air-diamond surface roughness ($\sigma = 3.5$ nm-rms) was required to reproduce the features of Fig. 6c. This roughness is far larger than values < 0.2 nm-rms measured on diamond samples etched by $ArCl_2$, and indicates some additional surface scattering or contamination is likely to blame.

After optical measurements were concluded, AFM measurements of the membrane revealed surface roughness of ~ 1 nm-rms in the regions of interest (measured over one

optical wavelength squared). The increased roughness was likely caused by the third $ArCl_2$ etch (while bonded to the mirror), which produced noticeable surface damage in some areas of the membrane (see Fig. 5c); the regions used in these experiments appeared unaffected, but in fact suffered roughening. Surface absorption caused by contamination could also be present, and would behave similarly in our model, exhibiting the same sensitivity to a field node at the air-diamond interface. It is therefore likely that reduced losses could be obtained with better surface preparation. Based on our simulations, state-of-the-art surface roughness $\sigma = 0.19$ nm-rms is compatible with finesse $> 10^6$ for air-like modes and $> 50,000$ for diamond-like modes.

2.4 Estimation of Purcell Enhancement

A figure of merit for cavity systems is the Purcell factor F_p, which describes the spontaneous emission enhancement into the cavity mode for an optimally placed single emitter. For a cavity with varying refractive index [32, 33],

$$F_p = \frac{3\,c\,\lambda^2}{4\pi^2\,n_d\,\Delta\nu}\frac{|E_{\max}|^2}{\iiint n^2(\mathbf{r})\,E^2(\mathbf{r})\,d\mathbf{r}^3}. \tag{2.6}$$

Here, $\Delta\nu$ is the cavity linewidth in frequency, λ is the resonant wavelength, $E(\mathbf{r})$ and $n(\mathbf{r})$ are the electric field and index of refraction within the cavity, and $E_{\max}$ is the electric field at the emitter in the diamond, assuming perfect emitter orientation and location. Notably, the Purcell factor depends on the linewidth in frequency, not length. As we are not currently able to directly measure the cavity spatial mode and $\Delta\nu$, we use our model and measurements of $\mathcal{F}_L$ to provide a theoretical estimate of the Purcell enhancement available in this cavity geometry.

In our analytic 1D model, it is straightforward to calculate the mode integrals of Eq. 2.6 and the linewidth $\Delta\nu$ in terms of the mirror finesse $\mathcal{F}$ (a function of only the lossless mirror reflectivity). This yields a simple result in the limit of large $\mathcal{F}$:

$$F_p^{(A)} = \mathcal{F}\frac{6\lambda^2}{n_d^3\pi^3 w_0^2} \tag{2.7}$$

$$F_p^{(D)} = \mathcal{F}\frac{12\lambda^2}{(n_d^3+n_d)\pi^3 w_0^2}, \tag{2.8}$$

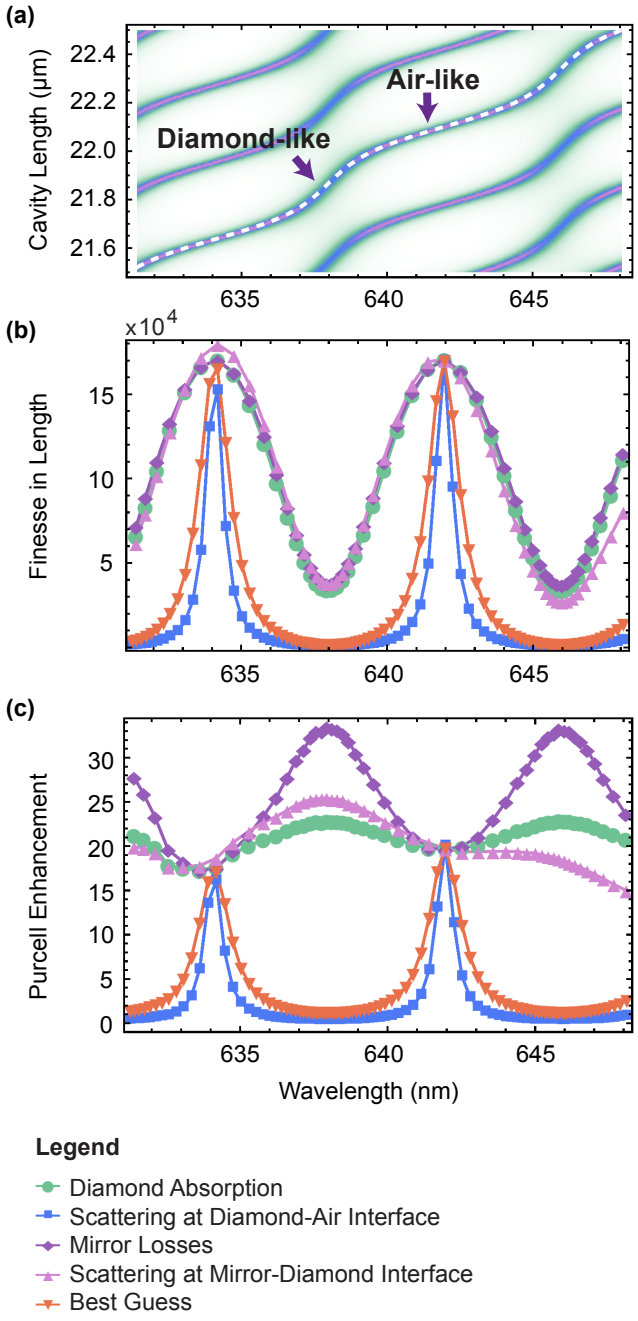

Figure 7: (Color online) Numerical cavity simulations including wavefront curvature and loss as a function of resonance wavelength. (a) Simulated cavity transmission, illustrating the cavity lengths for which the simulation was performed (dashed line). Steeper-sloped regions correspond to diamond-like modes, while shallower-slopes correspond to air-like modes.(b) Simulated finesse $\mathcal{F}_L$ for different sources of loss in the membrane-in-cavity system. For each simulation, enough loss was added to bring the measured finesse in length down to $17,000$. (c) Simulated Purcell enhancement for the same models as in (b). Note that the legend at bottom applies to both (b) and (c).

where $F_p^{(A)}$ ($F_p^{(D)}$) is the Purcell enhancement for air-like (diamond-like) modes and w_0 is the $1/e^2$ intensity radius of the cavity waist. Note that in the limit $n_d \to 1$, these match what one would obtain from the standard Purcell formula $(3\lambda^3/4\pi^2)(Q/V)$ with a mode volume of $V = (\pi/4)w_0^2 L$ [32] and $Q = 2L\mathcal{F}/\lambda$.

The two types of modes have different Purcell factors because they have different vacuum electric field maxima in the diamond and different cavity linewidths in frequency. The variation in $\Delta\nu$ has contributions from the reduced reflectivity of the flat mirror (due to the diamond layer) as well as the relative round-trip times of the diamond and air half-cavities.

Such effects are similar to finesse oscillations observed in optomechanical systems [29, 34]. Remarkably, in the high finesse limit of the lossless 1D model, the length dependence of the vacuum electric field maximum in diamond precisely cancels the length dependence of $\Delta\nu$, yielding the simple expressions above.

For lossless systems, $\mathcal{F}$ matches the peak value of $\mathcal{F}_L$, and one might be tempted to use Eqs. 2.7-2.8 with our observed peak finesse and cavity geometry to determine the Purcell enhancement of our device. Such a calculation (using $\mathcal{F} = 17,000$, w_0=2.2 μm, $\lambda = 637$ nm) would predict $F_p^{(A)} \approx 20$ and $F_p^{(D)} \approx 33$. However, adding in loss does not simply reduce $\mathcal{F}$: the location of the loss (in diamond or air) will affect the modes differently, and in general we find that using Eqs. 2.7-2.8 with $\mathcal{F} = \mathrm{Max}(\mathcal{F}_L)$ overestimates the best Purcell enhancement for realistic systems where loss is associated with the diamond.

Figure 7c shows the Purcell factor calculated using the numerical model with the different loss mechanisms described in the previous section. While mirror absorption produces similar results to the predictions of Eqs. 2.7-2.8, qualitatively distinct behavior appears from the surface losses that likely limit our system. In particular, we predict a maximum Purcell enhancement of approximately 20 for our current device geometry. However, our analysis also suggests that significant improvements can be obtained. For example, if surface losses can be limited to the observed roughness after $ArCl_2$ etching ($<$ 0.2 nm-rms), and higher reflectivity mirror coatings are used, a cavity finesse of 50,000 can be maintained even with an antinode at the air-diamond interface. Using a 30 μm radius-of-curvature mirror (attainable in our laser ablation setup), a $\langle 111 \rangle$-oriented 5 μm thick membrane, and a cavity length of 10 μm, a maximum Purcell factor of around 200 could be reached. Such a cavity would also couple efficiently to the fiber

mode ($>$ 90% with perfect alignment and low-loss mirrors [35]) and have a linewidth $\sim$300 MHz, which is large enough to accommodate minor spectral diffusion but small enough to resolve the excited-state structure of the NV center.

2.5 Finesse Changes with Cavity Length

Beyond the absorption and scattering processes considered above, a thick diamond membrane could also induce an additional, potentially important source of loss: mixing between transverse modes of the cavity. Our numerical model has assumed that the air-diamond interface follows the spherical wavefront of the cavity mode, allowing description of the cavity eigenstates in terms of two Gaussian beams in the diamond and air regions. The real planar interface, however, deviates from this requirement, and can thereby couple the TEM_{00} mode into higher-order Hermite-Gaussian modes. Because high-order transverse modes have a larger spatial extent, this mechanism could induce additional losses caused by clipping at the small fiber mirror. This type of loss would behave differently than those discussed previously because it would depend on the length of the cavity, with greater losses expected when higher-order modes approach degeneracy with the fundamental.

To estimate such losses, we apply non-degenerate perturbation theory (see Appendix 2.D) to calculate the first-order eigenstates of the membrane-in-cavity. The fraction of those eigenstates clipped at the fiber mirror can then be calculated to determine the loss per round trip. We begin with zero-order modes from the three-dimensional model discussed in Appendix 2.C. We then treat the volume of diamond between the curved, wavefront-matching surface and the true flat interface as the perturbative volume. The first order correction to the eigenstate is given by [36]:

$$\psi^1 = \kappa_{00} \sum_{m \neq 00} \frac{\iiint \psi_m(\mathbf{r}) \left(n_d^2 - 1\right) \phi_{00}(\mathbf{r}) \, d\mathbf{r}^3}{\kappa_m - \kappa_{00}} \psi_m \tag{2.9}$$

where the eigenstate is $\psi \approx \phi_{00} + \psi^1$, ϕ_{00} is a TEM_{00} zero-order cavity mode derived from our model, ψ_m is the m^{th} zero-order mode (including all longitudinal and transverse mode numbers), $\kappa_m = \left(\frac{\omega_m}{c}\right)^2$ contains the eigenfrequency ω_m for the m^{th} mode, and the integral is taken over the volume of the perturbation. The overlap integral cou-

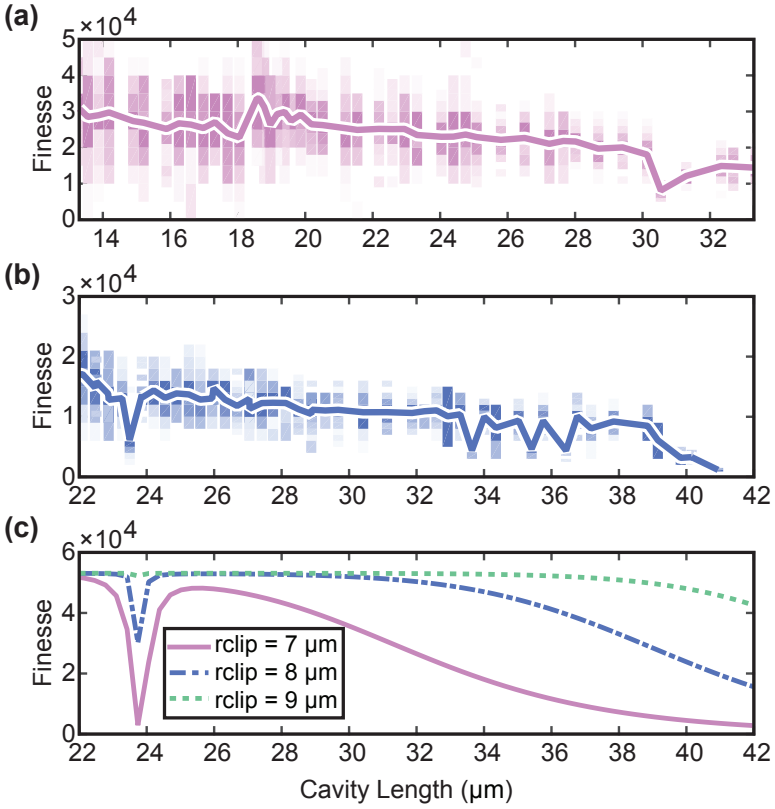

Figure 8: (Color online) (a) Finesse as a function of length measured for a bare cavity. In (a-b), binned raw finesse data is shown through opacity, while the mean finesse as a function of length is indicated by the solid line. (b) Finesse as a function of length measured for a cavity containing a 10.5 μm diamond membrane. The length axis is changed from (a) so that the beam radius on the fiber mirror takes on the same values over the range of collected data. (c) A simulation of finesse as a function of length including perturbative coupling to higher order modes evaluated for different mirror clipping radii.

ples only even order transverse modes, and falls off quickly with transverse mode number. In practice, we have included transverse mode numbers whose sum is ≤ 6. Because the denominator grows quickly as the mode frequencies diverge, we consider corrections only from the two longitudinal modes closest in frequency to ω_{00}.

To examine the importance of these perturbative couplings experimentally, we measured finesse as a function of cavity length with and without the membrane (see Fig. 8a-b). The bare cavity finesse exhibits a decreasing slope as a function of cavity length, which arises from coupling to lossy higher order modes caused by the Gaussian shape of the fiber dimple [37, 38]. We offset the x-axes of the bare cavity and membrane-in-

cavity so that the beam radii on the fiber mirror would match, varying from 2.5 μm to 3.6 μm over the length range presented in Fig. 8b-c. In addition to the decreasing slope seen for the bare cavity, we measured intermediate drops in finesse at specific cavity lengths. Since we use the same fiber mirror in both data sets, these dips must be associated with the membrane, and could be caused by coupling to lossy higher-order transverse modes. For comparison, we simulated the cavity finesse (ignoring all other loss processes) using the first order correction to the electric field wavefunction (Eq. 2.9) for different clipping radii on the fiber mirror, outside of which all light is assumed to scatter out of the cavity. The result is shown in Fig. 8c, which exhibits qualitatively similar drops in finesse at certain resonant lengths.

We lack the detailed surface profile data to accurately parameterize our membrane and fiber dimple topography, so the simulations cannot include the exact perturbations present in the measurement (for example, it likely also contains a wedge, which would couple TEM_{00} and TEM_{10} modes). Nevertheless, our calculations demonstrate that the finesse reductions observed at specific cavity lengths in Fig. 8b could reasonably be caused by this mechanism. Perhaps more importantly, this data illustrates that perturbative losses are not a major impediment to working with planar membranes, even at relatively large thicknesses > 10 μm and over a range of cavity lengths. Furthermore, as the diamond thickness diminishes, the perturbative coupling drops, indicating that it should be a negligible effect for few-micron-thick membranes.

2.6 Conclusion

We have shown that high finesse $\sim 17,000$ can be maintained in a Fabry-Perot microcavity even with incorporation of a thick diamond membrane. The membrane modifies the cavity modes, leading to variations in linewidth for different membrane thicknesses or different resonant frequencies. Our simulations indicate that surface losses dominate, producing qualitatively different behavior from bulk absorption. Membrane-induced coupling to higher-order transverse modes, conversely, does not greatly impact device performance. We anticipate that, despite the large surface losses, the current cavity will allow in the range of a 20-fold Purcell enhancement for diamond-based emitters,

which in the case of the NV center would direct more than a third of its emission into the zero phonon line. Furthermore, device performance in this case is limited by surface roughness or contamination that is well above the currently attainable limits [27, 28].

When cooled to cryogenic temperatures and locked to the NV resonance frequency, such devices could significantly enhance the efficiency of photon-mediated entanglement between distant defects [39]. Moreover, the cavity linewidth is below the typical spacing between spin-resolved resonant optical transitions in the NV center, enabling exploration of spin-dependent cavity effects. With improved diamond surface treatment and higher reflectivity mirrors, finesse $\sim 10^5$ should be possible [12], and shorter cavities with smaller radius-of-curvature mirrors could enhance the cavity cooperativity by another order of magnitude [17]; even with current fabrication capabilities, Purcell enhancements in the range of 200 appear within reach. Ultimately, this highly-tunable open-cavity geometry could offer a route towards an efficient or even deterministic interface between single photons and solid-state spins.

Acknowledgments

We acknowledge support from NSERC, FRQNT, Canadian Foundation for Innovation, Canada Research Chairs, and INTRIQ.

2.A Estimation of Bare Cavity Parameters

The following section describes a method for extracting some parameters of the bare fiber cavity system given measurable quantities and a one dimensional model shown in Fig. 9. These calculations permit us to understand the asymmetric lineshapes observed for both the bare and membrane-in-cavity systems.

In this model, the mirrors have real amplitude transmission and reflection coefficients t and r, and we account for a loss per round trip in the cavity of $1 - e^{-2\alpha} \approx 2\alpha$. Assuming that light is launched into the cavity through the fiber, E_{in} is the incident electric field, E^0_{ref} is the reflected field that is coupled back into the fiber core, E'_{ref} is the reflected field that is not coupled into the fiber core, and E_{trans} is the field coupled to the (free space) transmitted mode. The field circulating within the cavity is represented by E_{circ},

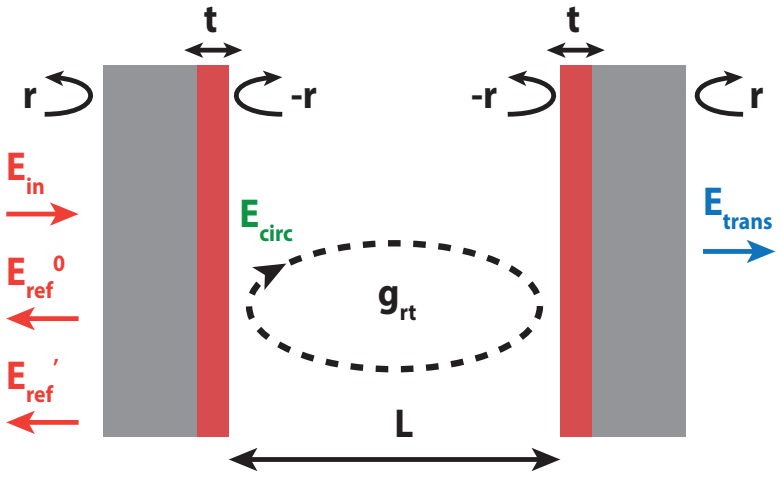

Figure 9: (Color online) The one-dimensional model used to estimate bare cavity parameters. L is the cavity length; r and t are the mirror amplitude reflection and transmission coefficients, g_{rt} is the round-trip gain of the cavity, and E_{in}, E^0_{ref}, E'_{ref}, E_{trans}, and E_{circ} are the electric fields at the input, reflected into the fiber, reflected into other modes, transmitted, and circulating in the cavity, respectively.

which is defined just to the right of the left-hand mirror; the change in amplitude and phase incurred in one roundtrip is represented by the rountrip gain: $g_{rt} = e^{-2\alpha}e^{-\frac{2iL\omega}{c}}$. We consider imperfect cavity coupling, where ϵ_1 is the overlap between the fiber and cavity modes, and ϵ_2 is the coupling coefficient between the cavity and transmitted modes (for our analysis we set $\epsilon_2 \approx 1$). If the ablation spot is not perfectly centered on the fiber core, the promptly reflected light that is coupled back into the fiber mode can be described by a complex coupling coefficient η, which has a magnitude less than unity as well as a nonzero phase for imperfect alignment. The relevant relationships between these parameters are given by:

$$E^0_{\text{ref}} = -e^{-2\alpha-\frac{2iL\omega}{c}} rt\epsilon_1 E_{circ} + r\eta E_{in} \tag{2.10}$$

$$E_{\text{circ}} = e^{-2\alpha-\frac{2iL\omega}{c}} r^2 E_{circ} + t\epsilon_1 E_{in} \tag{2.11}$$

$$E_{\text{trans}} = e^{-\alpha-\frac{iL\omega}{c}} t\epsilon_2 E_{circ} \tag{2.12}$$

Solving for the transmitted and reflected powers ($|E_{trans}|^2$ and $|E^0_{ref}|^2$), normalized to the input power ($|E_{in}|^2$) yields the power reflected (P_r) and transmitted (P_t):

$$P_r = \frac{r^2\left|\left(t^2\,\epsilon_1^2 + \left(-e^{2\alpha+\frac{2iL\omega}{c}} + r^2\right)\eta\right)\right|^2}{e^{4\alpha} + r^4 - 2\,e^{2\alpha}\,r^2\cos\left[\frac{2L\omega}{c}\right]} \tag{2.13}$$

$$P_t = \frac{e^{2\alpha}\,t^4\,\epsilon_1^2\epsilon_2^2}{e^{4\alpha} + r^4 - 2\,e^{2\alpha}\,r^2\cos\left[\frac{2L\omega}{c}\right]}. \tag{2.14}$$

We set $\eta = a + ib$ and expand the cosine terms to second order in ΔL, where $L = m\lambda/2 + \Delta L$ and m is an integer, resulting in power lineshapes of the form:

$$P_r = \frac{(a_1 + a_2\,\Delta L)}{\pi}\frac{\left(\frac{\delta L}{2}\right)^2}{\left(\frac{\delta L}{2}\right)^2 + \Delta L^2} + y_0 \tag{2.15}$$

$$P_t = \frac{a_3}{\pi}\frac{\left(\frac{\delta L}{2}\right)^2}{\left(\frac{\delta L}{2}\right)^2 + \Delta L^2} \tag{2.16}$$

where δL is the FWHM cavity linewidth measured in length, and:

$$y_0 = \left(a^2 + b^2\right)r^2 + a t^2\epsilon_1^2 \tag{2.17}$$

$$a1 = \pi t^2\epsilon_1^2\frac{a\left(r^4 - e^{4\alpha}\right) + r^2t^2\epsilon_1^2}{\left(e^{2\alpha} - r^2\right)^2} \tag{2.18}$$

$$a2 = \frac{4\pi b\,e^{2\alpha}\,r^2t^2\epsilon_1^2\omega}{c\left(e^{2\alpha} - r^2\right)^2} \tag{2.19}$$

$$a3 = \pi\frac{e^{2\alpha}\,t^4\epsilon_1^2\epsilon_2^2}{\left(e^{2\alpha} - r^2\right)^2} \tag{2.20}$$

Note that this produces a Fano lineshape in reflection. The parameters $\{y_0, a_1, a_2, a_3\}$ can be extracted from our data by fitting the transmission and reflection curves and

calibrating the input power. In addition, we use measurements of the finesse $\mathcal{F}$ and the following relationships to fully constrain the cavity parameters:

$$\mathcal{F} = \frac{\pi}{\alpha + t^2} \tag{2.21}$$

$$t^2 + r^2 + \alpha = 1, \tag{2.22}$$

as well as the known laser frequency ω and $\epsilon_2 = 1$. With these expressions, one can solve for all of the cavity parameters of interest. For example, using data acquired in a bare cavity of length 12.2 ± 0.3 μm we obtain:

$$\begin{aligned} t &= (8.8 \pm 0.2) * 10^{-3} \\ r &= -0.999957 \pm 0.000001 \\ a &= 0.61 \pm 0.02 \\ b &= 0.14 \pm 0.04 \\ \epsilon_1 &= 0.69 \pm 0.03 \\ \alpha &= 8 \pm 1 \text{ ppm} \end{aligned}$$

This yields a power transmittance of $T = 78 \pm 3$ ppm, which agrees with the quoted coating value of $T = 70 \pm 10$ ppm. The combined absorption and scattering losses were quoted to be < 24 ppm, which also agrees with the derived α value.

Note: While in the final stages of preparing this manuscript, we became aware of detailed theoretical and experimental exploration of the origin of asymmetric lineshapes associated with misalignment of fiber cavities [40].

2.B Calculating the Effective Radius of Curvature

The Gaussian-shaped ablation dimple can be approximated by a parabola near the center, which has a well defined radius of curvature. This radius is appropriate for cavity modes with small beam diameters on the mirror. As the cavity length is increased, the mode diameter grows and the approximation breaks down. In this regime, it is more accurate to estimate the effective mirror radius from the spacing of the higher order TEM modes.

If $\Delta\nu_{trans}$ is the difference in frequency between adjacent transverse modes with the same longitudinal mode (e.g. $\mathrm{TEM}_{m,n}$ and $\mathrm{TEM}_{m,n+1}$), the effective radius of curvature is

$$R = L\left(1 - \cos^2\left(\frac{\Delta\nu_{trans}}{\nu_{FSR}}\pi\right)\right)^{-1}, \tag{2.23}$$

where L is the length of the cavity and $\nu_{FSR} = c/2L$ is the free spectral range. Using this equation to analyze the TEM_{00} and $\mathrm{TEM}_{01}/\mathrm{TEM}_{10}$ modes in the white-light spectrum measured for the bare cavity, we estimate an effective radius of curvature of 61.0 ± 1.4 μm for a bare cavity length of 13.3 μm and a beam radius of 2.6 μm on the fiber mirror. The same beam diameter would correspond to a cavity length of 22 μm for a cavity containing a 10.5 μm diamond membrane, as the beam diverges less in the higher refractive index medium. Deviation from the radius of curvature extracted from a parabolic fit to our interferometry measurement ($R \approx 50 \pm 1$ μm) arises because the finite diameter mode samples a range of curvatures within the Gaussian dimple.

2.C Numerical Cavity Model

We have developed a numerical model to calculate the fundamental Gaussian cavity mode for a half symmetric cavity containing a diamond membrane bonded to the flat mirror. The model first solves for the Gaussian beam parameters (waist radius and position) in both the air and diamond sections assuming a curved diamond surface lying along the mode wavefront (see Fig. 10). As boundary conditions, we require that the beam diameters and radii of curvature are equal at the air-diamond interface to ensure electric field continuity. In addition, the radius of curvature in air should match the ablation radius of curvature at the fiber mirror, while the mode waist in diamond should lie at the flat mirror. With these four requirements, once can solve for the required radius of curvature for the air-diamond interface, the beam waists w_1 and w_2 corresponding to the modes in diamond and air, and the effective waist position x_{02} for the air mode.

Once the two Gaussian modes in the air and diamond regions are known, one can solve for the resonant frequencies and lengths of the cavity using transfer matrix the-

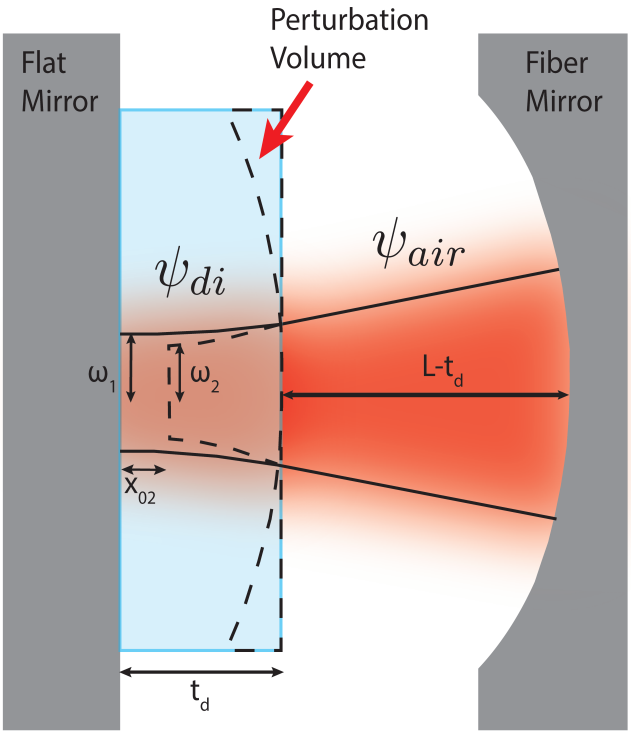

Figure 10: (Color online) A diagram illustrating the $1/e^2$ intensity radius of the zero-order Gaussian modes in the diamond and air (solid lines). The mode in diamond has a waist with radius w_1 at the flat mirror, while the mode in air has a waist with radius w_2 a distance x_{02} from the mirror flat. The perturbation volume considered in Eq. 2.9 (dashed lines) is the difference between the presumed diamond interface lying along the mode wavefront and the planar diamond surface.

ory applied to the left and right traveling electric fields within the cavity structure (see Fig. 11).

Here, we model the full geometry of the flat mirror as a one-dimensional 29 layer dielectric stack where the right-moving electric field travels from glass into air; the transfer matrix describing this process is M_{gma}. Conversely, the fiber mirror is modeled as the inverse matrix ($M_{amg} = M_{gma}^{-1}$). Since the mirrors are defined for air termination, we need to include an additional matrix to model the air-diamond interface at the flat mirror (D_{ad}). As mentioned above, we assume that the second air-diamond interface

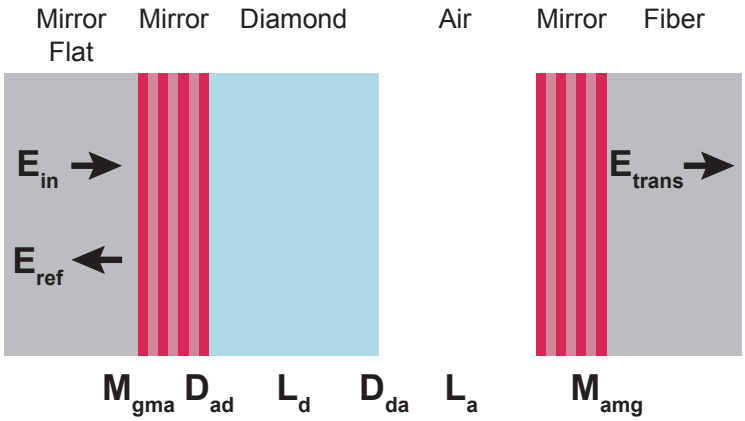

Figure 11: (Color online) A diagram indicating the relevant transfer matrices used to calculate the resonant cavity frequencies and lengths.

(D_{da}) follows the curvature of the wavefronts at that position (dashed line in Fig. 10). The propagation matrices in the air and diamond include Guoy phase, and are given by:

$$L_{diamond} = \begin{bmatrix} e^{-\frac{2\pi n_d}{\lambda} t_d + i\phi_1(t_d)} & 0 \\ 0 & e^{\frac{2\pi n_d}{\lambda} t_d - i\phi_1(t_d)} \end{bmatrix}$$

$$L_{air} = \begin{bmatrix} e^{-\frac{2\pi}{\lambda}(L-t_d) + i\phi_2(L-x_{02})} & 0 \\ 0 & e^{\frac{2\pi}{\lambda}(L-t_d) - i\phi_2(L-x_{02})} \end{bmatrix}$$

where $\phi_i(x) = \arctan\left(x\lambda/\pi w_i^2\right)$ is the Guoy phase, t_d is the diamond thickness, L is the cavity length, w_1 and w_2 are the $1/e^2$ radii at the diamond and air waists respectively, and x_{02} is the effective beam waist position for the mode in air (see Fig. 10). The full transfer matrix for the cavity is:

$$\begin{bmatrix} E_{trans} \\ 0 \end{bmatrix} = S \begin{bmatrix} E_{in} \\ E_{ref} \end{bmatrix} \tag{2.24}$$

where:

$$S = M_{amg}\, L_a\, D_{da}\, L_d\, D_{ad}\, M_{gma}. \tag{2.25}$$

Using the transmission curves calculated with this model, the linewidth in frequency and length can be determined. The field within the diamond and air regions can be found by evaluating subsets of the transfer matrices to find the amplitudes in the air and diamond, which are then multiplied by appropriate Gaussian modes.

When adding loss to this model, the dielectric indices used in the mirror stack and diamond were given small complex components; in addition the interface matrices D_{da} and D_{ad} were modified according to Eqs. 2.4-2.5.

2.D Nondegenerate Perturbation Theory

The Hermite-Gaussian family of modes represent the eigenstates of a spherical resonator, satisfying the Helmholtz equation [41]. Introducing some small volume of material with a different refractive index can break the cavity symmetry, leading to a new set of cavity eigenstates that can be expressed as a linear combination of the unperturbed cavity modes [36].

In our case, the zero-order modes correspond to solutions in the presence of a membrane whose interface is curved to follow a wavefront (see Fig. 10). They are defined by

$$\left(\nabla^2 + \kappa_i n_0^2(\mathbf{r})\right) \psi_i^0(\mathbf{r}) = 0, \tag{2.26}$$

where ψ_i^0 are the zero-order modes of the system, $\kappa_i = (\frac{\omega_i}{c})^2$ contains the corresponding eigenfrequencies ω_i, and $n_0^2(\mathbf{r})$ is the index of refraction inside the cavity assuming an air-diamond interface following the mode wavefront. These zero-order eigenfunctions may be found exactly as a (real-valued) Hermite-Gaussian family of modes with different parameters in the air and diamond regions (see Appendix 2.C). The orthonormalization condition is

$$\iiint \psi_m^0(\mathbf{r}) n_0^2(\mathbf{r}) \psi_n^0(\mathbf{r}) d^3\mathbf{r} = \delta_{mn}, \tag{2.27}$$

where δ_{mn} is the Kronecker delta, the integral is taken over the cavity volume, and subscripts m and n encode all transverse and longitudinal mode indices.

We wish to calculate the perturbative effect of the membrane planarity, which is equivalent to introducing a small piece of dieletric representing the difference between

the curved surface and a flat one. We are interested in a fundamental transverse mode (which is non-degenerate), for which the exact eigenstate ψ satisfies

$$\left(\nabla^2 + \kappa\left(n_0^2(\mathbf{r}) + \lambda\mathcal{V}(\mathbf{r})\right)\right)\psi = 0, \tag{2.28}$$

where $\mathcal{V}(\mathbf{r}) = n_d^2 - 1$ inside the perturbation volume (and zero outside), λ is some small number, and κ corresponds to the new eigenfrequency. We can express both ψ and κ as a power series in λ:

$$\psi = \psi_0^0 + \sum_{n=1}^{\infty} \lambda^n \psi^n \tag{2.29}$$

$$\kappa = \kappa_0 + \sum_{n=1}^{\infty} \lambda^n \Delta_n \tag{2.30}$$

where ψ_0^0 and κ_0 correspond to the non-degenerate fundamental mode eigenstate of the unperturbed system, and ψ^n, Δ_n are the n^{th} order corrections. Considering only the terms of Eq. 2.28 to order λ, one finds

$$(\nabla^2 + n_0^2(\mathbf{r})\kappa_0)\psi^1 = -(\Delta_1 n_0^2(\mathbf{r}) + \kappa_0\mathcal{V}(\mathbf{r}))\psi_0^0, \tag{2.31}$$

and one can thereby derive the first order correction to the eigenstate:

$$\psi^1 = \kappa_0 \sum_{m\neq 0} \frac{\iiint \psi_m^0(\mathbf{r})\,\mathcal{V}(\mathbf{r})\,\psi_0^0(\mathbf{r})\,d\mathbf{r}^3}{\kappa_m - \kappa_0}\,\psi_m^0 \tag{2.32}$$

where ψ_m^0 is the mth order mode of the unperturbed system, and we have set $\lambda = 1$. Here m labels all longitudinal and transverse modes to which the zero-order Gaussian mode ψ_0^0 can be coupled by the perturbation.

References

1. Lončar, M. & Faraon, A. Quantum photonic networks in diamond. *MRS Bulletin* **38,** 144 (2013).
2. Aharonovich, I. & Neu, E. Diamond nanophotonics. *Advanced Optical Materials* **2,** 911 (2014).
3. Schirhagl, R., Chang, K., Loretz, M. & Degen, C. L. Nitrogen-vacancy centers in diamond: nanoscale sensors for physics and biology. *Annual Review of Physical Chemistry* **65,** 83 (2014).
4. Rondin, L., Tetienne, J., Hingant, T., Roch, J., Maletinsky, P. & Jacques, V. Magnetometry with nitrogen-vacancy defects in diamond. *Reports on Progress in Physics* **77,** 056503 (2014).
5. Ladd, T. D., Jelezko, F., Laflamme, R., Nakamura, Y., Monroe, C. & O'Brien, J. L. Quantum computers. *Nature* **464,** 45 (2010).
6. Nemoto, K., Trupke, M., Devitt, S. J., Stephens, A. M., Scharfenberger, B., Buczak, K., Nöbauer, T., Everitt, M. S., Schmiedmayer, J. & Munro, W. J. Photonic architecture for scalable quantum information processing in diamond. *Physical Review X* **4,** 031022 (2014).
7. Doherty, M. W., Manson, N. B., Delaney, P., Jelezko, F., Wrachtrup, J. & Hollenberg, L. C. The nitrogen-vacancy colour centre in diamond. *Physics Reports* **528,** 1 (2013).
8. Burek, M. J., Chu, Y., Liddy, M. S., Patel, P., Rochman, J., Meesala, S., Hong, W., Quan, Q., Lukin, M. D. & Lončar, M. High quality-factor optical nanocavities in bulk single-crystal diamond. *Nature Communications* **5,** 5718 (2014).
9. Khanaliloo, B., Mitchell, M., Hryciw, A. C. & Barclay, P. E. High-Q/V monolithic diamond microdisks fabricated with quasi-isotropic etching. *Nano Letters* **15,** 5131 (2015).
10. Lee, J. C., Bracher, D. O., Cui, S., Ohno, K., McLellan, C. A., Zhang, X., Andrich, P., Alemán, B., Russell, K. J., Magyar, A. P., *et al.* Deterministic coupling of delta-doped nitrogen vacancy centers to a nanobeam photonic crystal cavity. *Applied Physics Letters* **105,** 261101 (2014).

11. Faraon, A., Santori, C., Huang, Z., Acosta, V. M. & Beausoleil, R. G. Coupling of nitrogen-vacancy centers to photonic crystal cavities in monocrystalline diamond. *Physical Review Letters* **109,** 033604 (2012).

12. Hunger, D., Steinmetz, T., Colombe, Y., Deutsch, C., Hänsch, T. W. & Reichel, J. A fiber Fabry–Perot cavity with high finesse. *New Journal of Physics* **12,** 065038 (2010).

13. Muller, A., Flagg, E. B., Lawall, J. R. & Solomon, G. S. Ultrahigh-finesse, low-mode-volume Fabry-Perot microcavity. *Optics Letters* **35,** 2293 (2010).

14. Kaupp, H., Deutsch, C., Chang, H.-C., Reichel, J., Hänsch, T. W. & Hunger, D. Scaling laws of the cavity enhancement for nitrogen-vacancy centers in diamond. *Physical Review A* **88,** 053812 (2013).

15. Albrecht, R., Bommer, A., Deutsch, C., Reichel, J. & Becher, C. Coupling of a single nitrogen-vacancy center in diamond to a fiber-based microcavity. *Physical Review Letters* **110,** 243602 (2013).

16. Albrecht, R., Bommer, A., Pauly, C., Mücklich, F., Schell, A. W., Engel, P., Schröder, T., Benson, O., Reichel, J. & Becher, C. Narrow-band single photon emission at room temperature based on a single nitrogen-vacancy center coupled to an all-fiber-cavity. *Applied Physics Letters* **105,** 073113 (2014).

17. Johnson, S., Dolan, P., Grange, T., Trichet, A., Hornecker, G., Chen, Y.-C., Weng, L., Hughes, G., Watt, A., Auffèves, A., *et al.* Tunable cavity coupling of the zero phonon line of a nitrogen-vacancy defect in diamond. *New Journal of Physics* **17,** 122003 (2015).

18. Santori, C., Barclay, P., Fu, K. C., Beausoleil, R., Spillane, S. & Fisch, M. Nanophotonics for quantum optics using nitrogen-vacancy centers in diamond. *Nanotechnology* **21,** 274008 (2010).

19. Tamarat, P., Gaebel, T., Rabeau, J., Khan, M., Greentree, A., Wilson, H., Hollenberg, L., Prawer, S., Hemmer, P., Jelezko, F., *et al.* Stark shift control of single optical centers in diamond. *Physical Review Letters* **97,** 083002 (2006).

20. Chu, Y., de Leon, N. P., Shields, B. J., Hausmann, B., Evans, R., Togan, E., Burek, M. J., Markham, M., Stacey, A., Zibrov, A. S., *et al.* Coherent optical transitions in implanted nitrogen vacancy centers. *Nano Letters* **14,** 1982 (2014).

21. Mouradian, S. L., Schröder, T., Poitras, C. B., Li, L., Goldstein, J., Chen, E. H., Walsh, M., Cardenas, J., Markham, M. L., Twitchen, D. J., *et al.* Scalable integration of long-lived quantum memories into a photonic circuit. *Physical Review X* **5,** 031009 (2015).

22. Miguel-Sánchez, J., Reinhard, A., Togan, E., Volz, T., Imamoglu, A., Besga, B., Reichel, J. & Estève, J. Cavity quantum electrodynamics with charge-controlled quantum dots coupled to a fiber Fabry-Perot cavity. *New Journal of Physics* **15,** 045002 (2013).

23. Toninelli, C., Delley, Y., Stöferle, T., Renn, A., Götzinger, S. & Sandoghdar, V. A scanning microcavity for in situ control of single-molecule emission. *Applied Physics Letters* **97,** 021107 (2010).

24. Hunger, D., Deutsch, C., Barbour, R. J., Warburton, R. J. & Reichel, J. Laser microfabrication of concave, low-roughness features in silica. *AIP Advances* **2,** 012119 (2012).

25. Brandstätter, B., McClung, A., Schüppert, K., Casabone, B., Friebe, K., Stute, A., Schmidt, P. O., Deutsch, C., Reichel, J., Blatt, R., *et al.* Integrated fiber-mirror ion trap for strong ion-cavity coupling. *Review of Scientific Instruments* **84,** 123104 (2013).

26. Hausmann, B. J. M. *et al.* Integrated Diamond Networks for Quantum Nanophotonics. *Nano Letters* **12,** 1578 (2012).

27. Tao, Y. & Degen, C. Facile Fabrication of Single-Crystal-Diamond Nanostructures with Ultrahigh Aspect Ratio. *Advanced Materials* **25,** 3962 (2013).

28. Ovartchaiyapong, P., Pascal, L., Myers, B., Lauria, P. & Bleszynski Jayich, A. High quality factor single-crystal diamond mechanical resonators. *Applied Physics Letters* **101,** 163505 (2012).

29. Jayich, A. M., Sankey, J. C., Zwickl, B. M., Yang, C., Thompson, J. D., Girvin, S. M., Clerk, A. A., Marquardt, F. & Harris, J. G. E. Dispersive optomechanics: a membrane inside a cavity. *New Journal of Physics* **10,** 095008 (2008).

30. Szczyrbowski, J. & Czapla, A. Optical absorption in DC sputtered InAs films. *Thin Solid Films* **46,** 127 (1977).

31. Katsidis, C. C. & Siapkas, D. I. General transfer-matrix method for optical multilayer systems with coherent, partially coherent, and incoherent interference. *Applied Optics* **41,** 3978 (2002).

32. Gerard, J.-M. in *Single Quantum Dots* 269 (Springer, 2003).

33. Sauvan, C., Hugonin, J.-P., Maksymov, I. & Lalanne, P. Theory of the spontaneous optical emission of nanosize photonic and plasmon resonators. *Physical Review Letters* **110,** 237401 (2013).

34. Wilson, D. J., Regal, C. A., Papp, S. B. & Kimble, H. J. Cavity optomechanics with stoichiometric SiN films. *Physical Review Letters* **103,** 207204 (2009).

35. Joyce, W. & DeLoach, B. Alignment of Gaussian beams. *Applied Optics* **23,** 4187 (1984).

36. Favero, I., Sankey, J. & Weig, E. in *Cavity Optomechanics* 83 (Springer, 2014).

37. Benedikter, J., Hümmer, T., Mader, M., Schlederer, B., Reichel, J., Hänsch, T. W. & Hunger, D. Transverse-mode coupling and diffraction loss in tunable Fabry–Pérot microcavities. *New Journal of Physics* **17,** 053051 (2015).

38. Kleckner, D., Irvine, W. T., Oemrawsingh, S. S. & Bouwmeester, D. Diffraction-limited high-finesse optical cavities. *Physical Review A* **81,** 043814 (2010).

39. Bernien, H. *et al.* Heralded entanglement between solid-state qubits separated by three metres. *Nature* **497,** 86 (2013).

40. Gallego, J., Ghosh, S., Alavi, S. K., Alt, W., Martinez-Dorantes, M., Meschede, D. & Ratschbacher, L. High-finesse fiber Fabry–Perot cavities: stabilization and mode matching analysis. *Applied Physics B* **122,** 47 (2016).

41. Saleh, B. E. & Teich, M. C. *Fundamentals of Photonics* (Wiley New York, 1991).

Preface to Chapter 3

In the second manuscript, we measure room temperature coupling between a fiber cavity and a single germanium vacancy center in a diamond membrane. These defects could provide the basis for an efficient spin-photon interface since they exhibit a high branching ratio into the ZPL, which can have nearly transform-limited linewidths at low temperature. We measure an increased fluorescence spectral density in cavity emission at room temperature, from which we predict a strong Purcell enhancement at cryogenic temperatures. The upshot of this work is that both the emitter and cavity are of sufficient quality to dramatically increase the fraction and rate of coherent photon emission compared to existing platforms using defects in diamond.

3

Cavity-Enhanced Photon Emission from a Single Germanium Vacancy Center in a Diamond Membrane

Rasmus Høy Jensen[1,*], Erika Janitz[2,*], Yannik Fontana[2], Yi He[3], Olivier Gobron[1], Ilya Radko[1], César Daniel Rodríguez Rosenblueth[2], Lilian Childress[2], Alexander Huck[1], Ulrik Lund Andersen[1]

[*] These authors contributed equally to this work

1. Center for Macroscopic Quantum States (bigQ), Department of Physics, Technical University of Denmark, Lyngby Denmark
2. Department of Physics, McGill University, Montreal Canada
3. Department of Electrical and Computer Engineering, Carnegie Mellon University, Pittsburgh USA

This manuscript is in preparation and will be submitted to Physical Review Letters.

Abstract

Atomic-like defects in diamond provide a promising light-matter interface for quantum information applications. Looking at alternatives to the well-studied nitrogen-vacancy (NV) center, we examine interactions between a defect with superior optical properties, the germanium vacancy (GeV), and an open microcavity. We demonstrate room temperature coupling between a single emitter in a diamond membrane and a finesse $11,000$ fiber cavity, evidenced by a 8-fold increase in the spectral density of emission. The experimental advancements in this work set the stage for future cryogenic experiments, where for the existing system we estimate a factor of 7 increase in the GeV spontaneous emission rate.

Defect centers in diamond can exhibit long-lived spin states that are accessible via coherent optical transitions [1–3], providing a promising platform for quantum information applications [4, 5]. There have been impressive steps towards creating such a platform using the NV center in diamond, with several critical elements demonstrated in the last decade [6–12]. Nevertheless, optically-mediated entanglement rates for NVs have been limited to tens of Hz [13] due to the low fraction of photons emitted into the coherent zero phonon line (ZPL) (3%), the difficulty of collecting these photons into a single optical mode, the long excited state lifetime (12 ns), and spectral diffusion of the emitter. This platform could be improved by coupling defects to an optical resonator, thereby increasing the ZPL emission rate into a well-defined mode. However, enhanced spectral diffusion near surfaces has thus far impeded attempts to realize stable NV centers in small-mode-volume optical cavities [14–16].

An alternative approach explores emitters such as the silicon vacancy (SiV) [17, 18] and GeV centers [19, 20]. While their spins interact strongly with phonons (requiring low temperature [3] or high strain [21]), their optical properties are superior. Owing to inversion symmetry, these defects have large ZPL fractions ($60 - 70\%$) and exhibit minimal spectral diffusion, even near fabricated surfaces [22, 23]. Moreover, there are indications that the GeV also has high quantum efficiency [23]. Integrating GeV centers into optical resonators is therefore a promising step toward generating highly efficient or even deterministic interactions between spins and photons [24].

Over the last decade, two primary approaches to coupling diamond defect centers to optical cavities have emerged: (1) diamond nanophotonics and (2) open-geometry microcavities. Emitters coupled to low-mode-volume nanophotonic resonators can exhibit high Purcell enhancement [14] and can even enter the high-cooperativity regime [24, 25], but suffer from enhanced spectral diffusion and inhomogeneous broadening due to nearby diamond surfaces. Open Fabry-Pérot microcavities offer much narrower resonator linewidths as well as in-situ spectral and spatial tunability. Critically, such cavities accommodate microns-thick diamond membranes where even NV centers exhibit minimal spectral diffusion [26]. So far it has proved challenging to fabricate membranes with sufficiently low-loss surfaces as to take advantage of very high cavity finesse. This is particularly true when the energy of the optical mode is concentrated in

the diamond (so-called "diamond-like" modes) since the electric field has an antinode at the air-diamond interface [27]. Indeed, the only demonstration of coupling between an emitter in a diamond membrane and an open cavity used a finesse $\mathcal{F} = 5260$ mode localized in air. Nevertheless, this system achieved a 30-fold enhancement in NV center ZPL emission, clearly illustrating the potential of the open-cavity approach.

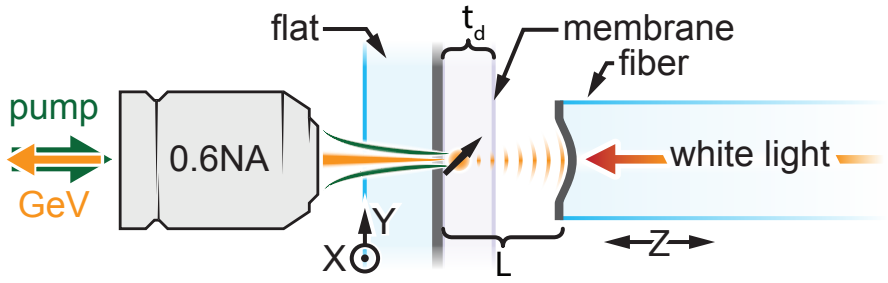

Figure 12: A schematic of the cavity setup.

In this work, we observe coupling between a single GeV center in a diamond membrane and a Fabry-Pérot microcavity at room temperature, thereby combining the advantageous optical properties of the GeV with the flexibility of an open-geometry resonator. We build on previous room temperature experiments with defects in nanodiamonds [28, 29] to observe clear funneling of GeV center emission into the cavity mode, evidenced by an 8-fold increase in the spectral density of single photon emission [30]. Our experiment represents the first demonstration of GeV-cavity coupling and confirms that both the diamond membrane and cavity are of sufficient quality to support high finesse ($\mathcal{F} > 10,000$) "diamond-like" resonances. Furthermore, we observe and study the presence of a dark state in the GeV level structure, ellucidating new details regarding the emission dynamics. Looking toward future cryogenic experiments, we predict a Purcell enhancement of the ZPL of ≈ 10 with our current device, which would lead to a ≈ 7-times reduction in the excited state lifetime. These results therefore represent an important step toward realizing an efficient spin-photon interface using diamond defects in open-cavities.

Our microcavities comprise a macroscopic flat mirror (substrate from Coastline optics) and a microscopic spherical mirror deposited on the tip of a single-mode optical fiber (Thorlabs 630HP). The spherical dimple of the fiber mirror is machined using a laser ablation technique [31]. Both the flat and fiber substrates are coated with dielec-

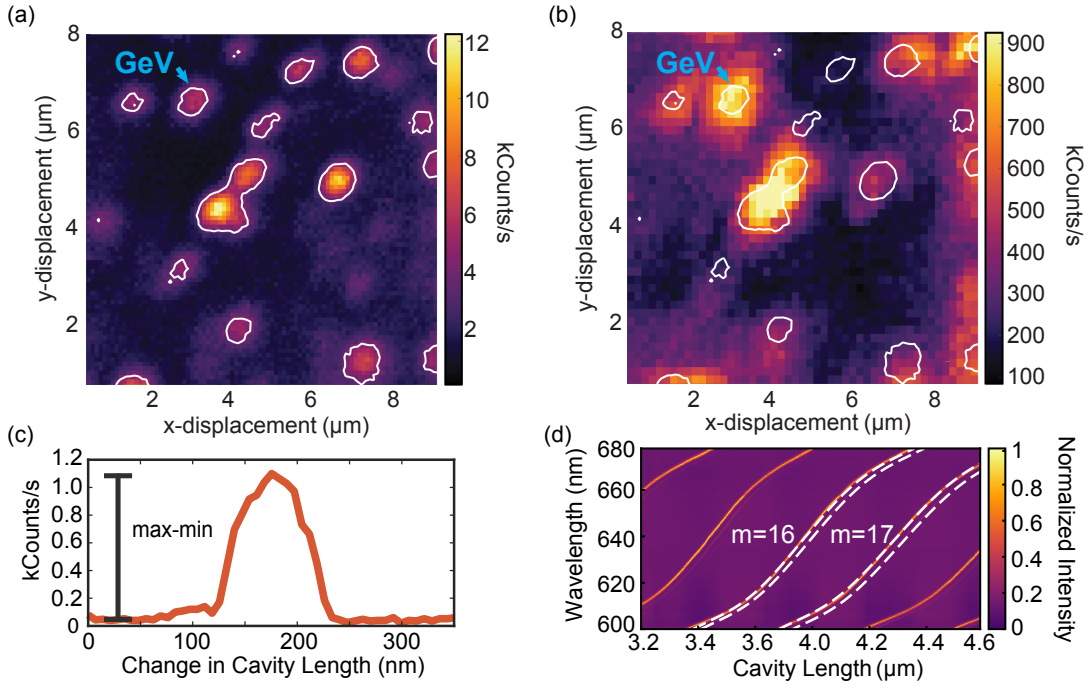

Figure 13: a) A confocal image of the membrane, where white contours indicate emitter localization. The studied GeV center is indicated with an arrow. b) A 3D cavity scan over the same area, with the confocal contours overlaid and the same defect indicated. c) An example length scan taken at the position of the studied GeV center. The difference between the maximum and minimum photon counts is labeled, and is used in generating the 3D cavity scan shown in b). d) White light cavity transmission as a function of length. The dashed lines correspond to numerical fits of the fundamental and first order transverse modes of the $m = 16$ and 17 longitudinal modes.

tric Bragg stack mirrors (LASEROPTIK) with alternating high and low index layers of Ta_2O_5 and SiO_2, respectively. The flat mirror is low-index terminated such that the addition of the diamond membrane increases the mirror reflectivity; it also produces an electric field antinode at the mirror-diamond interface. In contrast, the fiber mirror is high-index terminated (designed for use in air) and has an electric field node at the air-mirror interface. The layer designs are numerically optimized to have (into diamond and air respectively) matched transmissions of $T_{flat} = T_{fiber} = 70$ ppm at 602 nm. At the pump wavelength (532 nm) the mirrors have $T_{flat} = 99.8\%$ and $T_{fiber} = 0.7\%$ to prevent laser leakage into the fiber.

We incorporate an emitter into the cavity by bonding a diamond membrane containing GeV centers (fabrication details in supplementary) to the flat mirror, which is

mounted on a three-axis stage with piezoelectric control (Fig. 12). A coverslip corrected objective for emitter excitation and cavity mode collection is mounted facing the backside of the flat mirror (Olympus LUCPLFLN 40X, 0.6 NA), and a separate stage facing the sample is used for mounting either an objective (Mitutoyo 100X Plan Apo, 0.7 NA) for confocal characterization, or the fiber mirror for cavity characterization. An additional tip-tilt stage is used to align the fiber mirror normal to the sample, with a piezoelectric scanner along the z-axis for fine tuning the cavity length. We align the collection objective and fiber mirror to the excitation laser, and scan the sample relative to this to study different emitters.

We first characterize the membrane in the confocal configuration to map out the position of emitters in the scanning range of the sample stage. Confocal images are obtained by exciting emitters with a 532 nm laser (19 mW) through the back of the flat mirror, and collecting emission through the collection objective. We filter the emission with a passband of $600 - 605$ nm and an additional 532 nm notch filter (Semrock) before coupling the emission into a single mode fiber, resulting in the image shown in Fig. 24a. Here, bright spots correspond to single GeV emitters (confirmed by $g^{(2)}$ measurements, see supplementary), and contours are drawn at 4000 counts/s to qualitatively show emitter localization. The relatively low count rate achieved can be attributed to a combination of low transmission in the collection path, narrow spectral filtering, and much of the emission being confined to the membrane in the form of guided modes. Count rates are further reduced by the presence of a dark state in the GeV center energy level structure. We studied the population dynamics of one emitter by measuring $g^{(2)}$ as a function of power and found that it was well described by a three-level model including power-dependent ionization (full details in supplementary). We found a dark-state equilibrium population of over 90% at high pump power, drastically reducing the emitter brightness. It is possible that non-radiative decay paths may further limit the observed confocal counts, as varying estimates for the quantum efficiency have been reported recently [23, 32]. Lastly, the excitation intensity was often below saturation due to the low absorption cross-section at 532 nm [33], and varied over the GeV implantation depth (125 ± 20 nm) owing to the low-finesse cavity formed by the diamond membrane.

We replace the collection objective with the fiber mirror to study emitter-cavity coupling in the same region of the membrane sample. Again the sample is scanned laterally,

and the cavity length is tuned over a full free spectral range at each x-y position. A map of the cavity-coupled emission amplitude obtained at each position is shown in Fig. 24b, with an example z-scan shown in Fig. 24c. The regions of high counts in the scan correspond to cavity-funneled emission over the room-temperature-broadened ZPL (the width of this peak is ultimately set by the filters in the collection path). We study coupling to the $m = 16$ longitudinal mode, as found by fitting white light transmission data (see Fig 24d). The contours obtained from the confocal measurement are overlaid for comparison, revealing a clear spatial correspondence between emitters in the confocal scan and high emission into the cavity. The resolution in the 3D cavity scan is set by the 532 nm excitation spot size (≈ 1 μm) since the cavity waist diameter on the flat mirror is much larger (≈ 3μm).

We studied the GeV center marked with an arrow in both the confocal and cavity images, as it was well isolated. Confocal characterization confirmed that this was a single defect, with $g^2(0) = 0.25 \pm 0.16$ (see supplementary), a lifetime of $\tau = 6.0 \pm 0.1$ ns, and a strong ZPL emission centered at 602 nm. In addition, this emitter displayed a comparatively low saturation power of $P_{sat} = 3.9 \pm 0.3$ mW, implying efficient excitation.

Beyond the spatial correlations between Figs. 24a and 24b, further evidence that we are probing a cavity-coupled GeV center can be obtained by comparing emitter spectra from both setups. Fig. 14a shows a spectrum obtained in the confocal configuration for the emitter, which has strong ZPL emission around 602 nm with a FWHM linewidth of 5.22 THz. A corresponding cavity measurement can be obtained by exciting the emitter while scanning the cavity length and acquiring a spectrum at each position (Fig. 14b). Integrating the emission along one mode using a 2 nm window about the resonance results in the purple trace shown in Fig. 14c, where the noise can be attributed to mechanical instability of the cavity. To show the underlying spectral shape we also average the data using a 40 point window (orange trace). Both spectra were taken using a 605 ± 15 nm bandpass filter (Semrock), which did not limit the observed spectra. The peaks around 597 and 609 nm in Fig. 14b are due to mechanical disturbances causing the cavity to pass through the same resonance twice. The clear qualitative similarities between the confocal and cavity spectra further confirm that the collected emission is coming from a GeV center. In addition to the fundamental mode coupling shown here, we found that roughly 20% of the emission instead coupled to a higher order transverse mode (details in supplementary).

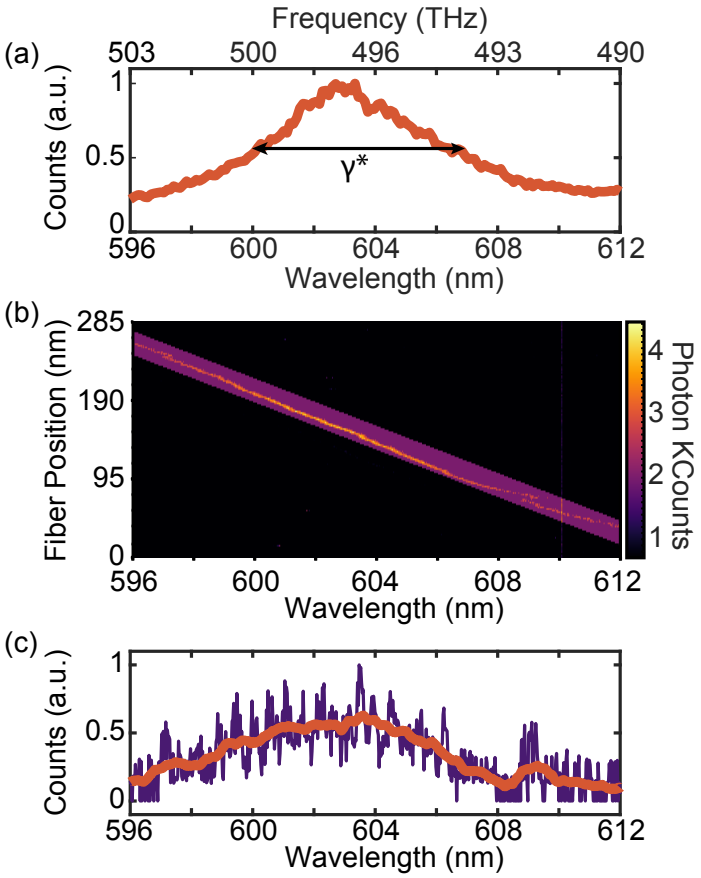

Figure 14: a) GeV center spectrum taken in the confocal configuration. The pure dephasing rate γ^* is indicated with an arrow. b) GeV center fluorescence as a function of cavity length. The colored region represents the integration window. c) Integrated spectrum taken in the cavity configuration. The purple trace shows the raw data, and the orange trace has been averaged over 40 points.

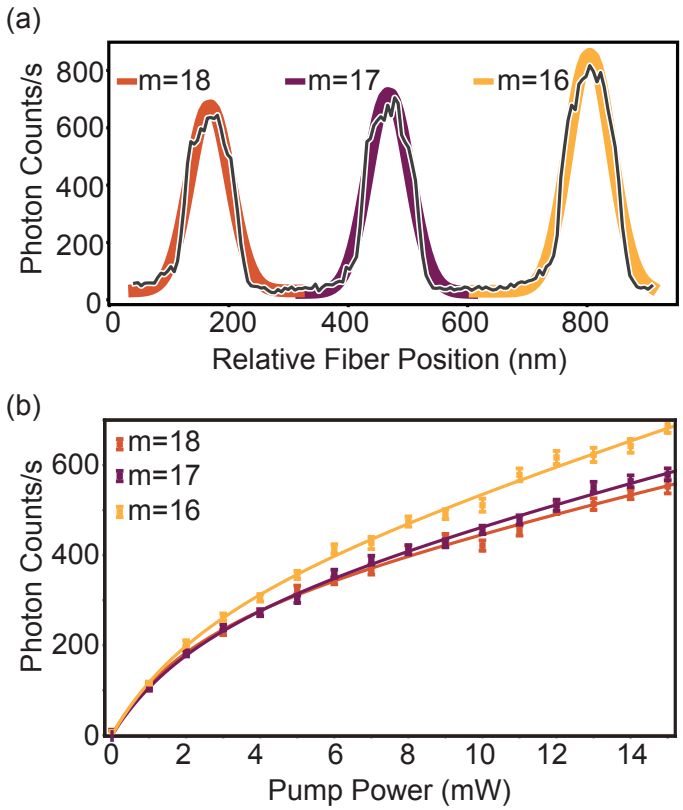

Figure 15: a) A longitudinal cavity scan for 14 mW pump power. The amplitudes of the Gaussian fits for $m = 16$, 17, and 18 are used in saturation measurements. b) Corresponding saturation curves, where error bars indicate one standard deviation on the amplitude of the fits.

In principle, comparison of GeV photon count rates in and out of the cavity enables us to quantify cavity funneling of the emitter. However, we must take care to account for different excitation intensities arising from interference effects in the diamond membrane and cavity. We thus compare saturating fluorescence counts I^{∞} (counts at infinite pump power), obtained by fitting saturation curves with the model $I(P) = I^{\infty}\frac{P}{P+P_{sat}} + c_{bg}P$, where P is excitation power, I is the observed count rate, P_{sat} is the saturation power, and c_{bg} accounts for a linear background. In the confocal setup, we measure a saturation power of $P_{sat} = 3.9 \pm 0.3$ mW and extract a saturating fluorescence count rate of $I^{\infty}_{free,meas} = 4000 \pm 400$ counts/s. This value can be corrected for the efficiency of the confocal collection path ($\eta_{free} = 0.11 \pm 0.06\%$, see supplementary), resulting in $I^{\infty}_{free} = I^{\infty}_{free,meas}/\eta_{free} = 4 \pm 2$ Mcounts/s, the total number of photons emitted by the defect. We collect photon emission between $600 - 605$ nm, corresponding to a photon spectral density of 280 ± 150 counts/(s GHz).

For comparison, we measure the saturation behavior of the emitter coupled to the m=16, 17, and 18 longitudinal modes of the cavity. For each excitation power, we measure fluorescence as a function of cavity length using the same optical filters (Fig. 15a). As expected, the cavity-coupled fluorescence decreases with mode number as the cavity mode volume increases. The amplitudes of these resonances are extracted by fitting with Gaussians, and plotted as a function of excitation power in Fig 15b. Fitting the m = 16 data to the saturation model yields $P_{sat} = 3.1 \pm 0.5$ mW and $I^{\infty}_{cav,meas} = 380 \pm 50$ counts/s. We estimate a collection efficiency of $\eta_{cav} = 10 \pm 2\%$ for the cavity setup (see supplementary), resulting in a corrected saturating fluorescence count rate of $I^{\infty}_{cav} = I^{\infty}_{cav,meas}/\eta_{cav} = 3700 \pm 700$ counts/s. Moreover, we calculate a cavity linewidth of $\kappa = 2\pi \times 1.1 \pm 0.2$ GHz (see supplementary), leading to a cavity-enhanced spectral density of 2200 ± 600 counts/(s GHz), a factor of 8 ± 5 greater than what was obtained with the confocal measurements. The experimental efficiency of emission into the $m = 16$ mode is then

$$\beta_{exp} = \frac{I^{\infty}_{cav}}{I^{\infty}_{free}} = 0.10 \pm 0.06\%. \tag{3.1}$$

We simulate the electric field distribution of the cavity mode using one-dimensional transfer matrix theory [27] with the measured dephasing rate $\gamma^* = 5.22$ THz, ZPL wavelength $\lambda = 602$ nm, and branching ratio $\xi = 0.6$. We further assume that the

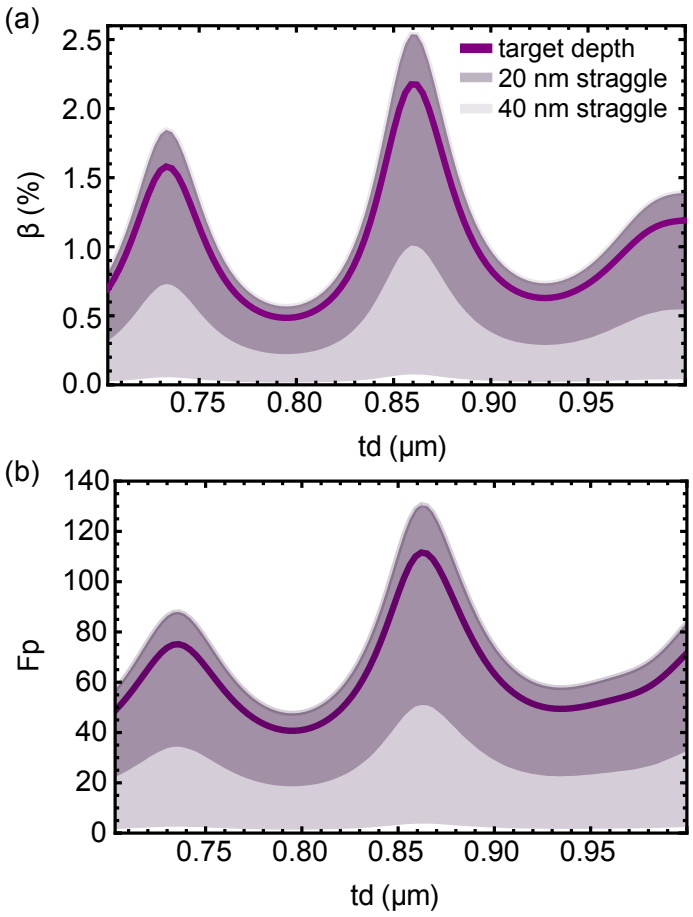

Figure 16: a) Theoretical β for an emitter resonantly coupled to the $m = 16$ mode as a function of diamond thickness. b) Corresponding Purcell enhancement of the ZPL emission for the same emitter.

optical dipole is along the $\langle 111 \rangle$-axis, as was shown for the SiV center [18]. Absorption losses in the mirrors are included through the addition of complex components in the dielectric layer refractive indices, lowering the bare cavity finesse to $\mathcal{F} \approx 21,000$ at 652.6 nm. In addition, scattering losses are introduced by adding $\sigma = 0.15$ nm-rms of surface roughness to the diamond interfaces [34, 35], reducing the membrane-in-cavity finesse to the measured value of $\mathcal{F} \approx 11,000$ at 602 nm. Finally, we use a fiber mirror radius of $R = 45$ μm and diamond thickness $t_d = 860$ nm (extracted from the fits in Fig. 24d), and include lensing effects on the cavity mode from the planar diamond-air interface in calculating the cavity waist diameter of ≈ 3 μm [36].

From the resulting electric field distribution, we can calculate β as a function of diamond thickness for an emitter resonantly coupled to the $m = 16$ cavity mode (theoretical details in supplementary). The results are shown in Fig. 16a, where the solid line corresponds to the target implantation depth of 125 nm and the shaded region reveals the spread corresponding to one and two times the nominal implantation straggle (± 20 nm), resulting in $\beta \approx 0.08 - 2.5\%$. As expected, the efficiency of emission into the cavity mode is peaked for diamond-like modes, where the electric field at the position of the emitter is maximized. This simulation can be compared against the experimentally determined value of $0.10 \pm 0.06\%$.

Cooling such a high-quality membrane to cryogenic temperatures should result in a narrowing of the ZPL optical transitions, approaching the radiative limit of $\gamma = 2\pi \times 27$ MHz for a 6.0 ns excited state lifetime. In this regime, the cavity linewidth should far exceed that of the emitter ($\kappa \gg \gamma + \gamma^*$), allowing for a Purcell enhancement of resonantly coupled optical transitions. Using the extracted system parameters, we can estimate this enhancement as

$$F_p = \frac{\beta \gamma^*}{\xi \kappa (\beta - 1)}, \tag{3.2}$$

resulting in $F_p \approx 10$. This would reduce the excited state lifetime by a factor of ≈ 7 (assuming unity quantum efficiency), with 90% of photons emitted into the ZPL. We simulate the Purcell enhancement for the same system (details in supplementary), resulting in $F_p \approx 4 - 130$ over the range of the implantation straggle (Fig. 16b), which can be compared against the current state-of-the-art for open microcavities, where the ZPL of an NV center was enhanced by a factor of $F_p = 30$ [16].

In summary, we demonstrate room temperature coupling between a single GeV center in a diamond membrane and a Fabry-Pérot microcavity. We achieve an 8-times increase in the spectral density of single photon emission, and moreover show that is it possible to couple single defect centers in membranes to high-finesse "diamond-like" modes of an open cavity system. Looking toward future experiments at cryogenic temperatures, we project a Purcell enhancement of ≈ 10 for our current device, corresponding to a 7-times reduction of the excited state lifetime. This value could be further improved by employing fiber mirrors with smaller radius of curvature, where $R = 15$ μm would roughly double the Purcell enhancement. Moving forward, the viability of the GeV should be confirmed through studies of spin coherence times at ~ 100 mK temperatures, as well as further studies of the observed dark state. Nevertheless, the advancements made in this work represent an important step toward realizing an efficient spin-photon interface for defect centers coupled to open microcavities.

Acknowledgments

We would like to thank Ruffin Evans and Mihir Bhaskar for tri-acid cleaning and annealing the membrane samples, as well as Marie-Josée Gour for assistance with membrane fabrication. L. Childress acknowledges support from Canada Foundation for Innovation and Canada Research Chairs project 229003 and 231949, Fonds de Recherche - Nature et Technologies FQRNT PR-253399, National Sciences and Engineering Research Council of Canada NSERC RGPIN 435554-13, and l'Institut Transdisciplinaire d'Information Quantique (INTRIQ). L. Childress is a CIFAR Fellow in the Quantum Information Science Program. Y. Fontana acknowledges support from SNSF Early Mobility Fellowship; CDRR was supported by a CONACYT fellowship; Y. Hi was supported by a MITACS Globalink internship.

3.1 Supplemental Material: Cavity-Enhanced Photon Emission from a Single Germanium Vacancy Center in a Diamond Membrane

3.1.1 *Diamond Membrane Fabrication*

The diamond membrane is fabricated from a $\langle 100 \rangle$-cut electronic-grade bulk diamond (Element 6), which is laser-cut laterally into 20 ± 10 μm thick diamond plates (Delaware Diamond Knives), and cleaned with a piranha solution before being bonded via Van der Waals forces to sapphire carrier wafers. We then employ a cycled $ArCl_2$ and O_2/Ar dry-etching process [37–39] to remove 4 μm of material, smoothing the surface to 0.3 nm-rms (as measured by AFM) and relieving material strain from polishing. Once etched, the samples are implanted with germanium ions at an energy of 330 keV and fluence of $10^9/cm^2$, corresponding to an approximate implantation depth of $h = \lambda/(2n_d) \approx 125 \pm 20$ nm (calculated using SRIM software [40]). The samples are then cleaned in a triacid solution (1:1:1 sulfuric, nitric, and perchloric acids), and annealed using a three step procedure [41]. After annealing, the samples are again cleaned with a triacid mixture to remove graphitization, flipped (with implanted side down) and bonded to a carrier wafers for further etching to the desired device thickness (≈1 μm). Such thin and smooth samples bond very strongly to carrier wafers, and are consequently removed in a boiling piranha mixture. The membrane is then rinsed in DI water and transferred in a water droplet (with implanted side down) onto the flat mirror, and blow-dried with nitrogen. Confocal characterization of these samples showed ≈ 6% annealing conversion efficiency from implanted ions to GeV centers.

3.1.2 *Confirmation of Single Photon Emission*

We ensure that we are studying a single GeV center by measuring the second order correlation function, as seen in Fig. 17 (19 mW pump power).

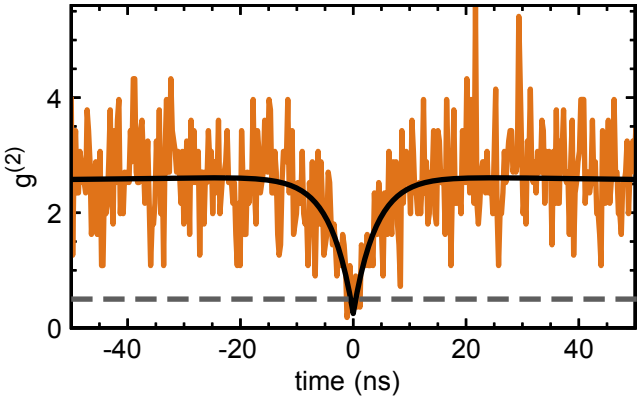

Figure 17: A second order correlation function of the studied GeV center. The fit to Eq. 3.3 is shown with a solid line, while $g^{(2)} = 0.5$ is indicated with a dashed line for reference.

We fit this data assuming a Poissonian background contribution parameterized by $\sigma = S/(S+B)$ (where S is the signal from the GeV center and B is background [42]), resulting in a measured correlation function of

$$g_m^{(2)}(\tau) = g^{(2)}(\tau)\,\sigma^2 + 1 - \sigma^2, \tag{3.3}$$

where

$$g^{(2)}(\tau) = 1 - (1+a)\,e^{-|\tau|/\tau_1} + a\,e^{-|\tau|/\tau_2}. \tag{3.4}$$

We obtain $\tau_1 = 4.0 \pm 0.5$ ns, $\tau_2 = 1.19 \pm 0.01$ ms, $a = 2.2 \pm 0.4$, and $\sigma^2 = 0.75 \pm 0.16$, resulting in $g_m^{(2)}(0) = 0.25 \pm 0.16$. We can therefore conclude that we are studying a single GeV center.

3.1.3 *Rate Analysis*

We fit Eq. 3.3 to a series of power-dependent $g^{(2)}$ measurements to obtain information regarding the population dynamics of our system (Fig. 18a). Here, we look at correlations over a large range of time scales to observe a long-lived shelving state in the electronic level structure. A high resolution example taken for pump power $P = 10.0$ mW is

shown in Fig. 18b, where the dashed line indicates $g^{(2)}(0) = 0.5$ for $\sigma^2 = 0.58$. The

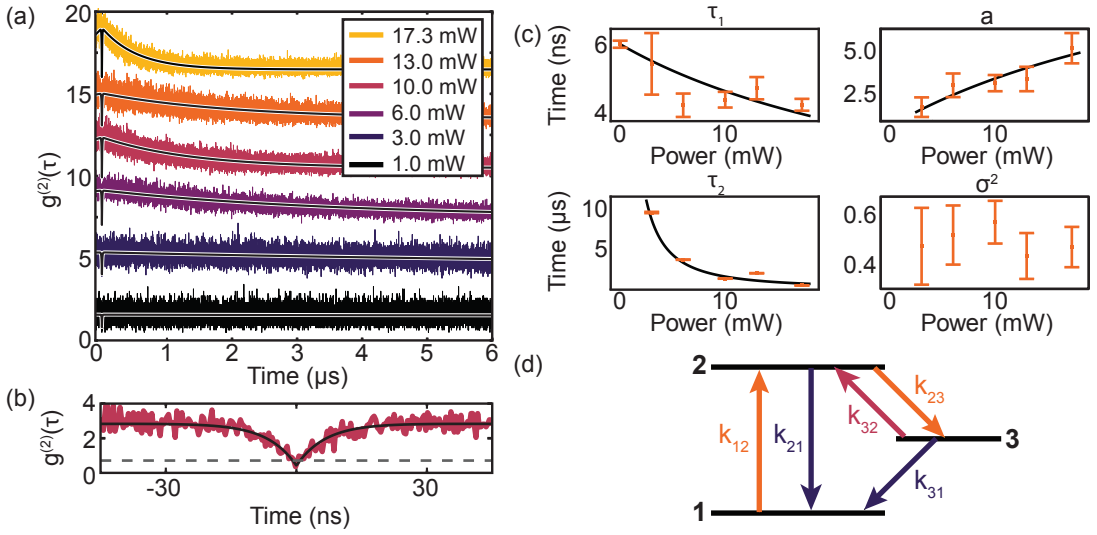

Figure 18: a) Power dependent $g^{(2)}$ measurements for the studied GeV (subsequent measurements are offset by 3 for clarity). Fits to Eq. 3.3 are shown in black. b) High resolution data for the $P = 10.0$ mW trace. The gray dashed line indicates $g^{(2)} = 0.5$ with $\sigma^2 = 0.58$. c) Extracted power dependent fitting parameters from Eq. 3.4. d) Equivalent three-level system for rate analysis.

resulting power-dependent parameters are shown in Fig. 18c. The clear bunching of the $g^{(2)}$ function at high excitation powers implies that there are three or more energy levels participating in the dynamics. In practice, we found that our data could be well described by an effective three-level model (Fig. 18d), where 1 and 2 are the ground and excited states respectively and 3 is an additional shelving state. A standard three-level model with k_{12} as the only power-dependent rate does not fit the data; we therefore include ionization from the excited and shelving states with linear power dependence. This has been used successfully in describing the rates of single SiV centers [29, 43]. The power-dependent intersystem rates are either proportional to power (orange arrows in Fig. 18d) or have linear and constant terms (red arrow):

$$k_{12} = c_{12}P \tag{3.5}$$

$$k_{32} = c_{32}P \tag{3.6}$$

$$k_{23} = c_{23}P + k_{23}^{0}, \tag{3.7}$$

where k_{23}^0 and c_{ij} are constants. The rates k_{21} and k_{31} are assumed to be independent of excitation power (purple arrows). The fitting parameters in Eq. 3.3 are related to these intersystem rates by

$$\tau_{1,2} = \frac{2}{\left(A \pm \sqrt{A^2 - 4B}\right)} \tag{3.8}$$

$$a = \frac{1 - \tau_2 \left(k_{31} + k_{32}\right)}{\left(k_{31} + k_{32}\right)\left(\tau_2 - \tau_1\right)}, \tag{3.9}$$

where

$$A = k_{12} + k_{21} + k_{23} + k_{31} + k_{32} \tag{3.10}$$

$$B = k_{23}k_{31} + k_{21}\left(k_{31} + k_{32}\right) + k_{12}\left(k_{23} + k_{31} + k_{32}\right). \tag{3.11}$$

The power-dependent fit parameters are plotted in Fig. 18d, where the $P = 0$ value of τ_1 is taken from an additional lifetime measurement. Fits to the three-level model are shown with black lines, leading to the extracted rates of

$$\begin{aligned} c_{12} &= 4.6\ \text{MHz/mW} \\ c_{23} &= 0.20\ \text{MHz/mW} \\ c_{32} &= 14\ \text{kHz/mW} \\ k_{23}^0 &= 0.37\ \text{MHz} \\ k_{21} &= 0.17\ \text{GHz} \\ k_{31} &= 0.0\ \text{MHz}. \end{aligned}$$

From these parameters, the steady-state population of the excited state in the limit $P \to \infty$ is given by

$$\rho_2^{ss,\infty} = \frac{1}{1 + c_{23}/c_{32}} = 0.067,$$

and the total de-excitation rate (including nonradiative decay) is

$$\gamma_{21} = \rho_2^{ss,\infty}\, k_{21} = 11\,\text{MHz}.$$

This analysis implies that the studied GeV center spends 93% of it's time in a long-lived dark state (such as a different charge state) at high pump power, reducing the overall emission dramatically.

3.1.4 *White Light Cavity Transmission*

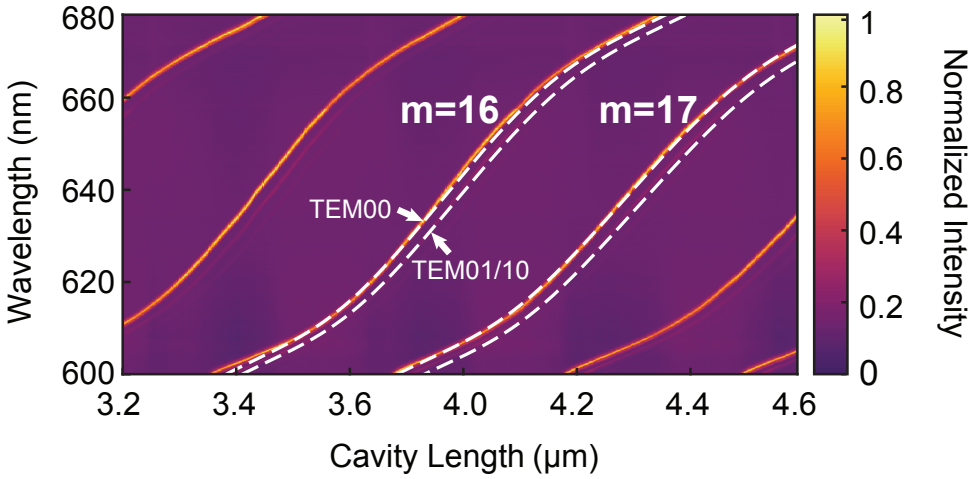

Figure 19: White light cavity transmission spectrum as a function of length. The dashed lines correspond to numerical fits to the fundamental (TEM00) and first-order transverse (TEM01/10) modes for the $m = 16$ and 17 longitudinal modes.

Cavity characteristics such as mode number m and diamond thickness t_d can be extracted by characterizing the white light transmission spectrum as a function of cavity length. We couple a broadband fiber laser (NKT Photonics) through the fiber mirror, and collect the transmission through the flat mirror as a function of cavity length (Fig. 19), revealing the cavity mode structure. We fit the fundamental and first order transverse modes of two adjacent longitudinal modes simultaneously (dashed lines in Fig. 19) to a transfer matrix model including Guoy phase [27]. From this model, we extract a membrane thickness $t_d = 860$ nm, fiber mirror radius of curvature $R = 45$ μm, as well as the mode numbers m and cavity lengths L labeled on the plot. The $m = 16$ resonance was the lowest longitudinal mode number achievable before the fiber mirror made physical contact with the membrane. Deviation of the fit from the measured data could be

due to minor differences between the simulated and actual mirror layer thicknesses or wavelength dependent variation in the refractive indices.

Furthermore, we use the white light spectrum to estimate the cavity decay rate at 602 nm. We first measure the cavity linewidth to be $\Delta L = 27 \pm 4$ pm, corresponding to a finesse of $\mathcal{F}_L = \lambda/(2\,\Delta L) = 11000 \pm 2000$. The magnitude of the slope of the $m = 16$ resonance at 602 nm is 40 ± 2 THz/μm, resulting in a cavity linewidth in frequency of $\kappa = 2\pi \times 1.1 \pm 0.2$ GHz.

3.1.5 *Higher Order Modes*

Our analysis assumes that we only collect emission coupled to a fundamental cavity mode as the single mode fiber in our collection path should spatially filter out other transverse modes. In practice, we do collect some emission coupled to higher order modes (see Fig. 20), comprising $20 \pm 5\%$ of the total emission in this particular scan. We attribute this to lateral misalignment of the cavity mode on the collection fiber, which may vary slightly over time due to experimental drift and realignment. The count rate from the fundamental cavity mode is therefore $I_{fund,meas} = I_{cav,meas}/\eta_{hotm}$ with the correction factor $\eta_{hotm} = 1.25 \pm 0.08$ for higher order transverse modes.

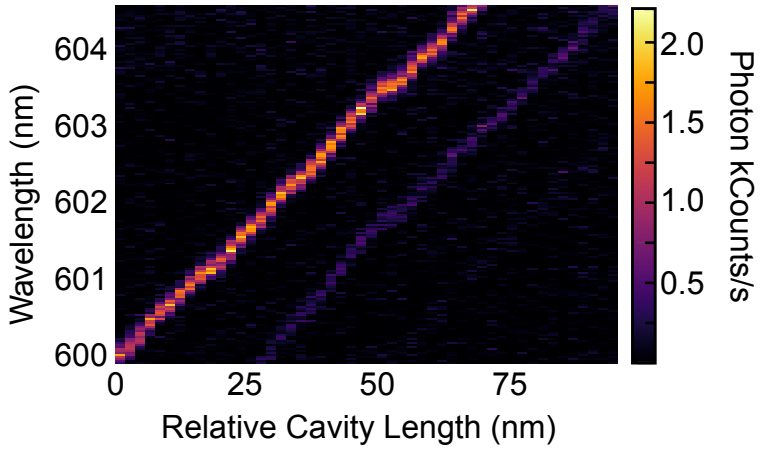

Figure 20: GeV center fluorescence as a function of cavity length. A weak higher order mode is visible at shorter wavelengths compared to the bright fundamental mode.

3.1.6 *Collection Efficiency Calculations*

Comparison of the saturating fluorescence counts in the confocal and cavity systems necessitates careful characterization of the measurement collection efficiencies. To extract the GeV center free-space emission from the confocal measurements, we first simulate the possible dipole emission patterns for our system including the membrane and mirror coating geometry (see Sec. 3.1.7), and obtain a collection efficiency of 0.07 ± 0.02 for a 0.7 NA collection objective. We must further correct for spectral filtering, which can be estimated by integrating the GeV center spectrum (see Fig. 22a, Sec. 3.1.9) between $600 - 605$ nm ($\approx 496 - 500$ THz), resulting in a factor of 0.272 ± 0.004. We estimate an efficiency of 0.22 ± 0.1 for the single mode fiber coupling by comparing counts from the same emitter using a multimode fiber, where we assumed unity efficiency for the latter. Additional collection efficiencies exclusive to the confocal detection path are detailed in Tab. 2.

Optical Element	Collection Efficiency
dipole collection by objective	0.07 ± 0.02
spectral filtering	0.272 ± 0.004
objective transmission (602 nm)	0.80 ± 0.01
two dielectric mirrors	0.98 ± 0.01
collection fiber coupling	0.22 ± 0.10
total $\eta_{free,ex}$	0.0033 ± 0.0018

Table 2: Confocal optical elements.

Similarly, all of the collection efficiencies exclusive to the cavity setup are listed in Tab. 3. The cavity escape efficiency provides the normalized transmission through the flat mirror including all cavity losses (cavity transmission, scattering, and absorption, as well as reflection from the back mirror interface). Using our transfer matrix model, we estimate this quantity to be 0.34 ± 0.02 at 602 nm for the $m = 16$ mode, where the error is estimated from the values at 600 and 605 nm. We assume that all photons emitted through the flat mirror are collected by the objective due to the comparatively low NA of the cavity mode (≈ 0.1). We image the collimated cavity mode yielding a

beam radius of 690 ± 70 μm, which is used to calculate a fiber coupling efficiency of 0.89 ± 0.09 (assuming perfect lateral alignment and neglecting aberrations). We only consider emission coupled to a fundamental cavity mode, and correct for coupling to higher order transverse modes with a factor of 1.25 ± 0.08 (see Sec. 3.1.5).

Optical Element	Collection Efficiency
cavity escape efficiency	0.34 ± 0.02
objective transmission (602 nm)	0.91 ± 0.01
four dielectric mirrors	0.96 ± 0.02
dichroic transmission	0.93 ± 0.01
collection fiber coupling	0.89 ± 0.09
transverse mode contribution	1.25 ± 0.08
total $\eta_{cav,ex}$	0.31 ± 0.04

Table 3: Cavity optical elements.

Finally, there are a number of optical components that are common to both the cavity and confocal setups detailed in Tab. 4.

Optical Element	Collection Efficiency
fiber coupling lens	1.00 ± 0.01
tunable long pass filter	0.92 ± 0.02
tunable short pass filter	0.92 ± 0.02
532 nm notch filter	0.97 ± 0.02
transmission at fiber facets	0.94 ± 0.03
APD telescope lenses	0.98 ± 0.02
APD efficiency (600 nm)	0.45 ± 0.02
total η_{comm}	0.33 ± 0.02

Table 4: Common optical elements.

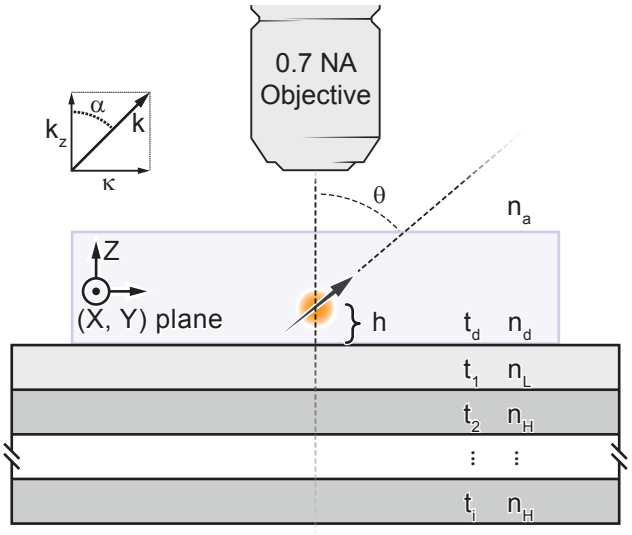

Figure 21: An illustration of the dipole simulation parameters.

Using these values, the free-space and cavity emission of the GeV center should be corrected by $\eta_{free} = \eta_{free,ex}\,\eta_{comm} = 0.11 \pm 0.06\%$, and $\eta_{cav} = \eta_{cav,ex}\eta_{comm} = 10 \pm 2\%$ respectively.

3.1.7 *Dipole Emission Calculation*

To calculate the collection efficiency in the confocal setup, the directional emission of the GeV center must be determined since our objective does not collect light emitted at angles exceeding the NA (0.7), or light that is confined to guided modes in the diamond membrane. To calculate this efficiency, we model the spontaneous emission from a GeV center as that of a classical dipole (this assumption is valid as the spatial extent of the GeV is much smaller than the emission wavelength, and the transition orbital is not affected by the dielectric mirror [44]). Using the formalism developed by Neyts *et al.* [45], we calculate the angular emission pattern for a point dipole positioned $h = 125$ nm above the flat mirror in a diamond layer with thickness t_d=860 nm (see Fig. 21). The mirror coating is modelled with 50 alternating layers of SiO_2 and Ta_2O_5 with the design layer thicknesses t_i, deposited on a fused silica substrate.

We consider the four orientations of GeV centers, which have quantization axes along the family of $\langle 111 \rangle$-crystallographic directions. The micron-scale thickness and high re-

fractive index of diamond makes it an efficient waveguide, in contrast to the layers of the Bragg stack which are too thin to support modes in the transverse plane. Consequently, between 82% and 99% of the emission is trapped in guided diamond modes depending on the angle, α, of the dipole. The optical dipole orientation of the GeV center has not been experimentally determined, but by symmetry we assume that it is either a single dipole along the $\langle 111 \rangle$ direction, or two perpendicular dipoles in the (111) plane. A dipole along the $\langle 111 \rangle$ axis makes an angle $\alpha = 54.7^\circ$ to the (100) plane (the membrane surface) resulting in 7.5% of the light being collected by the objective. For a dipole in the (111) plane, α can be between 35.3° and 90°, giving collection efficiencies of 4.6% and 13.5% respectively. The average collection efficiency of the two dipoles in this plane is therefore also 7.5%. We estimate the error on this value by further calculating the collection efficiency for a dipole located ± 20 nm from the target depth (corresponding to the simulated straggle), resulting in 7.6% and 5.5% respectively. We therefore estimate a collection efficiency of $7 \pm 2\%$.

3.1.8 *Cavity Funneling Theory*

We calculate β by modeling the GeV center as an emitter with n optical transitions (including a phonon sideband), where the efficiency of emission into the cavity mode is given by [28]

$$\beta = \frac{\sum_{j=0}^{n-1} R_j}{\gamma + \sum_{j=0}^{n-1} R_j}, \tag{3.12}$$

where R_j is the emitter-cavity coupling rate of the jth transition. In the bad emitter limit ($\gamma_j^* \gg \gamma + \kappa$), this is given by

$$R_j = \frac{4g_j^2}{\gamma_j^*} \frac{1}{1 + \left(\frac{2\delta_j}{\gamma_j^*}\right)^2}, \tag{3.13}$$

where g_j is the coupling rate of the jth transition to the cavity (which is related to the overall coupling rate g by the branching ratio ξ_j by $g_j = \sqrt{\xi_j} g$), δ_j is the transition-

cavity detuning, and γ_j^* is the homogeneous dephasing rate [28]. If the cavity is resonantly coupled to the ZPL transition (labeled $i = 0$), emission from other transitions into the cavity mode can be neglected if

$$\frac{\xi_0}{\gamma_0^*} \gg \sum_{j \neq 0} \frac{\xi_j}{\gamma_j^*} \frac{1}{1 + \left(\frac{2\delta_j}{\gamma_j^*}\right)^2}. \tag{3.14}$$

For the case of the GeV center, we find that the phonon sideband (PSB) transitions contribute negligibly to the cavity emission when on resonance with the ZPL (analysis in Sec. 22) and the total efficiency can then be approximated as

$$\beta \approx \frac{R_0}{\gamma + R_0}, \tag{3.15}$$

where in the main text we neglect the $i = 0$ subscript. The total cavity-coupling rate is given by

$$g = \sqrt{\frac{3\, c\, \lambda^2\, \gamma}{8\pi\, n_d^3\, V}} \frac{|\vec{f}(z_0) \cdot \vec{\mu}\,|}{|\vec{\mu}|}, \tag{3.16}$$

where $\vec{\mu}$ is the optical dipole moment of the emitter, $\vec{f}(z_0)$ is a complex vector describing the electric field polarization and normalized amplitude at the position of the emitter (z_0), n_d is the refractive index of diamond, and V is the cavity mode volume, given approximately by

$$V = \frac{\pi \omega_0^2}{2} \frac{\int n^2(z) |E(z)|^2 dz}{n_d^2 |E(z_0)|^2}, \tag{3.17}$$

where ω_0 is the cavity waist radius and $E(z)$ is the cavity electric field at position z along the cavity axis.

3.1.9 *Spectra Fitting*

In the main text, we neglected contributions from the PSB transitions. Here, we show the validity of this approximation by estimating the emission into the cavity mode from PSB transitions when on resonance with the ZPL. To do this, we analyze the spectrum of the emitter from 585-630 nm ($\approx 476 - 513$ THz), over which we assume the response of our optics and detector are constant. To account for background from the diamond, we took a spectrum on (Fig. 22a, orange trace) and off (yellow trace) the studied GeV center. The high signal to noise ratio achieved in our confocal scans between 600-605 nm ensured that this background was not coming from an emitter, and indeed it agrees well with published data on the second-order Raman transition in diamond for 532 nm excitation [20, 46]. We correct the raw GeV spectrum using this background by normalizing to the area under the first order Raman transition in each scan before subtraction, resulting in the purple trace in Fig. 22a.

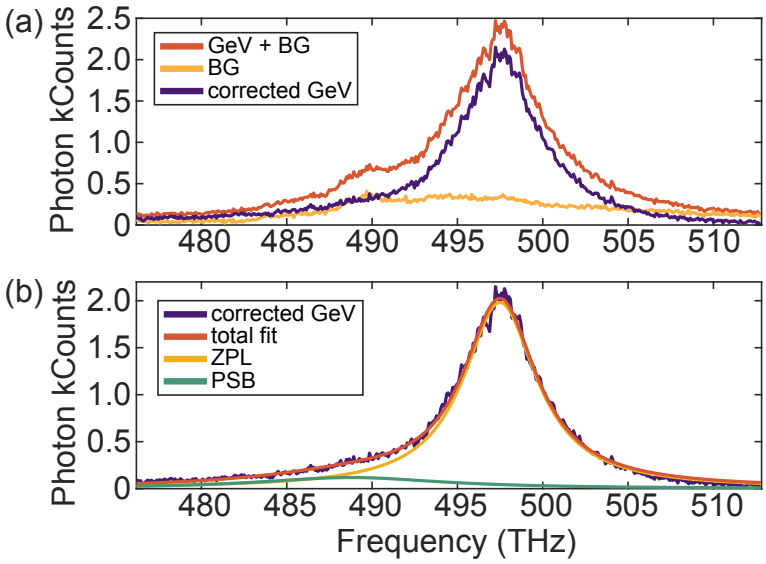

Figure 22: a) A raw GeV spectrum (orange), background diamond spectrum (yellow), and the corrected GeV spectrum (purple). b) A two-Lorentzian fit (orange) to the corrected GeV spectrum (purple), with the individual contributions of the ZPL (yellow) and PSB (green) plotted.

The corrected spectrum was fit to the sum of two Lorentzians (of the form $I(\nu) = A\frac{(\gamma^*/4\pi)^2}{(\gamma^*/4\pi)^2+(\nu-\nu_0)^2}$) with zero constant offset (orange trace, Fig. 22b), representing the

ZPL transition (yellow), and a broad PSB transition (green), with fit parameters listed in Tab. 5.

Parameter	ZPL	PSB
A (counts)	1980 ± 10	118 ± 6
$\gamma^*/2\pi$ (THz)	5.22 ± 0.05	13.4 ± 1
ν_0 (THz)	497.49 ± 0.01	488.8 ± 0.5

Table 5: Spectrum fit parameters.

Comparing the integrated counts for each of these transitions results in 87% of the photons occurring in the ZPL. The Huang-Rhys factor for the GeV center was reported to be approximately 0.5 [47], resulting in a ZPL branching ratio of 60%. We therefore conclude that the fitted PSB transition comprises 9% of the total emission, and the other 31% of the PSB emission must occur at longer wavelengths. Considering only the fitted transitions, we find that it is valid to neglect contributions from the PSB when the cavity is on resonance with the ZPL, since

$$\left(\frac{\xi_{ZPL}}{\gamma^*_{ZPL}}\right) \Bigg/ \left(\frac{\xi_{PSB}}{\gamma^*_{PSB}} \frac{1}{1+\left(\frac{2\delta_{PSB}}{\gamma^*_{PSB}}\right)^2}\right) \approx 300, \tag{3.18}$$

where $\delta_{PSB} = \nu_{ZPL} - \nu_{PSB}$. We can therefore also neglect contributions from other PSB transitions which are necessarily further detuned, and assume that only photons from the ZPL are emitted into the cavity mode.

References

1. Doherty, M. W., Manson, N. B., Delaney, P., Jelezko, F., Wrachtrup, J. & Hollenberg, L. C. The nitrogen-vacancy colour centre in diamond. *Physics Reports* **528,** 1 (2013).
2. Rose, B. C., Huang, D., Zhang, Z.-H., Stevenson, P., Tyryshkin, A. M., Sangtawesin, S., Srinivasan, S., Loudin, L., Markham, M. L., Edmonds, A. M., *et al.* Observation of an environmentally insensitive solid-state spin defect in diamond. *Science* **361,** 60 (2018).
3. Sukachev, D. D., Sipahigil, A., Nguyen, C. T., Bhaskar, M. K., Evans, R. E., Jelezko, F. & Lukin, M. D. Silicon-vacancy spin qubit in diamond: a quantum memory exceeding 10 ms with single-shot state readout. *Physical Review Letters* **119,** 223602 (2017).
4. Kimble, H. J. The quantum internet. *Nature* **453,** 1023 (2008).
5. Wehner, S., Elkouss, D. & Hanson, R. Quantum internet: A vision for the road ahead. *Science* **362,** eaam9288 (2018).
6. Togan, E., Chu, Y., Trifonov, A., Jiang, L., Maze, J., Childress, L., Dutt, M. G., Sørensen, A. S., Hemmer, P., Zibrov, A. S., *et al.* Quantum entanglement between an optical photon and a solid-state spin qubit. *Nature* **466,** 730 (2010).
7. Bernien, H., Childress, L., Robledo, L., Markham, M., Twitchen, D. & Hanson, R. Two-photon quantum interference from separate nitrogen vacancy centers in diamond. *Physical Review Letters* **108,** 043604 (2012).
8. Bernien, H., Hensen, B., Pfaff, W., Koolstra, G., Blok, M., Robledo, L., Taminiau, T., Markham, M., Twitchen, D., Childress, L., *et al.* Heralded entanglement between solid-state qubits separated by three metres. *Nature* **497,** 86 (2013).
9. Hensen, B., Bernien, H., Dréau, A. E., Reiserer, A., Kalb, N., Blok, M. S., Ruitenberg, J., Vermeulen, R. F., Schouten, R. N., Abellán, C., *et al.* Loophole-free Bell inequality violation using electron spins separated by 1.3 kilometres. *Nature* **526,** 682 (2015).

10. Pfaff, W., Hensen, B., Bernien, H., van Dam, S. B., Blok, M. S., Taminiau, T. H., Tiggelman, M. J., Schouten, R. N., Markham, M., Twitchen, D. J., *et al.* Unconditional quantum teleportation between distant solid-state quantum bits. *Science* **345,** 532 (2014).

11. Maurer, P. C., Kucsko, G., Latta, C., Jiang, L., Yao, N. Y., Bennett, S. D., Pastawski, F., Hunger, D., Chisholm, N., Markham, M., *et al.* Room-temperature quantum bit memory exceeding one second. *Science* **336,** 1283 (2012).

12. Kalb, N., Reiserer, A. A., Humphreys, P. C., Bakermans, J. J., Kamerling, S. J., Nickerson, N. H., Benjamin, S. C., Twitchen, D. J., Markham, M. & Hanson, R. Entanglement distillation between solid-state quantum network nodes. *Science* **356,** 928 (2017).

13. Humphreys, P. C., Kalb, N., Morits, J. P., Schouten, R. N., Vermeulen, R. F., Twitchen, D. J., Markham, M. & Hanson, R. Deterministic delivery of remote entanglement on a quantum network. *Nature* **558,** 268 (2018).

14. Faraon, A., Santori, C., Huang, Z., Acosta, V. M. & Beausoleil, R. G. Coupling of nitrogen-vacancy centers to photonic crystal cavities in monocrystalline diamond. *Physical Review Letters* **109,** 033604 (2012).

15. Li, L., Schröder, T., Chen, E. H., Walsh, M., Bayn, I., Goldstein, J., Gaathon, O., Trusheim, M. E., Lu, M., Mower, J., *et al.* Coherent spin control of a nanocavity-enhanced qubit in diamond. *Nature Communications* **6,** 6173 (2015).

16. Riedel, D., Söllner, I., Shields, B. J., Starosielec, S., Appel, P., Neu, E., Maletinsky, P. & Warburton, R. J. Deterministic enhancement of coherent photon generation from a nitrogen-vacancy center in ultrapure diamond. *Physical Review X* **7,** 031040 (2017).

17. Hepp, C., Müller, T., Waselowski, V., Becker, J. N., Pingault, B., Sternschulte, H., Steinmüller-Nethl, D., Gali, A., Maze, J. R., Atatüre, M., *et al.* Electronic structure of the silicon vacancy color center in diamond. *Physical Review Letters* **112,** 036405 (2014).

18. Rogers, L. J., Jahnke, K. D., Doherty, M. W., Dietrich, A., McGuinness, L. P., Müller, C., Teraji, T., Sumiya, H., Isoya, J., Manson, N. B., *et al.* Electronic structure of the negatively charged silicon-vacancy center in diamond. *Physical Review B* **89,** 235101 (2014).

19. Siyushev, P., Metsch, M. H., Ijaz, A., Binder, J. M., Bhaskar, M. K., Sukachev, D. D., Sipahigil, A., Evans, R. E., Nguyen, C. T., Lukin, M. D., *et al.* Optical and microwave control of germanium-vacancy center spins in diamond. *Physical Review B* **96,** 081201 (2017).

20. Iwasaki, T., Ishibashi, F., Miyamoto, Y., Doi, Y., Kobayashi, S., Miyazaki, T., Tahara, K., Jahnke, K. D., Rogers, L. J., Naydenov, B., *et al.* Germanium-vacancy single color centers in diamond. *Scientific Reports* **5,** 12882 (2015).

21. Sohn, Y.-I., Meesala, S., Pingault, B., Atikian, H. A., Holzgrafe, J., Gündoğan, M., Stavrakas, C., Stanley, M. J., Sipahigil, A., Choi, J., *et al.* Controlling the coherence of a diamond spin qubit through its strain environment. *Nature Communications* **9,** 2012 (2018).

22. Evans, R. E., Sipahigil, A., Sukachev, D. D., Zibrov, A. S. & Lukin, M. D. Narrow-linewidth homogeneous optical emitters in diamond nanostructures via silicon ion implantation. *Physical Review Applied* **5,** 044010 (2016).

23. Bhaskar, M. K. *et al.* Quantum nonlinear optics with a germanium-vacancy color center in a nanoscale diamond waveguide. *Physical Review Letters* **118** (2017).

24. Evans, R. E., Bhaskar, M. K., Sukachev, D. D., Nguyen, C. T., Sipahigil, A., Burek, M. J., Machielse, B., Zhang, G. H., Zibrov, A. S., Bielejec, E., *et al.* Photon-mediated interactions between quantum emitters in a diamond nanocavity. *Science* **362,** 662 (2018).

25. Sipahigil, A., Evans, R. E., Sukachev, D. D., Burek, M. J., Borregaard, J., Bhaskar, M. K., Nguyen, C. T., Pacheco, J. L., Atikian, H. A., Meuwly, C., *et al.* An integrated diamond nanophotonics platform for quantum-optical networks. *Science* **354,** 847 (2016).

26. Ruf, M., IJspeert, M., van Dam, S., de Jong, N., van den Berg, H., Evers, G. & Hanson, R. Optically coherent nitrogen-vacancy centers in μm-thin etched diamond membranes. *Nano Letters* **19,** 3987 (2019).

27. Janitz, E., Ruf, M., Dimock, M., Bourassa, A., Sankey, J. & Childress, L. Fabry-Perot microcavity for diamond-based photonics. *Physical Review A* **92,** 043844 (2015).

28. Albrecht, R., Bommer, A., Deutsch, C., Reichel, J. & Becher, C. Coupling of a single nitrogen-vacancy center in diamond to a fiber-based microcavity. *Physical Review Letters* **110** (2013).

29. Benedikter, J., Kaupp, H., Hümmer, T., Liang, Y., Bommer, A., Becher, C., Krueger, A., Smith, J. M., Hänsch, T. W. & Hunger, D. Cavity-enhanced single-photon source based on the silicon-vacancy center in diamond. *Physical Review Applied* **7,** 024031 (2017).

30. Grange, T., Hornecker, G., Hunger, D., Poizat, J.-P., Gérard, J.-M., Senellart, P. & Auffèves, A. Cavity-funneled generation of indistinguishable single photons from strongly dissipative quantum emitters. *Physical Review Letters* **114,** 193601 (2015).

31. Hunger, D., Steinmetz, T., Colombe, Y., Deutsch, C., Hänsch, T. W. & Reichel, J. A fiber Fabry-Perot cavity with high finesse. *New Journal of Physics* **12,** 065038 (2010).

32. Chen, D., Mu, Z., Zhou, Y., Froech, J., Diederichs, C., Zheludev, N., Aharonovich, I. & Gao, W.-b. Optical gating of resonance fluorescence from a single germanium vacancy color center in diamond. *arXiv preprint arXiv:1901.09231* (2019).

33. Häußler, S., Thiering, G., Dietrich, A., Waasem, N., Teraji, T., Isoya, J., Iwasaki, T., Hatano, M., Jelezko, F., Gali, A., *et al.* Photoluminescence excitation spectroscopy of SiV- and GeV- color center in diamond. *New Journal of Physics* **19,** 063036 (2017).

34. Katsidis, C. C. & Siapkas, D. I. General transfer-matrix method for optical multilayer systems with coherent, partially coherent, and incoherent interference. *Applied Optics* **41,** 3978 (2002).

35. Arnon, O. Loss mechanisms in dielectric optical interference devices. *Applied Optics* **16,** 2147 (1977).

36. Van Dam, S. B., Ruf, M. & Hanson, R. Optimal design of diamond-air microcavities for quantum networks using an analytical approach. *New Journal of Physics* **20,** 115004 (2018).

37. Hausmann, B. J. M. *et al.* Integrated diamond networks for quantum nanophotonics. *Nano Letters* **12,** 1578 (2012).

38. Latawiec, P., Venkataraman, V., Burek, M. J., Hausmann, B. J., Bulu, I. & Lončar, M. On-chip diamond Raman laser. *Optica* **2,** 924 (2015).

39. Appel, P., Neu, E., Ganzhorn, M., Barfuss, A., Batzer, M., Gratz, M., Tschöpe, A. & Maletinsky, P. Fabrication of all diamond scanning probes for nanoscale magnetometry. *Review of Scientific Instruments* **87,** 063703 (2016).

40. Ziegler, J. F., Ziegler, M. D. & Biersack, J. P. SRIM–The stopping and range of ions in matter. *Nuclear Instruments and Methods in Physics Research Section B: Beam Interactions with Materials and Atoms* **268,** 1818 (2010).

41. Chu, Y. *et al.* Coherent optical transitions in implanted nitrogen vacancy centers. *Nano Letters* **14,** 1982 (2014).

42. Brouri, R., Beveratos, A., Poizat, J.-P. & Grangier, P. Photon antibunching in the fluorescence of individual color centers in diamond. *Optics Letters* **25,** 1294 (2000).

43. Neu, E., Agio, M. & Becher, C. Photophysics of single silicon vacancy centers in diamond: implications for single photon emission. *Optics Express* **20,** 19956 (2012).

44. Lukosz, W. & Kunz, R. E. Light emission by magnetic and electric dipoles close to a plane interface I Total radiated power. *Journal of the Optical Society of America* **67,** 1607 (1977).

45. Neyts, K. A. Simulation of light emission from thin-film microcavities. *Journal of the Optical Society of America A* **15,** 962 (1998).

46. Solin, S. A. & Ramdas, A. K. Raman Spectrum of Diamond. *Physical Review B* **1,** 1687 (1970).

47. Palyanov, Y. N., Kupriyanov, I. N., Borzdov, Y. M. & Surovtsev, N. V. Germanium: a new catalyst for diamond synthesis and a new optically active impurity in diamond. *Scientific Reports* **5,** 14789 (2015).

Preface to Chapter 4

The goal of our fiber cavity platform is to enhance the coherent optical transitions of atomic defects in diamond via resonant cavity coupling. For open cavity systems, this requires tuning the mirror spacing and consequently the cavity frequency to that of a fixed optical transition. In this final manuscript, we make progress toward this goal by using the Pound-Drever-Hall scheme to lock the fiber mirror position to a laser frequency. This simple and rigid design allows us to obtain a measured feedback bandwidth of 44 kHz, and is suitable for use in cryogenic and high vacuum environments.

4

A High Mechanical Bandwidth Fiber-Coupled Fabry-Perot Cavity

Erika Janitz, Maximilian Ruf, Yannik Fontana, Jack Sankey, and Lilian Childress

Department of Physics, McGill University, Montreal CA

This chapter has been published in Optics Express.
Journal reference: Optics Express **25**, 20932 (2017).

Abstract

Fiber-based optical microcavities exhibit high quality factor and low mode volume resonances that make them attractive for coupling light to individual atoms or other microscopic systems. Moreover, their low mass should lead to excellent mechanical response up to high frequencies, opening the possibility for high bandwidth stabilization of the cavity length. Here, we demonstrate a locking bandwidth of 44 kHz achieved using a simple, compact design that exploits these properties. Owing to the simplicity of fiber feedthroughs and lack of free-space alignment, this design is inherently compatible with vacuum and cryogenic environments. We measure the transfer function of the feedback circuit (closed-loop) and the cavity mount itself (open-loop), which, combined with simulations of the mechanical response of our device, provide insight into underlying limitations of the design as well as further improvements that can be made.

4.1 Introduction

High finesse Fabry-Perot cavities have extensive applications in spectroscopy [1, 2] and precision measurement [3, 4], as well as fundamental research in quantum optics [5, 6].

In many situations, the cavity must be locked to a frequency reference (for example, an atomic transition) to compensate for external disturbances and maintain a specific resonant frequency [6–9]. Such locking is typically accomplished by monitoring the transmission or reflection of light at the reference frequency, and feeding the signal back to a mechanical transducer that adjusts a mirror to stabilize the cavity length. The bandwidth of the lock (here defined as the frequency below which noise is suppressed) represents a key figure of merit, and determines the maximal noise suppression that can be achieved at low frequencies. The mechanical response of the mirrors and mirror mount typically limit the bandwidth, requiring careful engineering to suppress low-frequency vibrational modes.

Fiber-based micro-mirrors [10] offer a promising technology for creating tunable, high-finesse optical micro-cavities. These cavities can achieve very small mode waists, which are advantageous for cavity quantum electrodynamics applications; so far, they have been coupled to atoms [11–13], ions [9, 14], optomechanical systems [15, 16], molecules[17], and crystalline defect centers [18–20]. Moreover, the light weight of the fiber mirror suggests that it should be possible to achieve a high bandwidth feedback loop for length stabilization of such a cavity.

Previous work on locking fiber-coupled cavities has demonstrated mechanical feedback with bandwidths of only $1 - 3$ kHz [21, 22] (we note that for the 1 kHz case the first limiting mechanical resonance occurred at 25 kHz). Adding photothermal stabilization can further improve noise suppression for frequencies up to 500 kHz [21, 22]. Such "self-stable" operation is achieved via intra-cavity heating of the mirror coatings by an incident laser; disturbances that change the length of the cavity affect the intra-cavity power, which in turn induces thermal expansion that stabilizes the effective length. This method of thermal stabilization comes at the cost of high intra-cavity power on the order of $1 - 10$ Watts [21, 22], presenting a challenge for cryogenic operation or for coupling cavities to solid-state systems where non-resonant absorption of the locking light cannot be neglected.

In contrast, higher locking bandwidths can also be achieved using careful mechanical and electrical engineering of the cavity mount and feedback circuit. An optimized design for a macroscopic Fabry-Perot cavity composed of two small free-space mirrors achieved a bandwidth of up to 180 kHz [23]. However, this result relied on the damping properties of lead inside the mirror mount to reduce the impact of low-frequency me-

chanical resonances on the feedback circuit, which limits its function to non-cryogenic applications.

Here, we investigate the bandwidth attainable when electronically feeding back to a piezo-mounted fiber mirror. Our approach does not rely on specific material properties or intra-cavity heating; instead, we take advantage of the intrinsic high-frequency response available with a lightweight fiber mirror. We measure the full transfer function for the feedback circuit, and find that a locking bandwidth of 44 kHz is readily obtained. With a combination of direct measurements of the system's transfer function and finite-element simulations, we identify limiting features in the mechanical response associated with resonances in the mount, fiber, and epoxy, and provide an additional set of design considerations.

4.2 Experimental Setup

4.2.1 *Device Design and Construction*

Our cavity is formed by a macroscopic flat mirror and a microscopic spherical mirror fabricated on the tip of a single mode optical fiber (Fig. 23(a)), using a CO_2 laser ablation process [10, 24]. Both mirror substrates are coated with a high reflectivity dielectric mirror (LASEROPTIK) with the reflection band centered at 1550 nm. This coating exhibits a finesse of $\mathcal{F} = 21000 \pm 2000$, measured after annealing for 5 hours at 300°C under atmospheric conditions [25].

The device is composed of two aluminum pieces onto which each mirror is mounted; the two-piece design facilitates easy assembly, and permits us to swap out different fiber mirrors and insert devices (e.g., a diamond slab [24] or mechanical resonator) after aligning and characterizing the empty cavity. The assembled device has dimensions of 28 mm in all directions. This aspect ratio was chosen heuristically to maximize the frequencies of the structure's normal modes, thereby minimizing the coupling between ambient (or driven) vibrations and the cavity length. The upright aluminum piece serves as a mount for the flat mirror, and (in this case) the mirror is glued in place using Stycast 2850.

On the second aluminum piece, a shear piezoelectric actuator (Noliac CSAP03) supports the fiber mirror and controls the length of the cavity. This piezo was chosen for

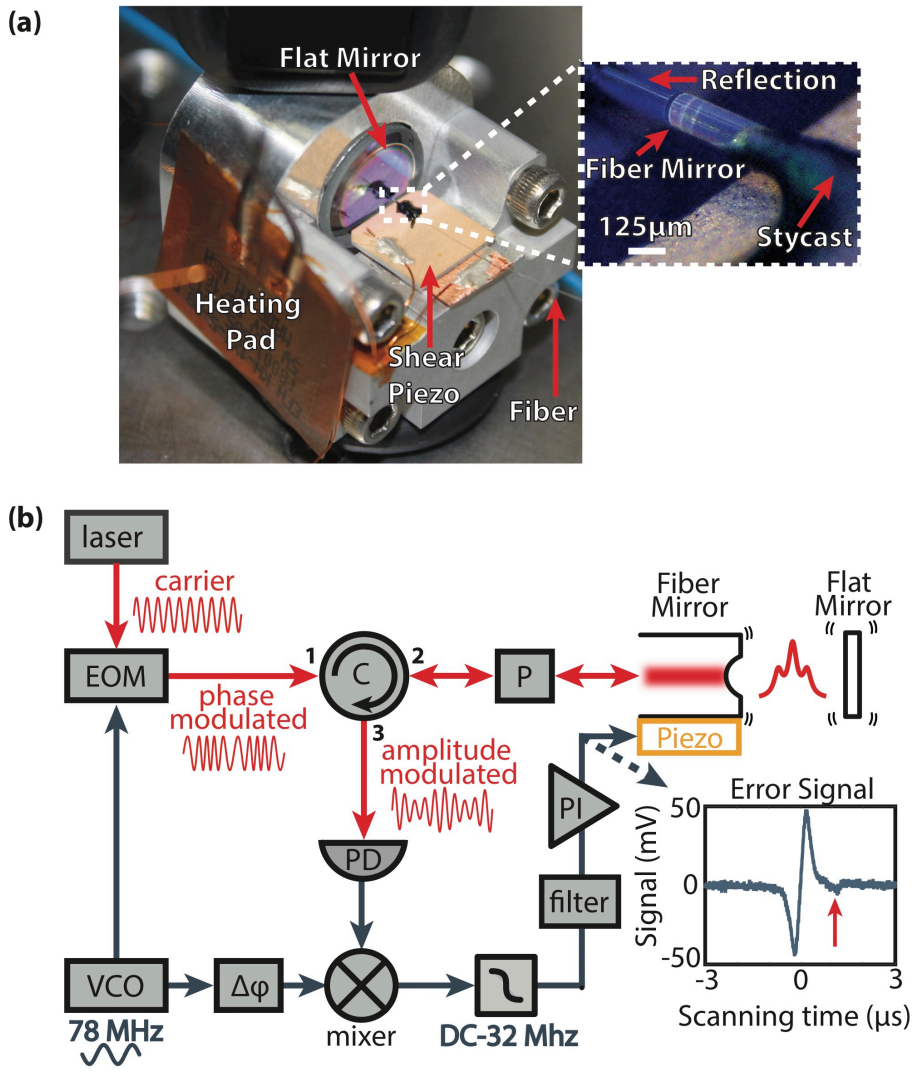

Figure 23: a) An image of the assembled fiber-coupled Fabry-Perot cavity device (inset: a microscope camera image showing the fiber mirror glued to the shear piezo, where the reflection can be seen in the flat mirror). b) A schematic showing the Pound-Drever-Hall locking circuit and a sample error signal measured for our cavity. The low amplitude nonideality visible to the right of the error signal (indicated with a red arrow) corresponds to the incompletely suppressed orthogonal linear polarization mode. EOM: electro-optic modulator; VCO: voltage controlled oscillator; PD: photodiode; C: circulator; filter: interchangeable analog filter circuit; P: polarization control; PI: proportional-integral amplifier.

its high unloaded resonance frequency of 1.75 MHz, which ultimately limits the theoretically achievable locking bandwidth. The bottom electrode is connected to a large DC voltage to coarsely tune the cavity length, while the top electrode is connected to a fast signal for feedback (maximum ± 10 V). The combined voltages we can achieve limit our travel range to $\approx$ 600 nm at room temperature, less than a free spectral range of our cavity ($\lambda/2 = 775$ nm). We therefore employ a heating pad and thermocouple to control the temperature of the aluminum, and tune a cavity resonance within range of the piezo. For the case of a cryogenic environment, piezo travel should decrease by a factor of ~ 5, requiring a combination of improved fabrication tolerances, higher drive voltages, and/or longer-travel piezo elements.

To mount the actuator, an alumina plate is first glued (Stycast 2850) to the second aluminum piece for electrical insulation. A piece of copper slightly longer than the piezo is then glued to the alumina, where the exposed copper is used for electrical contact to the bottom electrode. The piezo is attached to the copper sheet using silver epoxy (Epotek H20E), and kapton-coated copper wires are similarly glued to the copper sheet and top electrode. The two aluminum pieces are then screwed together.

Finally, the fiber mirror is pre-aligned above the actuator and glued in place with Stycast 2850 (the fiber is further aligned while submerged in the epoxy to maximize the contrast of the cavity reflection dip for a fundamental mode). The system is left to cure for 24 hours under ambient conditions, resulting in a geometric cavity length of approximately 15 μm (as determined by microscope image analysis).

The assembled device is then clamped to an optical table between two viton O-rings (visible above and below the device in Fig. 23(a)) to help isolate the system from high-frequency noise transmitted through the table.

4.2.2 *Pound-Drever-Hall Locking Circuit*

To lock the cavity length to our laser frequency, we employ active feedback via the Pound-Drever-Hall locking scheme [26, 27]. Briefly, the incident laser frequency is modulated and the reflected light is demodulated to produce an error signal that depends linearly on detuning from the cavity resonance. This signal is filtered, amplified, and fed back to the shear piezo under the fiber mirror.

The circuit used for generating an error signal is shown in Fig. 23(b), with optical (electrical) signal paths indicated in red (blue). The laser (Koheras Adjustik E15) is frequency modulated using an electro-optic phase modulator (EOM), driven with the output of a voltage controlled oscillator (VCO). The VCO is capable of generating output frequencies $f_m = 76 - 80$ MHz, which corresponds to the so-called "low-modulation regime" [27] for our cavity, which has a (full) linewidth of 189 ± 7 MHz. We find it is important to use only APC terminated fibers as well as isolators in our optical circuit to prevent back-reflections and standing waves that lead to residual amplitude modulation [28]. The modulated beam passes through a circulator (C) and couples to the cavity through the fiber mirror. The degeneracy of the two linear polarization states of the fundamental cavity mode is lifted by $\sim$ 100 MHz, likely due to a combination of fiber mirror ellipticity and birefringence [29]. The polarization is adjusted to select only one of these modes using a fiber polarizer (P), which we correct on an hourly basis as the strain in the fibers changes with lab temperature (typical temperature excursions $< 1\,^{\circ}$C). Note that using shorter fibers, thermally anchoring them, and stabilizing the temperature would significantly improve the polarization stability.

The reflected power is measured on a high bandwidth photodetector (bandwidth 150 MHz), and the output is demodulated by mixing with the VCO signal. The mixer output is sent through a 32 MHz low pass filter to remove the f_m and $2f_m$ oscillating terms, and the relative phase between the photodiode and mixing signal (ϕ) is adjusted by tuning the VCO frequency to obtain the desired error signal [27], similar to what is shown in the inset of Fig. 23(b). The residual signal from the incompletely suppressed orthogonal polarization mode is also visible to the right of the main features (indicated by the red arrow). This error signal is then sent through a combination of filters and a servo controller consisting of a "proportional-integral" (PI) amplifier (Newfocus LB1005) before finally being applied to the shear piezo. As discussed below, the filters and controller allow us to maximize the feedback gain at low frequencies for a given lock bandwidth.

4.3 Closed-Loop Measurements

4.3.1 *Measurement Block Diagram*

We can quickly gain insight into the limitations of this feedback system and the mechanical response of the mount by injecting a disturbance into the locked circuit and measuring its response, as described by Reinhardt *et al.* in [30]. As discussed below, this provides an estimate of the closed-loop transfer function.

A block diagram representing our feedback system is shown in Fig. 24(a), where all circuit element transfer functions and signals are complex functions of frequency. The error signal (a) is connected to the positive input of our servo controller, which also has an inverting input (b). The controller has an error monitor port that produces a voltage $e = T(a - b)$, where T is the associated transfer function. The controller itself has a PI transfer function P, such that its output voltage is $u = P(a - b)$. The output u then drives the system (G), which represents transduction between applied voltage and change in cavity length. Practically, this comprises a 200 Ω resistor in series with the piezo actuator supporting the fiber mirror. These two elements form a low-pass filter with a cut-off frequency $\approx$ 240 kHz. We found that it was not possible to lock the system without a resistor, as the low-pass filter behaviour is essential to suppress high-frequency perturbations. Consequently, the resistor is included in the system transfer function G for all closed-loop measurements. The piezo converts the output voltage into shear displacement (with a harmonic-oscillator-like transfer function), and all mechanical noise experienced by the cavity is modeled by the addition of a driving term d. The deviation of the length of the cavity from resonance (as determined by the laser frequency) is measured by the cavity mirrors, photodiode, and mixer circuit, which together have transfer function $-M$. M represents the cavity light's dynamical response to mechanical motion (essentially a low-pass filter with time constant equal to the cavity's ringdown time[30, 31]), along with the transfer functions of the fiber components, photodiode, cables, mixer, and 32 MHz low-pass filter, the last of which limits the bandwidth of M. The sign of M is determined by the phase of the local oscillator, and is negative in our case. As discussed below, we also have the freedom to introduce an ad-

ditional filter F prior to the PI controller, where the output is the error signal a that is fed back to the servo controller.

To probe the frequency response of different elements in the loop, we can apply a known perturbation b on the inverting input of the servo controller and observe the closed-loop response. Solving for the measurable quantity e in terms of the inputs b and d yields:

$$e = \frac{-T}{1 + PGMF} b - \frac{-TMF}{1 + PGMF} d. \tag{4.1}$$

All of the perturbations acting on the locking system are scaled by a term proportional to $1/(1 + PGMF)$. Thus, when the magnitude of $PGMF$ is large, the effect of these disturbances is minimized and the error signal tends to 0. Conversely, if $PGMF$ approaches the value -1 at some frequency, we enter a situation of positive feedback where the signal on the inputs is amplified [32]. Using a dual-phase lock-in amplifier (Zurich Instruments HF2LI) to supply the perturbation b and to measure e, the noise term d (which is uncorrelated with the lock-in's output b) can be eliminated, and it is straightforward to extract the circuit transfer function:

$$PGMF = -\frac{Tb}{e} - 1. \tag{4.2}$$

Here the only unknown is the error monitor port transfer function T, which can be measured independently (i.e. while unlocked). We hereafter refer to $PGMF$ as the transfer function of the circuit.

4.3.2 *Closed-loop Measurements*

The extracted circuit transfer functions can be seen in Fig. 24(b) for the "no filter" ($F = 1$) case, and for the case where F is an analog electronic filter (a lag compensator, schematic shown in Fig. 24(c)). The filter increases the noise suppression of the lock at low-frequencies by adding a second pole of roll-off to $PGMF$ from $\approx$ 300 Hz - 5 kHz, with the transfer function:

$$F = \frac{R_2(C_1 R_1 \omega - i)}{(C_1 + C_2)R_1 R_2 \omega - i(R_1 + R_2)} \tag{4.3}$$

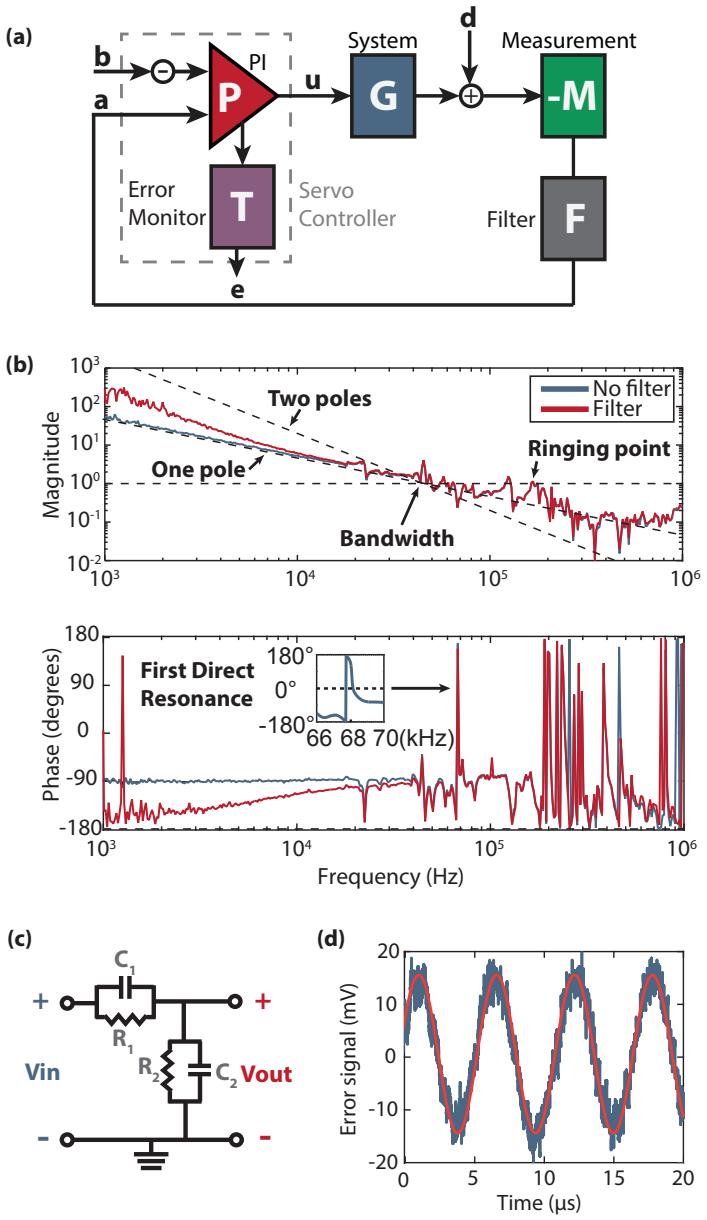

Figure 24: a) A block diagram illustrating the feedback loop. All circuit elements and signals are analyzed as a function of frequency. b) Circuit transfer functions ($PGMF$) extracted for the two different filter configurations (as described in the text). The circuit bandwidth, first ringing point, and first direct resonance are indicated with arrows (inset: high resolution plot of the measured phase response about the first direct resonance). The low frequency gains given one and two poles of roll-off from the bandwidth frequency are indicated with dashed lines. c) A circuit diagram for the electronic filter F. d) A time trace of the error signal where the gain has been increased to cause ringing at 179 kHz (fit overlaid in red).

where $C_1 = 330$ pF, $C_2 = 4.7$ nF, $R_1 = 100$ kΩ, and $R_2 = 1$ MΩ. The upper frequency bound in the filter is limited by needing to avoid a $-\pi$ phase excursion at the resonance near 20 kHz. In principle, the lower frequency bound could be further reduced to maintain two poles of roll-off over a larger frequency range. In practice, we are limited by the finite gain of our servo controller, and chose 300 Hz as a compromise that maximized gain near 1 kHz.

For the "no filter" case, $PGMF$ exhibits one pole of roll-off at low frequencies from the PI controller, which has transfer function $P = K(1 - i\frac{\omega_{PI}}{\omega})$, where K is the servo controller gain, and ω_{PI} is the "PI corner" frequency of $\omega_{PI}/2\pi$=100 kHz. The inclusion of the additional electronic filter allows us to attain a higher low frequency gain ($PGMF = 272 \pm 40$ at 1 kHz), but does not affect the transfer function considerably at higher frequencies.

Between $20 - 68$ kHz some small resonances appear that are mainly related to motion of the macroscopic mirror, deformation of the aluminum jig, and bending resonances of the fiber tip, as discussed in detail in Section 4.4. We refer to these as "indirect" resonances since they correspond to small phase excursions of $< \pi$, and could in principle be compensated for with electronics. Starting at 68 kHz, an increasingly dense set of resonances appears, stemming from the mechanical modes of the fiber mount and the clamped fiber. We refer to these resonances as "direct", since they behave similarly to a directly driven harmonic oscillator, exhibiting a phase decrease on the order of π when passing through resonance.

4.3.2.1 *Circuit Bandwidth*

We define the bandwidth of our circuit as the frequency range over which $|PGMF| > 1$ and $\arg(PGMF) > -\pi$; if the limiting conditions occur at the same frequency, it corresponds to the ringing condition of our system ($PGMF = -1$). Our definition of bandwidth (as opposed to a -3 dB point) is appropriate for a feedback circuit where the gain at low frequencies can be arbitrarily large if integrator components are used. This bandwidth corresponds to the maximum frequency at which noise can be suppressed; furthermore, it also places a ceiling on the gain at all lower frequencies (since $PGMF$ can increase at most as the inverse frequency squared). One can see that for both plots in Fig. 24(b), the first instance of $|PGMF| = 1$ occurs at 44 kHz, while $\arg(PGMF) > -\pi$

for frequencies up to 68 kHz (the first direct resonance). Note that the apparent $-\pi$ phase crossing point at 1.5 kHz in the "filter" plot is a result of measurement noise. Essentially, the feedback at low frequencies is so efficient that the suppressed signal is small compared to the noise in our lock-in amplifier, leading to increased noise in our estimate of circuit gain. We therefore conservatively define the bandwidth of our system as 44 kHz for both measurements.

4.3.2.2 *Ringing frequency*

For many systems, one would expect the amplitude and phase response to decrease monotonically with frequency after the first direct resonance (as, for example, in the case of a simple harmonic oscillator). In this case, the gain provided by the PI controller could be increased until $|PGMF| = 1$ at the lowest frequency where $\arg(PGMF) = -\pi$, and the system would ring at this frequency. The electro-mechanical modes of our system are not so simply modeled, and result in many high frequency resonances that exhibit an increase in magnitude and phase. Consequently, the bandwidth, first $-\pi$-phase crossing frequency, and first ringing frequency are all different. Figure 24(d) shows a time trace of the the locked error signal where the gain has been increased to hit the first ringing point at 179 kHz.

4.4 System Transfer Functions

As discussed in the previous section, the mechanical response of our cavity has a complicated structure. Because our other circuit components operate over a broad frequency range (MHz or more), our circuit bandwidth is set primarily by these mechanical resonances. It is therefore of interest to isolate the system transfer function G to determine limiting factors in the design with regard to the locking bandwidth.

We measure the axial response of the cavity mount (G) by coupling a 1310 nm laser through the fiber mirror where the dielectric mirror coatings are low finesse (with power reflection coefficient R$\approx$ 45%). A high voltage DC signal is first applied to the bottom electrode of the piezo to select a cavity length offset corresponding to high measurement sensitivity (approximately the point of highest slope on the reflection fringe). An AC drive voltage from a lock-in amplifier is then applied to the top electrode while recording

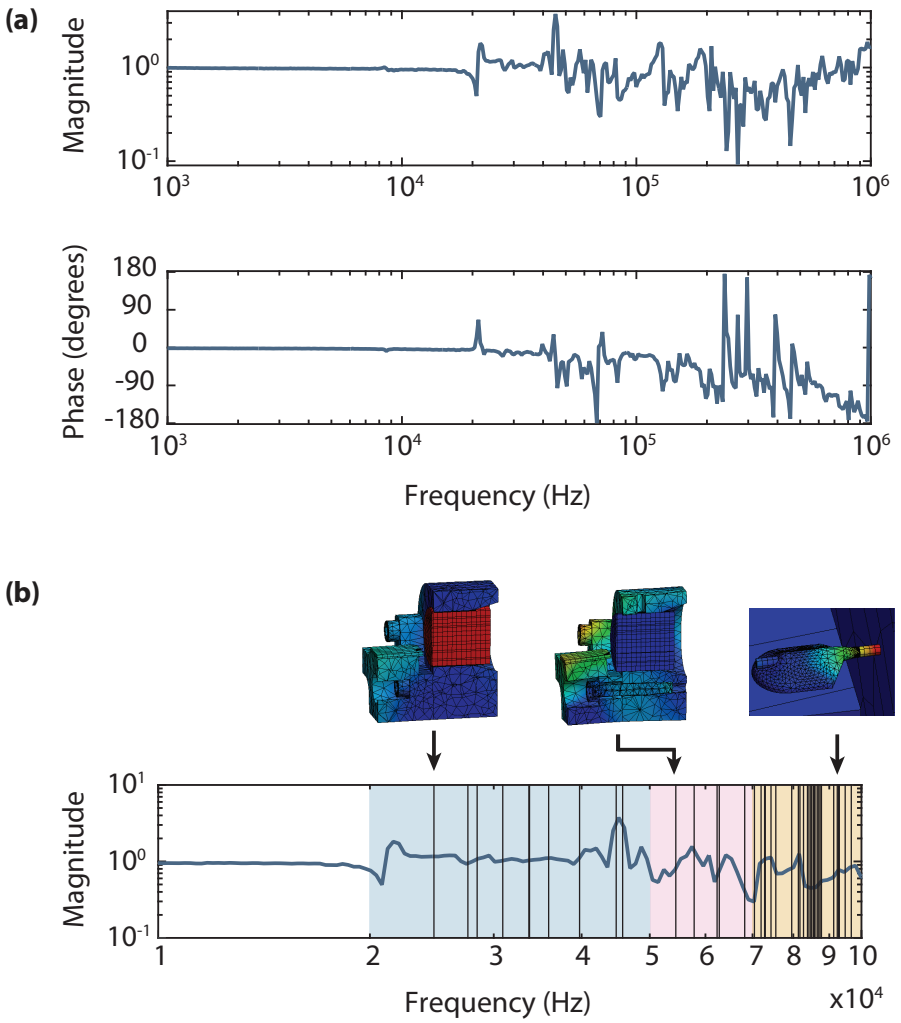

Figure 25: a) The system transfer function normalized to the low frequency magnitude. b) The amplitude of the measured system transfer function overlaid with a range of simulated mechanical resonant frequencies (black vertical lines). The low, medium, and high frequency regions as discussed in Section 4.4 are indicated by the blue, red, and orange shaded regions respectively. The simulated mechanical displacement for three typical resonances from the different regions are shown above (images used courtesy of ANSYS, Inc.), where the first mode corresponds to slipping motion of the flat mirror, the second mode corresponds to flexing of the jig under the piezo, and the third mode corresponds to motion of the fiber along the optical axis. These representations are exaggerated with respect to real displacement for clarity, with elements in red (blue) being subjected to larger (smaller) displacement for a given mode.

the modulation in reflected light, thereby probing the mechanical response of the system at different frequencies. The resulting system transfer function is shown in Fig. 25(a) (normalized to the low frequency amplitude).

We simulated the mechanical modes of the assembled cavity device using the ANSYS [33] finite element analysis program to understand the origin of different resonances. The results are overlaid with the measured amplitude response between $10 - 100$ kHz in Fig. 25(b), which yield a decent correspondence given the difficulties in modeling the exact system. Interestingly, the simulation suggests that the mechanical resonances can be divided into three distinct frequency ranges:

- The low frequency region ($20 - 50$ kHz) contains only a few modes and is mainly characterized by the deformation of the jig and the slip/rotation of the macroscopic flat mirror. We attribute the measured resonance near 20 kHz to the movement of the flat mirror in its housing (this mode is calculated to occur at 24.7 kHz in our simulations). These resonant frequencies could be improved (increased) by optimizing the geometry of the mount, reducing the mass of the macroscopic mirror, and changing how the mirror is fixed to the mount (for example, using a flexural clamp similar to a shaft collar).

- The mid-frequency region ($50 - 70$ kHz) is characterized by the low frequency bending resonances of the overhanging fiber tip, as well as the bending/folding of the jig under the piezo. Our simulations suggest that further reducing the length of overhanging fiber (from $L \approx 500$ μm) would increase the frequencies of the clamped fiber modes, where the resonant frequencies scale approximately with $1/L^2$ (up to frequencies where the mechanical modes of the glue structure are excited).

- The high-frequency region (> 70 kHz) is the most interesting with regard to fiber mounting considerations. In this frequency range, the fiber no longer acts as a simple clamped beam and the mechanical modes begin to incorporate motion of both the fiber and the glue bonding it to the piezo. The glue will deform along the fiber axis when driven with shear motion, impacting the cavity length directly. This could be improved by ensuring the fiber is in contact with the piezo while the epoxy cures, and by using less epoxy.

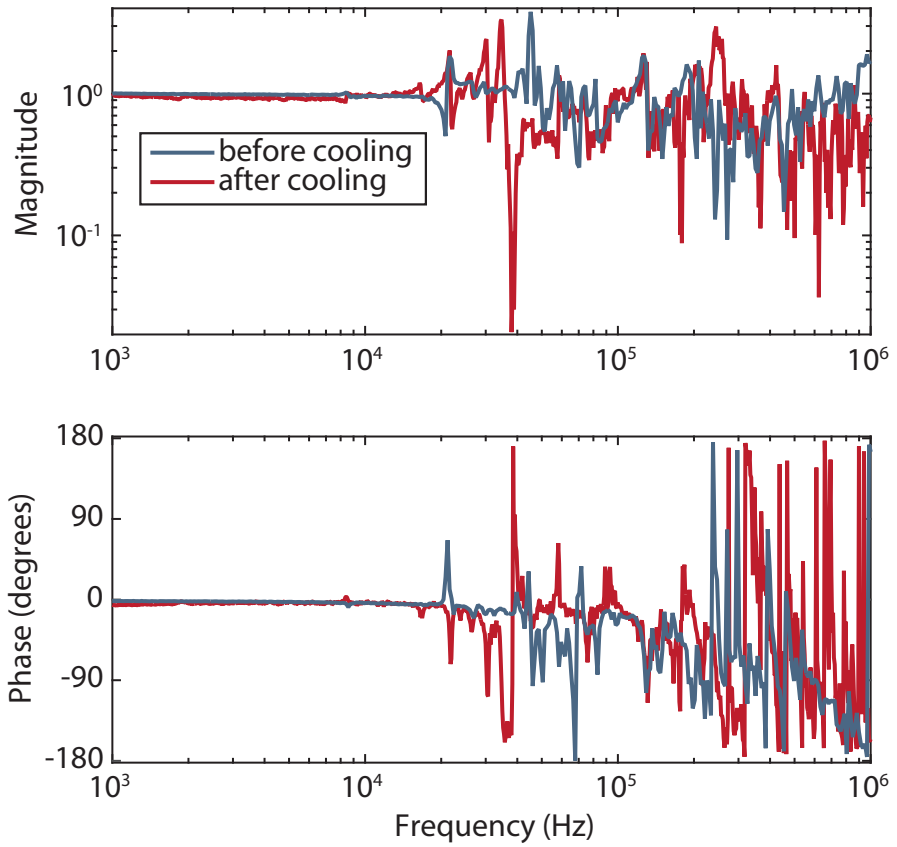

Figure 26: The system transfer function (G) before and after thermal cycling. The fiber mirror used before thermal cycling was replaced to facilitate a longer cavity length (shorter fiber overhang), and the piezo stack is unchanged.

At these high frequencies it is also necessary to consider vibration of the clamping screws, and "flapping" at unbonded corners for the different layers in the piezo stack.

4.4.1 *Thermal Cycling*

Many experiments in quantum optics require moving to cryogenic temperatures where mechanisms for thermal decoherence are suppressed. Although our device has not been expressly designed for cryogenic operation, its materials are in principle cryogenically

compatible, and thus we explore the impact of thermal cycling on the system. We clamp our device using a stainless steel strap to the base plate of a Montana Instruments Nanoscale Workstation cryostat. The fiber mirror used for the previous measurements was replaced to facilitate a longer cavity length of $\approx$ 60 μm that would prevent the fiber from crashing into the flat mirror due to thermal contraction of the mount. We estimate that this increase in cavity length corresponds to reducing the overhanging fiber length by $\sim$ 10%. The piezo stack is unchanged to allow for comparison with previous measurements.

The device survived two thermal cycles from room temperature to 6K. Due to the limited range of our piezo and voltage supplies, we were not able to make measurements at the base temperature. Nevertheless, after thermal cycling, we were able to maintain a cavity lock at 270K with the cryo-cooler running, but the system transfer function G changed considerably (see Fig. 26), likely due to a loosening of the aluminum screws holding the device together or delamination of the piezo stack. The new strong resonance at 37 kHz set a new ringing point for the locking circuit, and limited the achievable lock bandwidth to 3 kHz. We note this is not necessarily predictive of performance at base temperature, since the mechanical response of the structure's materials can change with temperature. The device broke at the epoxy connection between the alumina plate and aluminum mount as we tried to add Belleville washers to the screws, indicating that mount materials with a closer thermal expansion match to alumina (stainless steel, titanium) may prove advantageous for long-term cryogenic operation.

4.5 Conclusion

Fiber-based micro-mirrors offer a new platform for applications of high finesse Fabry-Perot cavities. We showed that a simple electronic feedback circuit can take advantage of the intrinsic high mechanical resonance frequency of a fiber mirror, achieving a lock bandwidth of 44 kHz. We also modeled the system, and our results suggest that the lock bandwidth may be further improved by minimizing the length of overhanging fiber from the piezo, and reducing the thickness of the epoxy holding the fiber. The resonance frequencies of the mount can be further increased by optimizing the geometry of the mount and, in particular, reducing the size (mass) of the flat mirror. Since our lock-

ing approach does not require strong intra-cavity laser power or specialized material damping properties, it should be extendable to cryogenic applications, or to systems requiring minimal perturbations to the cavity's light field and/or weak probe beams. Notably, even though our device is not expressly designed for cryogenic operation, we were still able to lock the cavity, clamped to the cold plate, with our closed-cycle cryostat running. This illustrates the potential for fiber-coupled optical cavity systems to operate in noisy environments, extending the range of applications for high finesse cavity measurements.

Funding

NSERC Discovery (435554 — 2013 and 418459 — 12); CRC (950 — 229003 and 235060); CFI (229003, 228130 and 33488); FRQNT (NC-172619); Alfred P. Sloan Foundation (BR2013 — 088); Centre for the Physics of Materials at McGill; Institute Transciplinaire d'Information Quantique; Y.F. acknowledges support by a Swiss National Foundation Early Postdoc Mobility Fellowship.

Acknowledgments

We thank Christoph Reinhardt, Tina Muller, and Yoichi Miyahara for helpful discussions.

References

1. Berden, G., Peeters, R. & Meijer, G. Cavity ring-down spectroscopy: Experimental schemes and applications. *International Reviews in Physical Chemistry* **19,** 565 (2000).
2. Srinivasan, K. & Painter, O. Linear and nonlinear optical spectroscopy of a strongly coupled microdisk–quantum dot system. *Nature* **450,** 862 (2007).
3. Udem, T., Holzwarth, R. & Hänsch, T. W. Optical frequency metrology. *Nature* **416,** 233 (2002).
4. Hinkley, N., Sherman, J., Phillips, N., Schioppo, M., Lemke, N., Beloy, K., Pizzocaro, M., Oates, C. & Ludlow, A. An atomic clock with 10^{18} instability. *Science* **341,** 1215 (2013).
5. Leibfried, D., Blatt, R., Monroe, C. & Wineland, D. Quantum dynamics of single trapped ions. *Reviews of Modern Physics* **75,** 281 (2003).
6. Birnbaum, K. M., Boca, A., Miller, R., Boozer, A. D., Northup, T. E. & Kimble, H. J. Photon blockade in an optical cavity with one trapped atom. *Nature* **436,** 87 (2005).
7. Mabuchi, H. & Doherty, A. Cavity quantum electrodynamics: coherence in context. *Science* **298,** 1372 (2002).
8. Keller, M., Lange, B., Hayasaka, K., Lange, W. & Walther, H. Continuous generation of single photons with controlled waveform in an ion-trap cavity system. *Nature* **431,** 1075 (2004).
9. Steiner, M., Meyer, H. M., Deutsch, C., Reichel, J. & Köhl, M. Single ion coupled to an optical fiber cavity. *Physical Review Letters* **110,** 043003 (2013).
10. Hunger, D., Steinmetz, T., Colombe, Y., Deutsch, C., Hänsch, T. W. & Reichel, J. A fiber Fabry-Perot cavity with high finesse. *New Journal of Physics* **12,** 065038 (2010).
11. Gehr, R., Volz, J., Dubois, G., Steinmetz, T., Colombe, Y., Lev, B. L., Long, R., Estève, J. & Reichel, J. Cavity-based single atom preparation and high-fidelity hyperfine state readout. *Physical Review Letters* **104,** 203602 (2010).

12. Haas, F., Volz, J., Gehr, R., Reichel, J. & Estève, J. Entangled states of more than 40 atoms in an optical fiber cavity. *Science* **344,** 180 (2014).

13. Colombe, Y., Steinmetz, T., Dubois, G., Linke, F., Hunger, D. & Reichel, J. Strong atom-field coupling for Bose-Einstein condensates in an optical cavity on a chip. *Nature* **450,** 272 (2007).

14. Ballance, T. G., Meyer, H. M., Kobel, P., Ott, K., Reichel, J. & Köhl, M. Cavity-induced backaction in Purcell-enhanced photon emission of a single ion in an ultraviolet fiber cavity. *Physical Review A* **95,** 033812 (3 2017).

15. Kashkanova, A., Shkarin, A., Brown, C., Flowers-Jacobs, N., Childress, L., Hoch, S., Hohmann, L., Ott, K., Reichel, J. & Harris, J. Superfluid Brillouin optomechanics. *Nature Physics* **13,** 74 (2017).

16. Flowers-Jacobs, N., Hoch, S., Sankey, J., Kashkanova, A., Jayich, A., Deutsch, C., Reichel, J. & Harris, J. Fiber-cavity-based optomechanical device. *Applied Physics Letters* **101,** 221109 (2012).

17. Toninelli, C., Delley, Y., Stöferle, T., Renn, A., Götzinger, S. & Sandoghdar, V. A scanning microcavity for in situ control of single-molecule emission. *Applied Physics Letters* **97,** 021107 (2010).

18. Albrecht, R., Bommer, A., Deutsch, C., Reichel, J. & Becher, C. Coupling of a single nitrogen-vacancy center in diamond to a fiber-based microcavity. *Physical Review Letters* **110,** 243602 (2013).

19. Benedikter, J., Kaupp, H., Hümmer, T., Liang, Y., Bommer, A., Becher, C., Krueger, A., Smith, J. M., Hänsch, T. W. & Hunger, D. Cavity-enhanced single-photon source based on the silicon-vacancy center in diamond. *Physical Review Applied* **7,** 024031 (2017).

20. Riedel, D., Söllner, I., Shields, B. J., Starosielec, S., Appel, P., Neu, E., Maletinsky, P. & Warburton, R. J. Deterministic enhancement of coherent photon generation from a nitrogen-vacancy center in ultrapure diamond. *Physical Review X* **7,** 031040 (2017).

21. Gallego, J., Ghosh, S., Alavi, S. K., Alt, W., Martinez-Dorantes, M., Meschede, D. & Ratschbacher, L. High-finesse fiber Fabry–Perot cavities: stabilization and mode matching analysis. *Applied Physics B* **122,** 1 (2016).

22. Brachmann, J. F., Kaupp, H., Hänsch, T. W. & Hunger, D. Photothermal effects in ultra-precisely stabilized tunable microcavities. *Optics Express* **24,** 21205 (2016).

23. Briles, T. C., Yost, D. C., Cingöz, A., Ye, J. & Schibli, T. R. Simple piezoelectric-actuated mirror with 180 kHz servo bandwidth. *Optics Express* **18,** 9739 (2010).

24. Janitz, E., Ruf, M., Dimock, M., Bourassa, A., Sankey, J. & Childress, L. Fabry-Perot microcavity for diamond-based photonics. *Physical Review A* **92,** 043844 (2015).

25. Brandstätter, B. *et al.* Integrated fiber-mirror ion trap for strong ion-cavity coupling. *Review of Scientific Instruments* **84,** 123104 (2013).

26. Drever, R., Hall, J. L., Kowalski, F., Hough, J., Ford, G., Munley, A. & Ward, H. Laser phase and frequency stabilization using an optical resonator. *Applied Physics B* **31,** 97 (1983).

27. Black, E. D. An introduction to Pound–Drever–Hall laser frequency stabilization. *American Journal of Physics* **69,** 79 (2001).

28. Whittaker, E. A., Gehrtz, M. & Bjorklund, G. C. Residual amplitude modulation in laser electro-optic phase modulation. *Journal of the Optical Society of America B* **2,** 1320 (1985).

29. Uphoff, M., Brekenfeld, M., Rempe, G. & Ritter, S. Frequency splitting of polarization eigenmodes in microscopic Fabry–Perot cavities. *New Journal of Physics* **17,** 013053 (2015).

30. Reinhardt, C., Müller, T. & Sankey, J. C. Simple delay-limited sideband locking with heterodyne readout. *Optics Express* **25,** 1582 (2017).

31. Rakhmanov, M., Savage, R., Reitze, D. & Tanner, D. Dynamic resonance of light in Fabry–Perot cavities. *Physics Letters A* **305,** 239 (2002).

32. Bechhoefer, J. Feedback for physicists: A tutorial essay on control. *Reviews of Modern Physics* **77,** 783 (2005).

33. *ANSYS Workbench* 17.0 (SAS IP, 2015).

5

Conclusion

5.1 Summary and Discussion

In the introduction to this thesis, we motivated the use of a hybrid light-matter interface in quantum networks, wherein spatially separated quantum matter nodes are connected optically. Quantum defects in diamond are a particularly promising candidate platform, evidenced by a recent demonstration of optically-mediated entanglement between NV centers separated by over a kilometer [1]. However, entanglement rates in this system were limited by the rate of coherent photon emission, as well as the collection efficiency into a well-defined optical mode. In this thesis, we propose to improve this interaction rate by using a defect with superior optical properties, the germanium vacancy center, coupled to a fiber Fabry-Pérot microcavity. Such a cavity will enhance emission into its spectral and spatial mode, improving the rate of optically-mediated interactions by many orders of magnitude. The introduction concluded with a detailed theoretical discussion of the GeV center and microcavity, as well as a description of the device fabrication process.

The body of this thesis described three experimental milestones towards the realization of the aforementioned light-matter interface. The first manuscript (chapter 2) presented extensive characterization and modeling of a membrane-in-cavity device. We used the finesse (measured in length) as a figure of merit for the system, obtaining values of up to $37,000$ for a bare cavity, and $17,000$ for a membrane-in-cavity device. In addition, we measured broadband transmission, revealing periodic structure in the spectrum, which can be understood in terms of electric field localization in the diamond or air. We then derived an analytic expression for the resonance condition, and were subsequently able to infer geometric cavity parameters by fitting this expression to the measured spectrum. Furthermore, we developed a numeric cavity model using transfer matrices. This model included different types of loss, such as absorption in the mirrors and diamond, as well as scattering at the diamond interfaces. This allowed us to estimate

a Purcell enhancement of up to 20 for an ideal defect in the given system, with a projected enhancement of up to 200 given realistic improvements. Finally, we developed a nondegenerate perturbation theory to explain additional losses that originate from coupling to higher order modes.

This manuscript was the first to provide a detailed description of the mode structure of an open microcavity containing a thick (≈ 10 μm) membrane. The resulting model for the cavity electric field distribution has been used in interpreting subsequent experimental results, such as the Purcell enhancement of an NV center in a diamond membrane coupled to an open microcavity [2].

The second manuscript (chapter 3) described room temperature cavity-coupling of a single GeV center in a diamond membrane. Here, we used an experimental setup that permitted us to switch between the fiber mirror and an objective lens, allowing the membrane to be characterized in both confocal and cavity configurations. We first took confocal scans of the sample, revealing individually resolvable GeV centers. We then replaced the objective lens with the fiber mirror, and observed a spatial correlation between the known position of individual defects and high emission into the cavity mode. We studied a well-isolated defect, comparing emitter saturation measurements to demonstrate an increase in the spectral density of fluorescence caused by cavity funneling effects. We then estimated a Purcell enhancement of ≈ 10 for the studied emitter at cryogenic temperatures.

There have been several demonstrations of room-temperature cavity funneling using defects in nanodiamonds [3, 4], some of which have achieved much higher single photon flux than in our work [4]. Unfortunately, emitters in these systems are not suitable for optically-mediated entanglement schemes since defects in nanodiamonds exhibit large inhomogeneous broadening [5]. In contrast, our system utilizes defects in diamond membranes which can exhibit excellent optical properties at cryogenic temperature [6]. This platform therefore has the potential to be used for such interactions without any further improvement to the cavity geometry.

The final manuscript (chapter 4) provides a method for actively stabilizing the cavity resonance to the frequency of a fixed optical transition. We first outlined the construction of a rigid fiber cavity mount which allows the cavity length to be tuned by moving the fiber mirror with a shear piezoelectric actuator. We then provided details on our Pound-Drever-Hall locking circuit, which was used to convert the measured cavity re-

flection into an electronic feedback signal. We locked the cavity length to a laser (which could be further locked to an optical transition) and measured a closed-loop feedback bandwidth of 44 kHz. In addition, we measured the open-loop system transfer function and performed simulations to understand the origin of different mechanical resonances. Finally, we thermally cycled the device in a closed-cycle cryostat and were able to subsequently lock the cavity with the cryo-cooler running.

This experiment achieved the highest mechanical feedback bandwidth for a fiber cavity to date, which is critical for coupling to fixed-frequency systems (where laser feedback is not possible). The small mass of the fiber mirror allowed us to take advantage of the high mechanical resonance frequencies afforded by shear piezoelectric actuators, demonstrating another attractive feature of the microcavity geometry.

5.2 Future Directions

The next step toward creating an efficient light-matter interface is to cool a cavity device to liquid helium temperature, where single GeV centers can exhibit nearly lifetime-limited optical transitions [7]. In this regime, it should be possible to measure a strong Purcell enhancement for ZPL transitions that are resonantly coupled to a microcavity. For the device characterized in chapter 3, we predict a $\approx$ 7-fold increase in the spontaneous emission rate for the studied emitter. In addition to higher photon flux, the collection efficiency would be improved dramatically compared to free-space emission, with potential power couplings of over 90% between the cavity and fiber mode for the 45 μm radius of curvature mirror used.

Achieving this goal would require some further experimental characterization and modification of the room-temperature cavity device. First, resonant excitation should be performed on GeV centers in a micron-thick diamond membrane to confirm low homogeneous and inhomogeneous broadening, which is critical for optical entanglement schemes [8]. Furthermore, a cryogenic and vacuum compatible cavity mount must be used that is able to scan the membrane sample laterally, as well as the cavity length. Such a mount should also be mechanically rigid to mitigate motional coupling, as the cavity mode is sensitive to $\sim$ 10 pm motion along the fiber axis. To that end, we plan to employ a high-mechanical-resonance frequency positioner from Janssen Precision Engineering.

These cryogenic stages allow for precise control of the position of the flat mirror and sample relative to a fixed fiber mirror. In conjunction with a vibration isolation platform, a similar system has been shown to achieve sub-nanometer cavity length stability while mounted in a closed-cycle cryostat [9]. Active locking schemes such as the one described in chapter 4 could then be used to further reduce this instability to below a cavity linewidth. Once the cryogenic cavity is assembled, the simplest demonstration of Purcell enhancement would involve off-resonant excitation of an emitter through the flat mirror, and measurement of a reduced excited state lifetime in ZPL emission coupled to the fiber mode.

Further improvements to the Purcell enhancement could be achieved by refinement of the fiber mirror geometry. The single-photon Rabi frequency can be increased by reducing the mirror radius of curvature and cavity length; encouragingly, novel laser ablation protocols have recently achieved radii of curvature down to 5 μm [10] and ablation depths of ≈ 1 μm. However, the expected increase in interaction strength should be carefully weighed against the reduction in coupling efficiency between the cavity and fiber modes due to wavefront mismatch [11]. Meanwhile, it should be possible to drastically improve the GeV center spin coherence by reducing the sample temperature to ~ 100 mk through the use of a dilution refrigerator, where recent measurements with SiV centers achieved $T_2 = 13$ ms. Once the spin properties are confirmed, it should be possible to use the state-dependent transmission/reflection of such cavity systems to experimentally realize a quantum network using defects in diamond [12].

Beyond use in quantum networks, this cavity platform has the potential to probe more fundamental physics. These devices can be tuned through several cavity-coupling regimes, potentially achieving the "strong-coupling regime" wherein a single photon remains inside the cavity long enough to interact with the defect many times before escaping. This could facilitate studies of nonlinear optics at the single-photon level [13], or photon-mediated interactions between different defects in a single diamond membrane [14]. Moving forward, this flexible cavity platform could directly impact all applications requiring high photon collection efficiency and interaction strength, opening new avenues for exploring fundamental quantum optics with defect centers in diamond.

References

1. Hensen, B., Bernien, H., Dréau, A. E., Reiserer, A., Kalb, N., Blok, M. S., Ruitenberg, J., Vermeulen, R. F., Schouten, R. N., Abellán, C., *et al.* Loophole-free Bell inequality violation using electron spins separated by 1.3 kilometres. *Nature* **526,** 682 (2015).

2. Riedel, D., Söllner, I., Shields, B. J., Starosielec, S., Appel, P., Neu, E., Maletinsky, P. & Warburton, R. J. Deterministic enhancement of coherent photon generation from a nitrogen-vacancy center in ultrapure diamond. *Physical Review X* **7,** 031040 (2017).

3. Albrecht, R., Bommer, A., Deutsch, C., Reichel, J. & Becher, C. Coupling of a single nitrogen-vacancy center in diamond to a fiber-based microcavity. *Physical Review Letters* **110,** 243602 (2013).

4. Benedikter, J., Kaupp, H., Hümmer, T., Liang, Y., Bommer, A., Becher, C., Krueger, A., Smith, J. M., Hänsch, T. W. & Hunger, D. Cavity-enhanced single-photon source based on the silicon-vacancy center in diamond. *Physical Review Applied* **7,** 024031 (2017).

5. Jantzen, U., Kurz, A. B., Rudnicki, D. S., Schäfermeier, C., Jahnke, K. D., Andersen, U. L., Davydov, V. A., Agafonov, V. N., Kubanek, A., Rogers, L. J., *et al.* Nanodiamonds carrying silicon-vacancy quantum emitters with almost lifetime-limited linewidths. *New Journal of Physics* **18,** 073036 (2016).

6. Ruf, M., IJspeert, M., van Dam, S., de Jong, N., van den Berg, H., Evers, G. & Hanson, R. Optically coherent nitrogen-vacancy centers in μm-thin etched diamond membranes. *arXiv preprint arXiv:1904.00883* (2019).

7. Siyushev, P., Metsch, M. H., Ijaz, A., Binder, J. M., Bhaskar, M. K., Sukachev, D. D., Sipahigil, A., Evans, R. E., Nguyen, C. T., Lukin, M. D., *et al.* Optical and microwave control of germanium-vacancy center spins in diamond. *Physical Review B* **96,** 081201 (2017).

8. Bernien, H., Hensen, B., Pfaff, W., Koolstra, G., Blok, M., Robledo, L., Taminiau, T., Markham, M., Twitchen, D., Childress, L., *et al.* Heralded entanglement between solid-state qubits separated by three metres. *Nature* **497,** 86 (2013).

9. Bogdanović, S., van Dam, S. B., Bonato, C., Coenen, L. C., Zwerver, A.-M. J., Hensen, B., Liddy, M. S., Fink, T., Reiserer, A., Lončar, M., *et al.* Design and low-temperature characterization of a tunable microcavity for diamond-based quantum networks. *Applied Physics Letters* **110,** 171103 (2017).

10. Najer, D., Renggli, M., Riedel, D., Starosielec, S. & Warburton, R. J. Fabrication of mirror templates in silica with micron-sized radii of curvature. *Applied Physics Letters* **110,** 011101 (2017).

11. Hunger, D., Steinmetz, T., Colombe, Y., Deutsch, C., Hänsch, T. W. & Reichel, J. A fiber Fabry–Perot cavity with high finesse. *New Journal of Physics* **12,** 065038 (2010).

12. Nemoto, K., Trupke, M., Devitt, S. J., Stephens, A. M., Scharfenberger, B., Buczak, K., Nöbauer, T., Everitt, M. S., Schmiedmayer, J. & Munro, W. J. Photonic architecture for scalable quantum information processing in diamond. *Physical Review X* **4,** 031022 (2014).

13. Birnbaum, K. M., Boca, A., Miller, R., Boozer, A. D., Northup, T. E. & Kimble, H. J. Photon blockade in an optical cavity with one trapped atom. *Nature* **436,** 87 (2005).

14. Evans, R. E., Bhaskar, M. K., Sukachev, D. D., Nguyen, C. T., Sipahigil, A., Burek, M. J., Machielse, B., Zhang, G. H., Zibrov, A. S., Bielejec, E., *et al.* Photon-mediated interactions between quantum emitters in a diamond nanocavity. *Science* **362,** 662 (2018).